Development of an Integrated Microfluidic Platform for Oxygen Sensing and Delivery

by

Adam P. Vollmer

B.S. Mechanical Engineering
Stanford University, 2002

SUBMITTED TO THE DEPARTMENT OF MECHANICAL ENGINEERING IN PARTIAL FULFILLMENT OF THE REQUIREMENTS FOR THE DEGREE OF

MASTER OF SCIENCE IN MECHANICAL ENGINEERING
AT THE
MASSACHUSETTS INSTITUTE OF TECHNOLOGY

JUNE 2005

Signature of Author: _____
Department of Mechanical Engineering
May 6, 2005

Certified by: _____
Todd Thorsen
Assistant Professor of Mechanical Engineering
Thesis Supervisor

Certified by: _____
Richard Gilbert
Visiting Scientist, Department of Mechanical Engineering
Thesis Supervisor

Accepted by: _____
Lallit Anand
Graduate Officer, Department of Mechanical Engineering

BARKER

(This page intentionally left blank)

Development of an Integrated Microfluidic Platform for Oxygen Sensing and Delivery

by

Adam P. Vollmer

Submitted to the Department of Mechanical Engineering on May, 6, 2005 in Partial Fulfillment of the Requirements for the Degree of Master of Science in Mechanical Engineering

Abstract

Treatment for end stage lung disease has failed to benefit from advances in medical technology that have produced new treatments for cardiovascular disease, certain cancers, and other major illnesses in recent years. As a result, end stage lung disease remains a devastating condition with few therapeutic options. To address the need for improved methods of respiratory life support, a novel technology was developed capable of generating oxygen directly from water present in blood plasma. This technology is intended to provide a self-contained, mobile oxygen supply suitable for implantation or extracorporeal oxygenation in support of an acute or chronically disabled lung. The core technology couples an optoelectronic metal oxide film with a microfluidic capillary network to facilitate oxygen exchange with flowing blood and replicate pulmonary capillary respiration. This thesis focuses on the optimization of this microfluidic capillary network with respect to hemocompatibility, mass transfer, and dissolved oxygen detection.

Microfluidic capillary devices were fabricated from silicone rubber using multilayer soft lithography to create dense 2D networks of bifurcating channels. To quantify the effectiveness of mass transfer in various channel geometries under differing experimental conditions, a mathematical model of oxygen convection and diffusion was generated. A novel integrated optical oxygen sensor based on an oxygen-quenched luminescent dye was developed to detect oxygen concentrations within the microfluidic device. Mass transfer within the microfluidic oxygenator was characterized experimentally, employing the integrated optical sensor, and analytically, using the convective model. Excellent agreement was found between experimental and analytical results.

We conclude that the microfluidic platform achieves rapid and efficient diffusion of oxygen into a liquid medium, effectively mimicking the function of the pulmonary system. The combination of precise oxygen delivery and detection, integrated into a miniature device, is widely applicable both to the photolytic artificial lung and to a broader class of applications related to detection of chemical species in biological microdevices.

Thesis Supervisors: Todd Thorsen
Title: Assistant Professor of Mechanical Engineering

Richard Gilbert
Title: Visiting Scientist, Department of Mechanical Engineering

(This page intentionally left blank)

Acknowledgements

Scores of friends and colleagues have contributed to making my experience at MIT more (and less) productive, more enlightening, and more rewarding than would ever have been possible without their advice, encouragement, and good company.

I would like to thank Todd Thorsen and Richard Gilbert for sharing their wisdom and good humor as my thesis advisors. You challenged me to maximize my experience as a graduate student by exploring new scientific directions. A special thanks to Harry Lee for selflessly providing an unlimited supply of good advice and guidance in my research efforts, and to Prof. Ronald Probstein for enlightening me in the science of mass transfer.

A special thank you goes out to the other half of the Thorsen group, JP Urbanski, whose fine taste in quality music, deep love of coffee and muffins, and masterful skills with the one-liner made the lab a good place to be. Thanks for helping to pass countless hours in the HML – sharing a desk with anyone else will never compare.

Thank you to my collective roommates over the past two years, Israel, Kyle, Hunt, Mo, Jess, Pete, Kathie (almost) and others. Yes, there are a lot of you. At the times when it felt like I lived in the lab, thanks for reminding me of all the good things I had to look forward to at home. Israel, thank you especially for Science Explorers. I may have learned more while dodging out of lab to build bottle rockets and volcanoes than I learned in my research and coursework combined.

Brady, thanks for staying close even though you were very far away.

Finally, thank you to my family, Mom, Dad, Eric, and Joanie. You have inspired me to be here. Thank you for always being there to share my excitement.

(This page intentionally left blank)

Contents

List of Tables and Figures

(This page intentionally left blank)

Chapter 1

Introduction

Despite major improvements across the spectrum of health care in the past 20 years, there have been few major advances in the care of patients with end-stage lung disease. While the death rate for certain cancers and cardiovascular disease has been substantially reduced, the death rate due to chronic lung disease has actually increased by over 50%. The increase in the death rate from chronic lung disease is largely on account of a relative lack of emerging therapies and inadequate technology for providing intermediate and long-term respiratory support. An estimated 250,000 deaths per year are attributed to lung disease, 150,000 of those related to acute, potentially reversible respiratory failure, and 100,000 related to chronic, irreversible respiratory failure. The total economic burden for all lung disease is in the range of 72 billion dollars annually. A particularly traumatic statistic is the mortality rate from lung disease in infants; lung disease accounts for 48% of all deaths for patients under one year of age (data from the Center for Disease Control, Atlanta). In addition to mortality, COPD poses significant quality of life impairments for its patients, in terms of challenges to employment and high levels of stress, depression, and anxiety.[1, 2]

The pressing medical case for the development of improved technological and therapeutic options for treatment of chronic lung disease has generated considerable interest in the area in recent decades. Recent advances in lung therapy have included an improvement of techniques for performing lung transplantation.[3, 4] Limitations in the number and availability of suitable donor organs, however, have made lung transplantation an unattainable option for the majority of patients. Rationing of donor lungs is particularly strict due to the large discrepancy between the numbers of donors and patients, the low yield of available lungs, and the absence of organ preservation methods during the pre-transplantation.[5, 6]

1.1 Mechanical respiration for treatment of lung disease

Various techniques have emerged and evolved to serve as a mechanical bridge to actual organ transplantation. Positive-pressure mechanical ventilation, in its modern incarnation, is a technique that evolved from WWII military technology for the delivery of oxygen and gas to fighter pilots at high altitude.[7] 'Positive pressure' means that positive pressure is applied at the patient's airway through an endotracheal or tracheostomy tube. This gas pressure causes oxygen to flow into the lungs until the ventilator breath is terminated, upon which point the lung volume is purged by the elastic recoil of the expanded chest, accomplishing passive exhalation. The efficacy of mechanical ventilation is very reliant on the severity of the patient's underlying disease state. Limitations of mechanical oxygenation include its prolonged, intensive nature, and the high possibility of adverse effects including oxygen toxicity, barotrauma, altered metabolism, and malnutrition.[8] These effects may in turn result in further injury to the failing lungs, and add significantly to morbidity and mortality.

Extracorporeal membrane oxygenation (ECMO) refers to the technique of augmenting oxygenation in the bloodstream through an extracorporeal circuit whereby oxygen is supplied diffusively to the blood through a microporous membrane. ECMO has been sufficiently refined to be suitable for oxygenation during cardiac bypass surgery.[9, 10] Despite its indisputable utility, ECMO is plagued by a number of functional limitations, including: 1) the requirement for a large and complex blood pump and oxygenator system, 2) the necessity for surgical cannulation, 3) the need for systemic anticoagulation, 4) a high rate of complications, including bleeding and infection, 5) biofouling due to protein adsorption and platelet adhesion on the surface of membranes, and 6) the high cost of implementation associated with labor intensive technical support. These limitations have confined ECMO largely to applications with a high probability of acute reversibility of disease prognosis.[11]

Intravenous membrane oxygenation (IVOX) is an extension of the membrane diffusion technology upon which ECMO is based, in which a membrane-bound hollow fiber catheter is inserted to the patient intravenously to allow O_2 and CO_2 diffusion.

IVOX is limited by a number of the same shortcomings as ECMO. In addition to a relatively high number of adverse effects, IVOX suffers from inefficient gas exchange, supplying less than 50% of basal O_2 requirements.[9, 11] Realizing that a primary impediment to effective mass transfer is the slow rate of venous oxygen diffusion, modern IVOX devices have achieved greater mass transfer efficiencies by including fluidic mixing elements.[12] Such added complexities increase the overall mechanical bulk of the device.

1.2 Development and applications of a photolytic oxygenator

In light of the limitations of current mechanical therapies for COPD – namely, their reliance on external pumping and gas supply apparatus and membrane-based diffusion, we have proposed the development of a self contained, miniaturized platform for artificial respiration. Such a device would be capable not simply of *delivering* oxygen to a patient's blood stream, but of *generating* oxygen directly in the blood stream from constituents of the blood plasma, thereby eliminating the reliance on external apparatus and facilitating an ambulatory therapeutic alternative for the treatment of chronic and acute lung disease. We propose for oxygen to be produced directly from the dissociation of water molecules in the blood plasma, a reaction that would be induced by a photo-catalytic, or photolytic, element fabricated integrally into the device. Fluidic transport in the device would be accomplished by means of an optimally designed hemocompatible microfluidic capillary network. Microfluidics deals with the transport of fluids at extremely low Reynolds numbers, on length scales sufficiently small to begin to mimic biological processes. Accomplishing oxygen transport in a microfluidic network would have the direct effect of accomplishing efficient diffusive oxygenation across an extremely small length scale, eliminating the need for gas mixing or pumping. An integrated microfluidic photolytic oxygen generation module would be a scalable device that could be designed to incorporated a high packing density of microchannels, accommodating near-physiological fluid flow rates and achieving rapid oxygen saturation within a minimal dimension. The research that will be discussed in this thesis was

undertaken in pursuit of this objective, with a specific emphasis on the design of the microfluidic element for facilitating blood flow and effective oxygen transfer at the microfluidic scale. In light of the motivation to develop new mechanical alternatives for the treatment of lung disease, the following applications of the microfluidic photolytic oxygenation platform are proposed:

1.2.1 Organ Preservation

The donor supply of transplantable lungs could be increased by maintaining the viability of lungs harvested immediately postmortem. Ischemic shock to lung tissue reduces lung viability to less than 50% within 4 hours of circulatory arrest. It has been experimentally demonstrated that perfusion of an oxygenated blood supply after the donor's death can maintain organ viability at significantly higher levels compared to un-oxygenated organs.[13] With this in mind, we envision a short term objective for the photolytic module to be the development of a mobile oxygenation/perfusion device easily suitable for organ transport and storage over the course of 12-24 hrs. Increasing the supply of available organs by maintaining more organs at a viable level would be a significant step towards alleviating demand on transplantation wait-lists and improving the degree of healthcare for lung disease patients.

1.2.2 Implantable Artificial Lung

An extension of the organ preservation device would be a small, self contained, implantable device capable of supporting and/or supplanting an ailing lung in the oxygenation of the body's pulmonary circulation. As opposed to the envisioned organ preservation device, an implantable unit would require considerably higher standards for operational lifetime, robustness, biocompatibility, packaging size, and power/electrical/optical control. As the majority of these objectives are far beyond the scope of this research, the investigation into the details regarding the artificial lung was

contained to a conceptualization of the theoretical structure of an integrated microfluidic/photolytic/optical/electronic device.

1.2.3 Additional micro-biological applications

Thinking beyond the application to the treatment of chronic lung disease, it is conceivable that an integrated microdevice capable of generating a controlled quantity of oxygen might find many other applications in micro-electro-mechanical (MEMS) related systems. As this thesis evolved, an increasingly important part of the research was the design and fabrication of an integrated oxygen sensor to detect gas levels within the microfluidic device. The delivery of a controlled oxygen supply and the accurate sensing of dissolved oxygen levels within a miniaturized environment is a necessity, for instance, in biological assay, bio-reactor, and tissue engineering applications. In cellular assays and bio-reactors, rapid determination of cell viability is frequently accomplished by monitoring of cellular metabolic activity via oxygen sensing. [14, 15] A controllable source of oxygen is a key constraint on cellular growth and development in tissue engineering applications. Newly implanted cells will consume the available oxygen supply within several hours, while it takes several days for angiogenesis to begin the creation of blood vessels to provide growing tissue with oxygen and nutrients.[16] As integrated microfluidic devices for such biological assay, reactor, and tissue engineering applications become increasingly ubiquitous, there is a compelling need for the development of flexible, low-cost oxygen sensors that can be rapidly prototyped and fabricated. This provides a third, independent, yet compelling motivation for the research into the development of an integrated microfluidic oxygen exchanger.

(This page intentionally left blank)

Chapter 2

Fundamental Technologies

Two fundamental technologies underlie the development of an integrated micro-oxygenation module. The first is photolytic oxygen generation, the use of a thin-film fabricated transition metal structure to generate dissolved oxygen directly in the bloodstream. The second is multi-layer soft-lithography microfluidics. A microfluidic network was developed to bridge the gap between the macroscopic physiological flow rates of the body and the microscopic scales at which diffusive oxygen transfer occurs most efficiently. Details of these two technologies, as they pertain to this research, are described in the following two sections. Before beginning this section, it is necessary to emphasize that this research, and this thesis, deal almost exclusively with the microfluidic portion of the device design. A photolytic film, developed by a corporate partner, was not made available for research purposes. Therefore, this work focuses purely on the microfluidic device design as it relates to hemocompatibility, mass transfer, and oxygen sensing. It is necessary, however, to explain the fundamentals of photolytic oxygen generation to motivate the development of the microfluidic component, as the artificial respiration device may be understood best as a whole.

2.1 Photolytic Oxygen Generation: Concept

As previously described, an inherent limitation of ECMO, IVOX, or other blood-oxygenation strategies is their reliance on membrane-based diffusion to supply a quantity of oxygen to the bloodstream. Such a technology requires a refillable tank and pump, rending it essentially non-mobile. A key motivating factor for this research has been the development of a portable artificial oxygenation technology that can produce oxygen

without the reliance on external apparatus or oxygen supplies. The use of a photo-catalyic, or photolytic, film obviates the need for an external oxygen supply and pump. Photolytic oxygenation refers to the generation of dissolved oxygen directly in the bloodstream, produced by the photo-catalyzed disassociation of water molecules in the plasma. The basis for photolytic reactions, broadly defined as those chemical reactions using energy derived from light, are ubiquitous mechanisms in nature for driving metabolism. One of the best-known photolytic reactions is photosynthesis, in which green plants and certain bacteria utilize sunlight to drive the production of dissolved oxygen (DO) from water and the exchange of oxygen for carbon dioxide, while simultaneously generating ATP. This research seeks to employ a novel family of photoactive materials which simulate the function of such naturally occurring photolytic reactions. This technology would address the challenge of artificial respiration not by delivering oxygen to the blood, but by converting the water already present in the blood into dissolved oxygen. The chemical details of the photolytic technology are described below.

The envisioned structure of the photolytic oxygenator resembles a sandwich of elements, including a robust semi-conducting transition metal oxide TiO_2 layer, Mn electrode films, fluidic channel, and some sort of UV light supply.

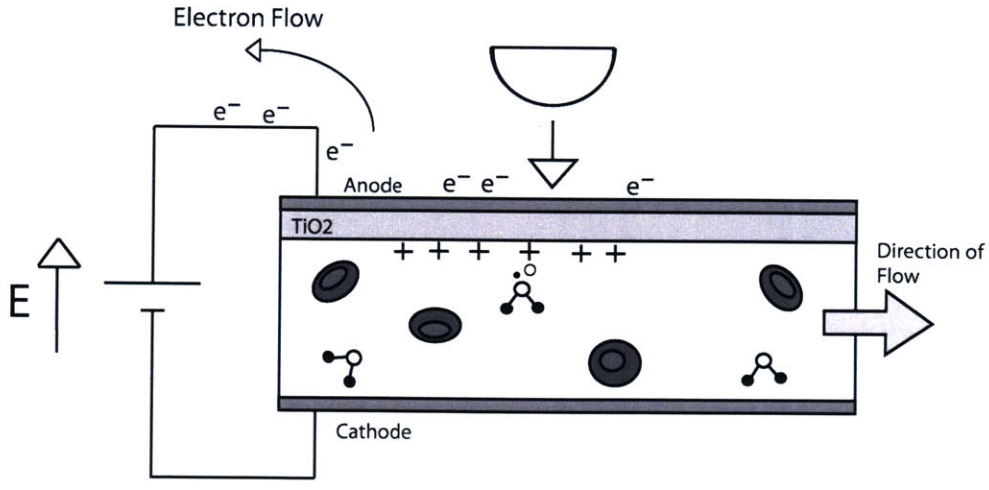

Figure 2.1: "Sandwich" structure of elements in photolytic oxygenator design.

The TiO_2 layer would be deposited upon a substrate of Mn with a chemical vapor deposition (CVD) process. The schematic of this structure is shown in fig. 2.1.

The photolytic structure operates by absorbing UV light, which promotes charge separation in the nano-crystals of the TiO_2 film, analogous to the generation of electron-hole pairs in electrical semiconductor materials. Free, electrons liberated into the conducting band, are pulled from the TiO_2 surface by application of an electrical potential, E. The potential E prevents "back reaction", the recombination of freed electrons with ionized elements in the TiO_2 film. The resulting ionized surface of the metal oxide layer is positively charged. This surface, which is in direct contact with the bloodstream, interacts with water molecules in the blood plasma and stimulates the dissociation of H_2O in a cascade of reactions, resulting in the production of, among other intermediary chemical species, dissolved oxygen (DO). This cascade of reactions occurs in four steps, which are described in detail.

PHOTOLYSIS

$$2H_2O + h\nu \xrightarrow{TiO_2\,(anatase)} H_2O_2 \text{ (Active oxygen, AO)} + 2H^+ + 2e^- \qquad (2.1)$$

DISPROPORTIONATION

$$H_2O_2\,(AO) \xrightarrow{MnO_2} \text{Dissolved oxygen (DO)} + H_2O \qquad (2.2)$$

PROTONATION

$$H^+ + HCO_3^- \longrightarrow H_2CO_3 \text{ (carbonic acid)} \qquad (2.3)$$

DEHYDRATION

$$H_2CO_3 \xrightarrow{Carbonic\,Anhydrase} H_2O + CO_2\uparrow \qquad (2.4)$$

In the photolysis reaction (2.1), water is dissociated by incident photonic energy to produce active oxygen (AO), H^+ ions, and free electrons. In the disproportionation reaction (2.2), AO spontaneously forms dissolved oxygen (DO), O_2. H^+ ions react with bicarbonate in the blood plasma to form carbonic acid (2.3), and carbonic acid is converted through dehydration (2.4) into water and CO_2. The principle products of the photolytic reaction, therefore, are DO and CO_2. DO diffuses from the TiO_2 surface into the bloodstream, where it is bound to hemoglobin in red blood cells (RBC's). An important challenge to the successful operation of the photolytic module is the chemical fixation or removal of CO_2, as CO_2 binds competitively to hemoglobin and will impede the oxygenation of RBC's. This will be discussed further in the considerations regarding the design of the microfluidic unit.

2.2 Photolytic Oxygen Generation: Validation

A photolytic film fabricated at Battelle Memorial Institute was tested in a preliminary proof-of-concept experiment by collaborators Bruce Monzyk (Battelle) and coworkers. UV light filtered to a wavelength of 365nm with an intensity of 88.1mW/cm^2 was delivered to a photolytic surface submerged in buffered water. To test the efficacy of oxygen generation, the electrical bias potential E = +1V, as well as the UV light, was cycled on and off, while the water's gas concentration was monitored in real-time by an electrode gas sensor. The results are shown in fig. 2.2.

Production of dissolved oxygen was evaluated in whole blood by perfusing a photolytic test cell with whole blood at a flow rate of 80 cc/min for 250 min. Samples from the collection reservoir downstream of the photolytic test cell were intermittently measured by blood gas analysis to determine O_2 concentration. Figure 2.3 shows this result, revealing that photolytic oxygenation effectively delivered a flux of DO to whole blood which approached saturation following a sufficient length of time.

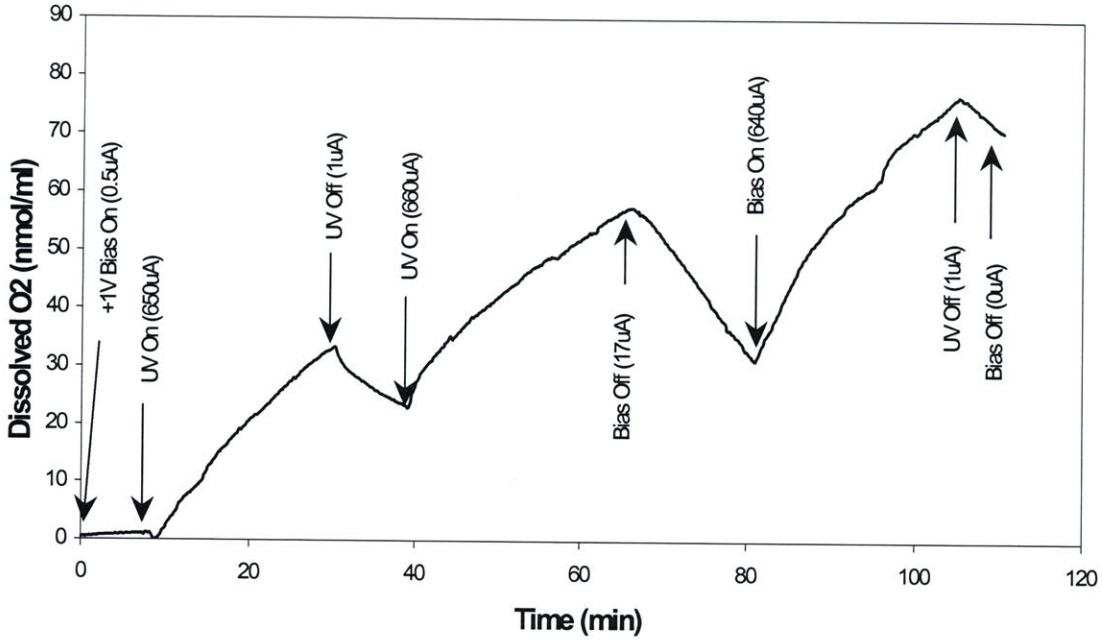

Figure 2.2: Dissolved O_2 concentration in aqueous photolytic test cell. Photolytic generation of DO occurs only when UV irradiation and bias potential E are applied simultaneously.

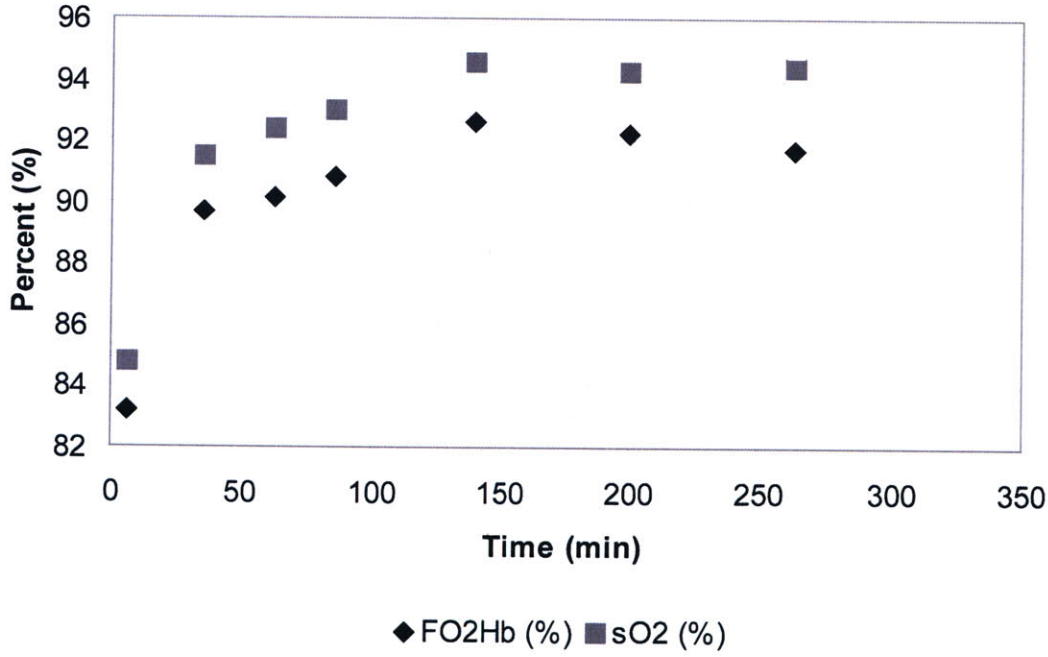

Figure 2.3: Percent oxygen concentration in whole blood versus time for photolytic test cell. FO2Hb represents the fraction of oxyhemoglobin, while sO2 represents the O_2 concentration relative to saturation in the blood plasma.

2.3 Multilayer soft lithography microfluidics

2.3.1 Microfluidics: Optimizing diffusion-limited mass transport

Blood flow is brought into contact with the TiO_2 photolytic film through a network of microfluidic channels. The use of microfluidics is intended to overcome inherently slow diffusion rates by accomplishing diffusive mass transfer on an extremely small length scale. Figure 2.3 reveals a significant limitation of the photolytic module as it has been previously implemented. The time constant to achieve nearly saturated blood-gas concentrations is approximately 150 min, a prohibitively long time for a device that is intended to be a fast and mobile oxygenator for emergency applications. The limiting factor in the speed of fluid oxygenation is not the magnitude of oxygen generation at the metal oxide surface, but rather the speed of diffusion of oxygen molecules through the bulk fluid. Whole blood is approximately 50% plasma by volume, the remaining volume being made up of RBC's, white blood cells, platelets, and other solid volumes. Plasma is 95% water by volume, which means that the diffusivity of O_2 in blood is approximately equal to the diffusivity of O_2 in water.

$$D_{O_2}(blood) \approx D_{O_2}(H_2O) = 2.4E-9 \quad \text{(m^2/s)}$$

The diffusion time for a molecule of oxygen to travel a particular distance L scales as follows:

$$t \sim \frac{L^2}{2D_{O_2}} \tag{2.5}$$

The approximate diffusion times for various length scales are shown in table 2.1. Diffusion becomes exponentially slower at large length scales, making it an extremely inefficient mechanism at macroscopic dimensions, such as those used in the photolytic flow cell experiment shown in fig. 2.3.

Length:	1 μm	10 μm	1 mm
Time	0.2 ms	0.02 s	200 s

Table 2.1: Approximate diffusion times for oxygen in water

To overcome the limitation of slow diffusive rates, efficient mass transfer may be accomplished either by actively mixing the fluid to increase the rate of O_2 uptake, or by reducing the length scale at which diffusion occurs. Mixing is undesirable, since it risks damaging RBC's in the blood and adds additionally complexity and apparatus to the oxygenator. Instead, the photolytic oxygenator is designed to operate in a microfluidic environment, intending to take advantage of the extremely small length scales possible in microscale flow and the corresponding rapid diffusion rates. This intuitively mimics the function of the lung, a biological oxygenation device. In the lung, the pulmonary arterial system transports RBC's in micron-sized capillaries into intimate contact with the alveoli, small air-filled sacks at the terminus of the lung's airways. Transport of O_2 and CO_2 in and out of the bloodstream, respectively, occurs rapidly across a thin membrane.

2.3.2 Multilayer soft lithography microfluidic fabrication

The particulars of the design and evolution of the microfluidic capillary network are discussed in detail in the following sections. Microfluidic devices are fabricated from polydimethylsiloxane (PDMS) using the technique of multi-layer soft lithography. Multi-layer soft lithography is a well documented technique for making rapidly prototyped devices suitable for biological and other applications.[17-19] In the simplest sense, soft lithography refers to the casting of polymeric stamps off of molds created using standard microfabrication techniques. A schematic of the soft lithography process is shown in fig. 2.4.

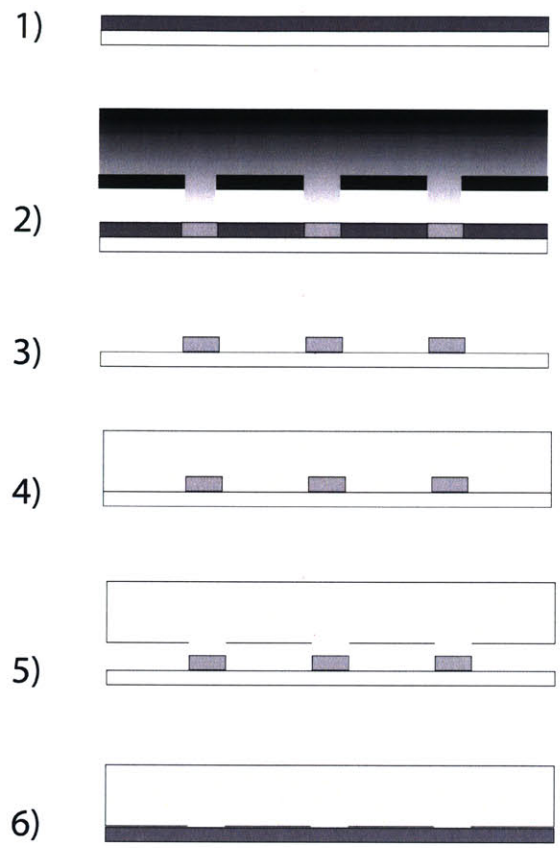

Figure 2.4: Polymeric stamping of a microfluidic device through soft lithography

Refering to fig. 2.4, steps 1-3 detail the photolithographic creation of a mold, while steps 4-6 detail the soft lithography casting of a PDMS device. In step 1), photoresist is spun coated on a silicon substrate to a desired thickness and baked, as appropriate for the particular photoresist. In step 2), the photoresist layer is illuminated with filtered UV light through a lithographic mask (chrome or transparency) to selectively cross-link the photoresist in the pattern of the mold. Simple transparency molds were used exclusively for this research, allowing feature resolution down to approximately 10-20 μm. Following UV exposure, the photoresist is post-baked then developed with an appropriate solvent, leaving a 2-D image of patterned channels on the surface of the Si wafer. Figure 2.5 shows a patterned photoresist mold on Si wafer.

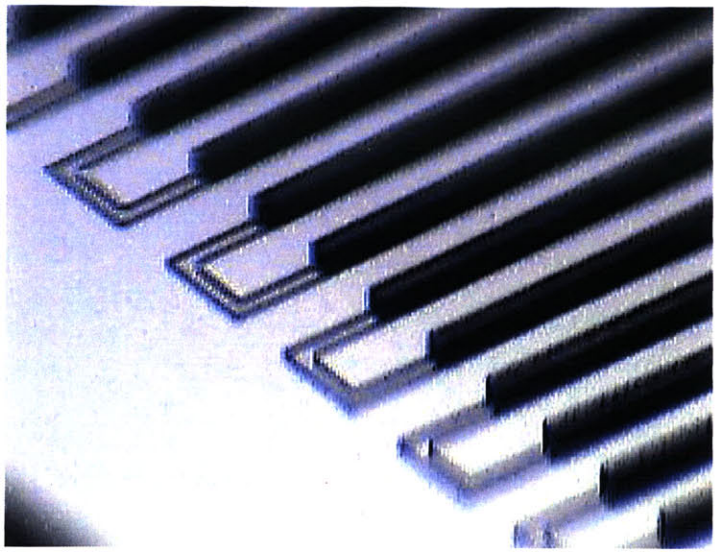

Figure 2.5: Photoresist mold, courtesy of JP Urbanski, Thorsen group, MIT

From fig. 2.4, step 4) illustrates the pouring of fluid (uncured) PDMS over the mold, which is then baked to crosslink the PDMS. Prior to pouring PDMS, the mold is treated with a silanization step to generate a Teflon-like layer of high molecular weight hydrophilic molecules over the mold surface. Silanization decreases adhesion of the PDMS to the photoresist mold and Si wafer, facilitating easier lift-off.[20] Solidified PDMS is peeled from the mold (step 5), then sealed to a substrate by plasma bonding (step 6).

Multi-layer soft lithography refers to the vertical stacking of multiple layers of fluid channels separated by thin layers of PDMS. Thin layers are created by spin-coating PDMS onto a wafer and baking, then pressing a thicker layer of PDMS on top of the thin coat. PDMS is a two-part polymer, consisting of a separate monomer and hardener which are custom mixed to the desired consistency before being baked and crosslinked into a flexible rubber. A typical monomer to hardener ratio, for a single-layer microfluidic device, is 10:1. For a multi-layer device, alternating PDMS layers are mixed at different monomer/hardener ratios. Typical ratios used in a two layer device are 20:1 and 5:1 for the lower and upper layers, respectively. The imbalance of hardener at the interface between the two layers facilitates crosslinking between layers during subsequent baking, forming a strong covalent bond. The two layers are adhered by baking, which

makes the thin layer sufficiently stiff to allow peel-off. A three layer device is illustrated in fig. 2.6.

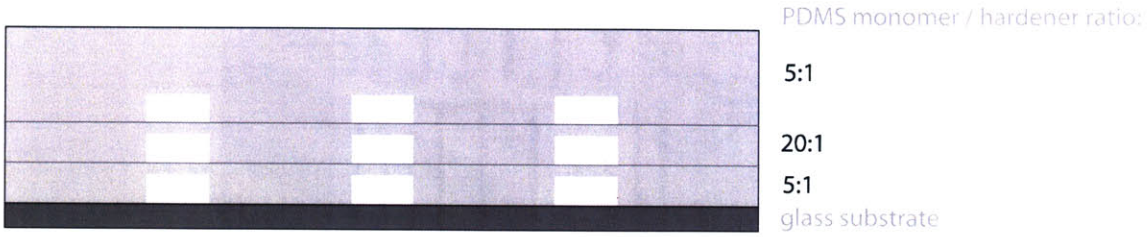

Figure 2.6: Multi-layer soft lithography

Multi-layer soft lithography permits extremely high packing density of fluidic channels, since individual PDMS layers may be on the order of 100 μm or less. A 1cm thick chip could conceivably contain 100 layers of fluid channels.

Chapter 3

Conceptualization of multi-layer microfluidic device

A large number of considerations underlie the design of the microfluidic network, making its structure an optimization problem. The following can be defined as primary objectives for the microfluidic network design:

3.1 Microfluidic device design: Primary objectives

1) Achieve hemocompatibility with blood flow
2) Translate between macroscopic and microfluidic flow regimes
3) Facilitate rapid, efficient oxygenation of blood

3.1.1 Hemocompatibility

Perfusion of blood through an artificial environment poses numerous challenges. The surface of PDMS is extremely hydrophobic, rendering it highly susceptible to protein adsorption, platelet aggregation, and thrombogenesis (clotting). Clotting can occlude a channel and cause pressure rises, device damage, and potentially result in downstream embolism if clots are freed from the PDMS walls and carried from the device into a patient's circulation. Thrombogenesis may result from interactions with proteins, such as fibrinogen, adsorbed to channel walls, or from adverse flow conditions such as recirculation and stagnation. In the case of stagnation or recirculation, the fluid velocity is sufficiently low that the blood thickens and clots are formed. Figure 3.1 demonstrates vorticity in the flow of a non-newtonian fluid in the entrance region of a sudden area

contraction.[21] Similar areas of vorticity in a shear-thinning non-newtonian fluid like blood are regions where clot formation might be expected.

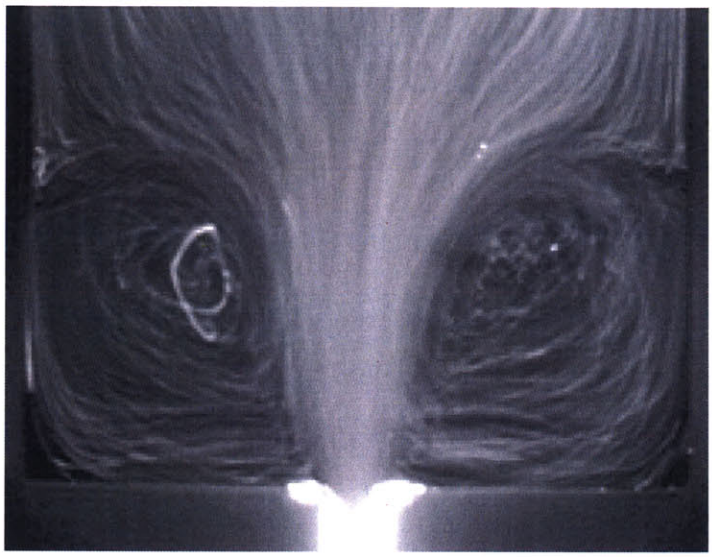

Figure 3.1: Vorticity observed in contraction flow of a non-newtonian viscoelastic fluid

Hemocompatibility refers additionally to the challenge of minimizing the shear stress in the fluidic network. Excessive shear stress can damage the RBC cellular membrane, hemolyzing the cell. The magnitude of shear stress arises from the magnitude of flow rate and channel cross sectional dimensions, as well as from the geometry of the fluid path.

3.1.2 Macrofluidic and microfluidic flow regimes

Typical microfluidic flow rates are on the order of nano-liters to micro-liters per minute, or in the very highest of flow rates, milli-liters per minute. In contrast, physiological flow rates are considerably more macroscopic; blood circulates through the body at an approximate flow rate of 5-10 L/min.[22] In order to achieve a near-physiological flow rate, a microfluidic device must straddle the limit between macro and microfluidics by incorporating an extremely high packing density of channels with an individual channel geometry capable of accommodating very high micro-flow rates. As previously

described, an upper limit on the flow rate of an individual channel is set by the RBC's susceptibility to hemolysis. There is, therefore, a tradeoff between hemocompatibility and desirable high flow rates.

3.1.3 Blood oxygenation

The microfluidic network must achieve rapid oxygen saturation in the bloodstream. As miniaturization of the overall oxygenation device is an objective, the microfluidic oxygenator should be designed so that it efficiently oxygenates the blood – that is to say, oxygenation should be accomplished in the shortest length possible. In addition to reducing the size of the device, a smaller device reduces the amount of fluidic resistance, decreasing the pressure needed to drive the blood through the microchannels, and thereby reducing the shear stress on blood cells.

The quantity of oxygen delivered to the bloodstream is a function of the fluid flow rate, the channel length, and height. Following sections will contain a detailed analysis of the optimization of the device's mass transfer characteristics.

3.2 Device construct and passive oxygenation

The 2-dimensional nature of soft lithography microfluidics lends itself well to the design of a stacked photolytic structure. Figure 3.2 demonstrates a visualization of the conceived structure for the integrated microfluidic/photolytic oxygenation module. PDMS fluidic elements are sandwiched between photolytic and accompanying electrical elements into a structure with a total height on the order of several millimeters. This structure could be stacked in repeating layers with integrated lightguides for UV illumination to achieve a very high density of fluidic channels in a compact module. In the device shown in fig. 3.2, the microfluidic element contains two parallel sets of channels, one for fluid flow (in contact with the photolytic surface), and one labeled for 'gas flow'.

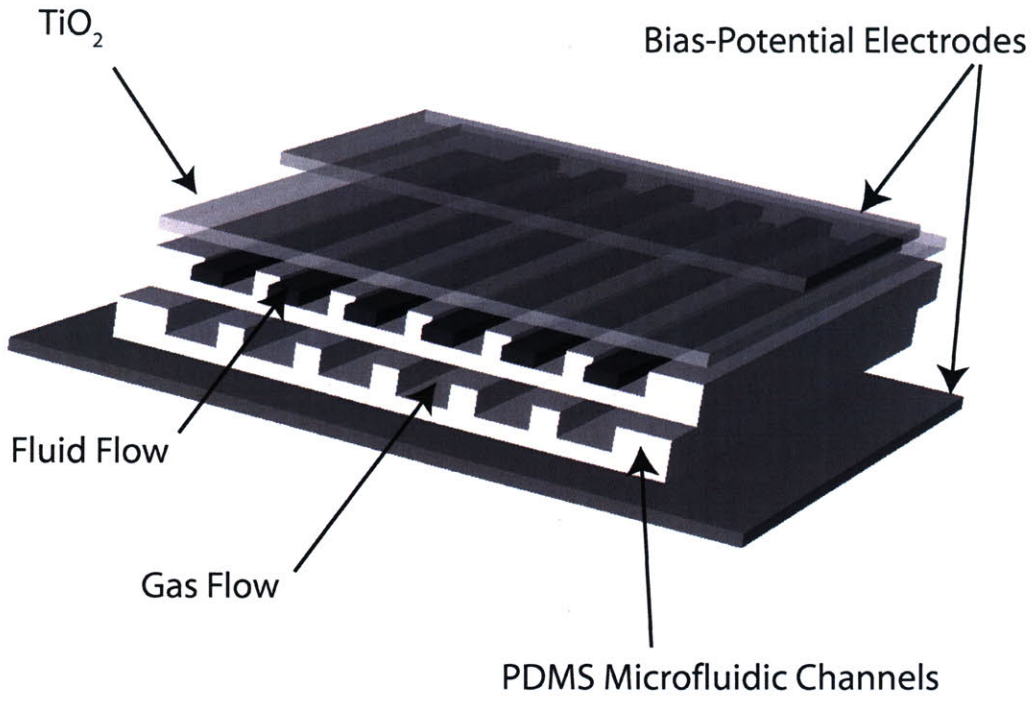

Figure 3.2: Conceived structure for integrated microfluidic photolytic oxygenation module. Multi-layer PDMS microfluidic channels are sandwiched between photolytic elements. The total thickness of the structure is on the order of several millimeters, meaning that multiple elements could be stacked back to back, achieving extremely high channel densities.

The gas flow channels shown in fig. 3.2 serve an important purpose in the design of the microfluidic module. First, they are intended to help purge CO_2 generated by the photolytic reaction from the bloodstream. In the normal function of the lungs, CO_2 is extracted from its binding to hemoglobin by the relatively low presence of CO_2 in the alveolar airways – the concentration gradient drives a flux out CO_2 out of the arteries, while an oppositely directed gradient drives diffusion of O_2 into the bloodstream. In a carbon dioxide-rich environment, CO_2 impedes the binding of O_2 to hemoglobin by directly binding to hemoglobin to form carbamates, and by forming bicarbonate that lowers the blood's pH and decreases hemoglobin's affinity for O_2.[23] In effect, the presence of large concentrations of CO_2 in the blood shifts the sigmoidal oxygen binding curve, shown in fig. 3.3, to the right. In addition to being produced as a byproduct of the photolytic reaction, CO_2 is present in blood entering the photolytic module, since this

blood is flowing from the venous return where it is transporting CO_2 from the tissue capillaries.

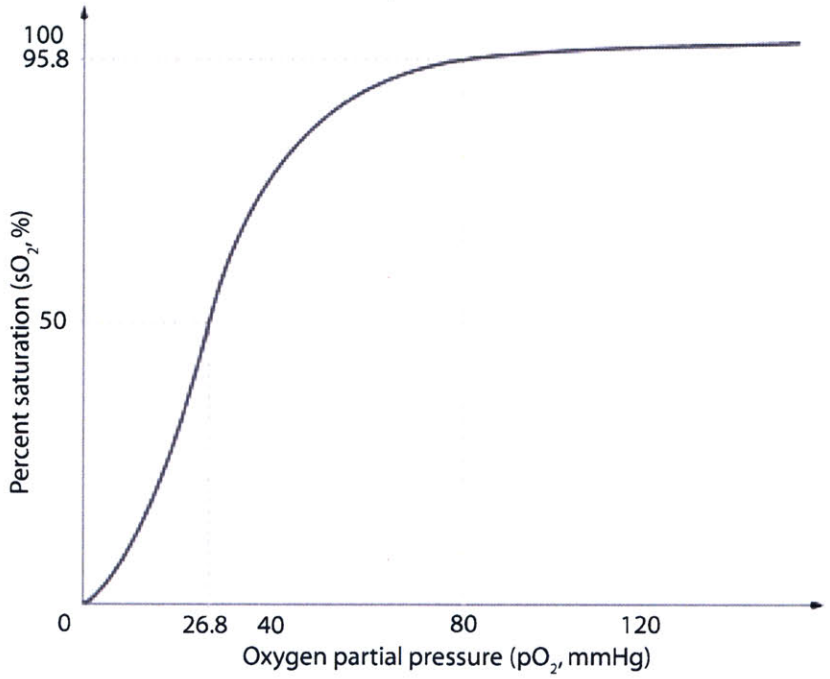

Figure 3.3: Sigmoidal oxygen affinity curve for blood

The gas flow channels in fig. 3.2 would serve the same purpose as the lung's alveoli, to promote O_2 binding by diffusively removing CO_2 generated by the photolyic reaction from the blood. One limitation on the strategy of removing excess CO_2 by diffusion through a membrane is the need to purge the gas channel lines to maintain a CO_2 gradient, potentially requiring an external pump. A primary intention of the photolytic module is to eliminate the reliance on external apparatus, meaning that CO_2 gas diffusion may not be an effective solution to the problem of removing CO_2 from the oxygenator.

Prior to serving as a solution for CO_2 removal, the gas channels fabricated in the multi-layer microfluidic structure serve a more important experimental purpose. Throughout the course of this research work, a functional photolytic metal oxide surface was not made available by research partners for testing or incorporation into an integrated oxygenation device. An original goal of this research was to replicate the experimental work on photolytic oxygenation shown in figs. 2.2 and 2.3 in a microfluidic environment.

The lack of a photolytic surface for testing purposes necessitated the development of other methods for the characterization and optimization of the mass-transfer properties in the microfluidic oxygenator. In order to simulate the behavior of an oxygen-generating photolytic surface, the microfluidic devices were fabricated as multiple layer devices with gas channels through which oxygen could be flowed. The high concentration of oxygen in the gas channels creates a large gradient across the thin PDMS membrane, driving diffusion of O_2 into the fluid channels. We refer to this technique as "passive oxygenation", as opposed to "active oxygenation" from a photolytic film. Passive oxygenation allowed testing of the mass transfer properties of the microfluidic network without the need for a TiO_2 surface. The ability to test the diffusion characteristics of the microfluidic device without the complexity of an oxide film, optical components (UV lamp and filters) and electrical components greatly simplified experimentation, while very accurately replicating the effect of an oxygen-generating surface. Figure 3.4 shows a microscope cross section of a device, illustrating the two vertically aligned channel layers separated by a thin (~20 μm) PDMS membrane. The lower set of channels, which would typically be sealed to the TiO_2 film, is bonded to a glass slide.

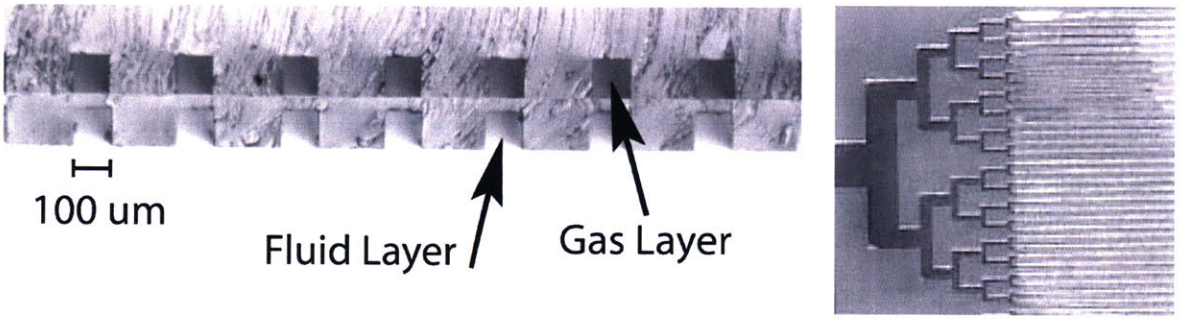

Figure 3.4: At left, cross section of fluid and gas channels in two-layer microfluidic device. Right, overhead view of capillary section and densely packed oxygenator channels.

Passive oxygenation proved to be an effective experimental technique, as the design of the capillary network geometry was entirely decoupled from the complexity of the photolytic element. The two-layer structure of a microfluidic chip for passive oxygenation is shown in fig. 3.5, with fluid dye illustrating the path of fluid flow (black arrowhead) and gas flow (white arrowhead).

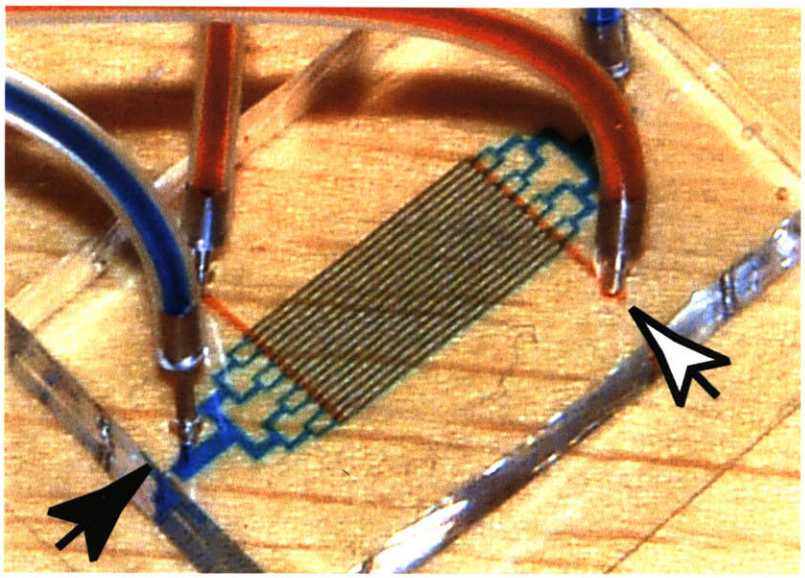

Figure 3.5: Two-layer microfluidic device for passive oxygenation with dyed fluid representing the path of the fluidic channels (black arrowhead) and gas channels (white arrowhead).

(This page intentionally left blank)

Chapter 4

Network Design: Evolutions

4.1 Scaling laws and capillary geometry

In an artificial microfluidic system, practical limitations related to the biocompatibility of blood flow in a synthetic environment limit the minimum length scale which may be used in designing microcapillaries. Blood flow in microchannels is limited predominantly by shear stress and intraluminal clotting. It was demonstrated experimentally by Brown et. al. that sustained shear stresses of 10-25 Pa result in "striking changes in morphology, biochemistry, and functional properties" of RBC's, while shear stresses from 150-450 Pa produce outright hemolysis (cell rupture).[24, 25] The diameter of a human red blood cell is approximately 7 μm, while the diameter of capillaries in the pulmonary arterial system is approximately 3 μm.[26] In a biological environment, the RBC deforms significantly into a plug shape to pass in single-file through narrow capillaries. The ability of RBC's to deform is aided by the endothelial lining and the natural compliance of the capillary wall. Experimental and analytical work on blood flow in glass microchannels suggests that, in an artificial environment, 100 μm is an approximate lower limit on the channel dimension to allow whole blood flow without considerable clotting and hemolysis (rupture) of RBC's.[27] It has been demonstrated that red blood cells can be flown through square PDMS channels with cross-sectional dimensions as small as 2x2 μm.[28] However, this experimental work was performed with solutions of RBC's only (no platelets or adhesion proteins, ie fibrinogen, etc.), at extremely low flow rates (~10-20 pL/min). We expect that the pressure drop associated with the passage of a near-physiological volume of blood at higher flow rates through such a small cross sectional area would generate unacceptably large levels of shear stress and cell hemolysis.

The choice of 100 μm for the minimum dimension of the blood microchannels sets the channel height of the microfluidic device, which is constant across the entire

device. The design challenge for the microfluidic capillary network remains to construct the two dimensional network of diverging and converging channel bifurcations. Analytical and physiological precedents exist to inform the design of a fluidic capillary network. Murray's law[29-31] (eqn. 4.1) states that the work required to drive fluid through a channel bifurcation is minimized when the diameter of the parent channel (D_p) and the diameters of the daughter channels (D_1, D_2, …., D_n) satisfy the following relationship.

$$D_P^{\,3} = D_1^{\,3} + D_2^{\,3} \tag{4.1}$$

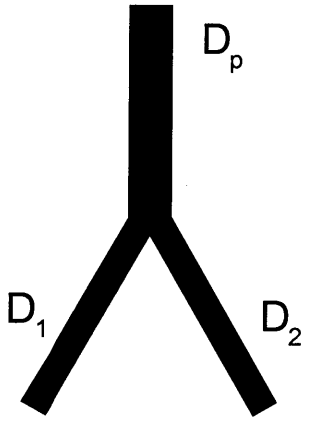

Figure 4.1: Bifurcation geometry and notation for Murray's Law, eqn. 4.1

Murray's law, which is applicable for symmetric and asymmetric branches, may be derived by several distinct analytical approaches, including minimization of the shear stress at a single bifurcation, and minimization of the total pumping work required to drive fluid through a capillary tree.[31]

Morphological data across multiple animal species, including humans, suggests a consistent pattern of branching ratios and vessel lengths unique to the pulmonary arterial system.[31-33] Previous work has shown a characteristic linearity of arterial diameter on a logarithmic scale across 15 orders of branching (equivalent to "levels" in a symmetrically bifurcating tree).[31, 32] On the basis of this morphological data, the scaling laws that govern the relative diameters of channels in a biological capillary system show excellent agreement with the scaling law set forth by Murray's law.[31] Murray's law was chosen as

a starting point for the design of the microfluidic capillary network based on its well-demonstrated mathematical rigorousness and excellent agreement with physiological data.

4.1.1 Scaling laws: geometric limitations

Murray's law is derived for the particular case of Poiseuille flow in cylindrical channels. Because the cylindrical geometry is not representative of the square, high aspect ratio channels encountered in microfluidic devices, several methods were attempted to translate the rectangular microfluidic channel cross sections into appropriate cylindrical analogs for Murray's law. One analogy commonly used to approximate the diameter of non-cylindrical channels is the hydraulic diameter, defined as:

$$D_H = \frac{4 * Area}{Perimeter} = \frac{4 * w * h}{(2h + 2w)} \tag{4.2}$$

where h is the channel height and w is the width. One important limitation of the hydraulic diameter is its asymptotic nature; at aspect ratios (w/h) greater than approximately 5, D_H approaches a limit equal to 2*h. A second approximation to Murray's law was to simply replace the 'cylindrical diameter' in eqn. 4.1 with the channel width. Ultimately, the method that was used was based on equating the fluidic resistance of a rectangular channel with that of a cylindrical channel to obtain a 'diameter' that was approximately analogous to a particular channel width, as will be described in greater detail in the following section. Since Murray's law essentially minimizes the resistance of a capillary network to fluid flow, the strategy of equating resistances was believed to be an optimal approach to minimizing shear stress in a rectangular geometry.

4.2 Microfluidic capillary design evolution

The evolution of 2D microfluidic capillary designs which were fabricated and tested for the photolytic oxygenation module is shown in fig. 4.2. The network labeled 'A' was a preliminary design used to test the upper limits on packing density (100 μm height, 200 μm wide, and 50 μm separation) which revealed stiction problems between the PDMS and mold surface associated with the high density of channels. Network 'B', which consists of 100 μm wide channels with 150 μm separation, represents what was determined to be an optimal packing density, from a fabrication standpoint. The asymmetric nature of the fluid inlet and outlet was non-optimal, however, from a fluid dynamics perspective. Trapped air bubbles were a persistent problem in this design. Designs 'C-D' represent the introduction of symmetry in the capillary design, which significantly reduced the formation of air bubbles in the microchannels. Network 'E' is the culmination of refinements in packing density, symmetry, and optimal branching ratios (based on Murray's law, eqn. 4.1). At it's lowest branching level, device 'E' consists of 16 parallel channels. Design 'E' displays an increased length in the narrow "gas exchange" central portion of the chip. The increased gas exchange length accomplished a five-fold increase in oxygen delivery capacity over the same total capillary length as device 'D'. Device 'F' consists of an extension of Device 'E' to 4 times the number of capillaries (64 in the gas exchange portion), whereas 'G' is a refined version of device 'F' with optimal branching ratios at the largest-width channels.

Device 'G' is noteworthy because of the novel support structure used to support the very high aspect ratio (> 20:1) channels at the inlet and outlet. This support structure, visible at higher magnification in Figure 10, consists of a grid of PDMS micro-pillar supports which prevent the ceiling of the channels from collapsing and occluding the channel. This design offers greater flexibility in implementing high flow-rate chips with very high aspect ratio channels.

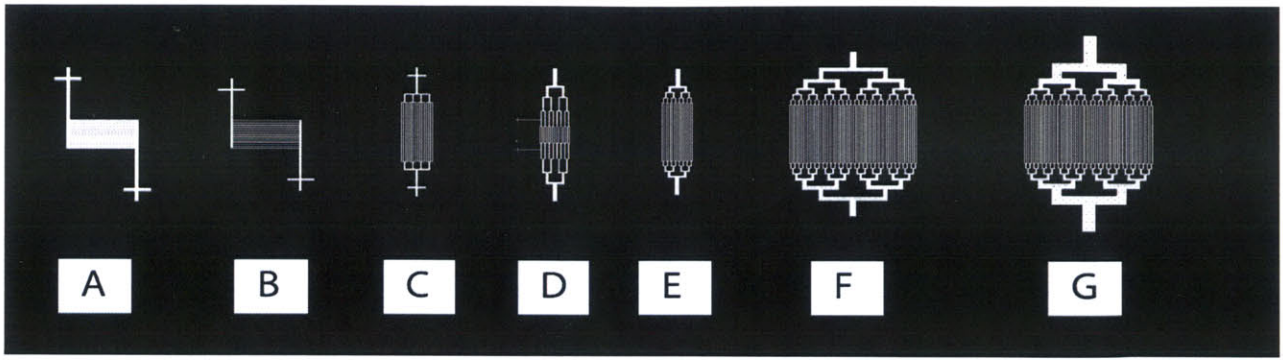

Figure 4.2: Evolution of arborizing microchannel designs.

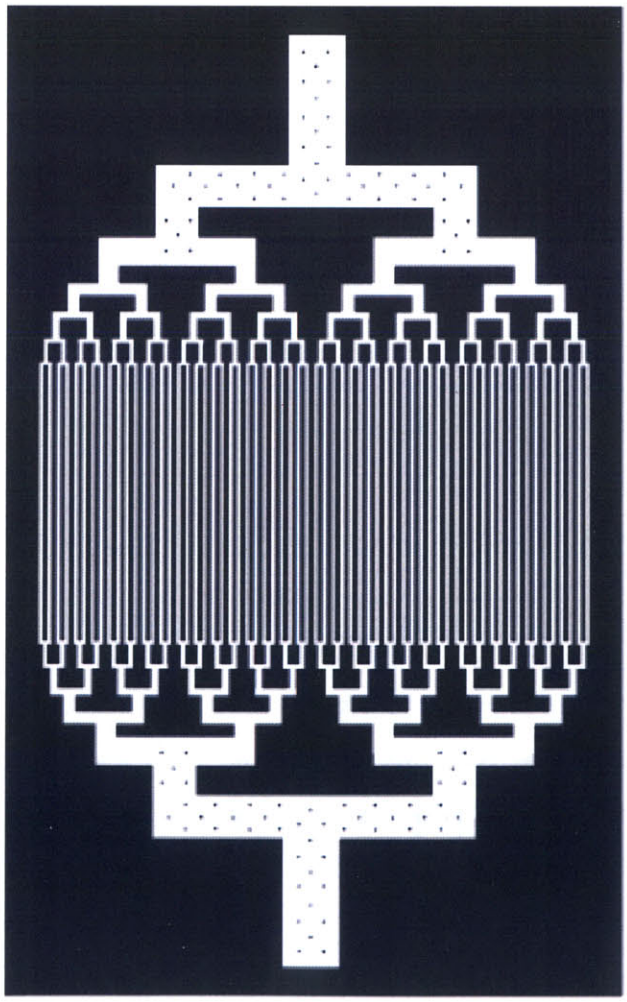

Figure 4.3: Photolithography template (mask) of microfluidic construct depicted in fig. 4.2G

The device shown in fig. 4.2G was the lithography design used in the bulk of experiments described throughout the remainder of this thesis. An important point should be made concerning the choice of bifurcation angle, shown in detail in fig. 4.3. Realizing that shear stress, fluid stagnation and recirculation, and other non-desirable fluid dynamical properties would be substantial due to the 90 degree bend angles chosen for the device design, it was nevertheless decided to fabricated this design as an experimental starting point, from which nearly all other bifurcation geometries would represent an improvement. Because the availability for blood to be used in experimentation was delayed nearly until the end of this research, the bulk of the experiments that follow were conducted with water, which never necessitated improvements to the channel branching angle, with regard to hemocompatibility. Various later iterations on the capillary network design will be discussed in the final chapters of the thesis, in the section concerning blood testing and microfluidic hemocompatibility.

In the following sections, we demonstrate the simulated flow behavior through the device that was ultimately chosen as a primary design, fig. 4.2G/4.3.

4.3 Calculated flow properties in microfluidic construct

The microfluidic network shown in fig. 4.3 is a symmetrically branching tree with seven levels of binary bifurcations. A 'symmetric' network implies that, at a given bifurcation, the two daughter vessels have an equal width. In such a capillary tree, the "rank" of a bifurcation is defined to be the number of bifurcations separating the channel from the lowest level of the tree, plus one. Rank 7, for instance, represents the largest channel, the fluid inlet, whereas rank 1 implies the smallest channel, in the gas-exchange portion of the device. Starting with the defined width of channels at rank 7, Murray's law is solved for channels of decreasing rank, yielding a set of hydraulic diameters. Using a resistance approximation for Poiseuille flow in rectangular ducts, a 2-dimensional width was extrapolated from the capillary hydraulic diameter solutions. The resistance approximation is as follows: An inlet channel diameter is created with a specified

diameter, and six levels of decreasing channel diameter are determined according to Murray's law, eqn. 4.1. With the exception of the smallest channels, whose length is determined from mass transfer analysis described in following sections, the lengths of branch ranks 2-7 are determined from a normalized regression fit to morphological data from Huang.[32] The rectangular channel width is calculated by equating the Poiseuille fluidic resistance for a cylindrical channel with diameter D, from Murray's law, and the fluidic resistance for a rectangular channel with width w and height h = 100 μm.

Poiseuille fluidic resistance:

$$\text{Cylindrical:} \quad R = \frac{8\mu L}{\pi\left(\frac{D}{2}\right)^4} \tag{4.3.A}$$

$$\text{Rectangular:}^{34} \quad R = \frac{\mu L(h+w)^2}{8(hw)^3}\left[96 - 95\frac{h}{w} + 56\left(\frac{h}{w}\right)^2\right] \tag{4.3.B}$$

The variables L and μ are the channel length and fluid viscosity, respectively. Blood is a non-Newtonian shear-thinning fluid,[35, 36] which, for the purposes of this analysis, is approximated with the viscosity of water. Equating eqns. 4.3A and 4.3B and solving for the width, w, yields the set of optimal channel widths for channel 'levels' 1-6. The resulting widths, used to construct the network of fig. 4.3, are plotted in fig. 4.4, along with the diameter 'D' which was determined from Murray's law and used to calculate the cylindrical resistance of eqn. 4.3.A. Figure 4.4 shows the channel diameter for a network extrapolated by regression analysis from morphological data on and adult male lung, per Huang et al,[32] as well as the channel diameter for a capillary network determined from Murray's law and the rectangular channel width determined via eqn. 4.3 in analogy to Murray's law.

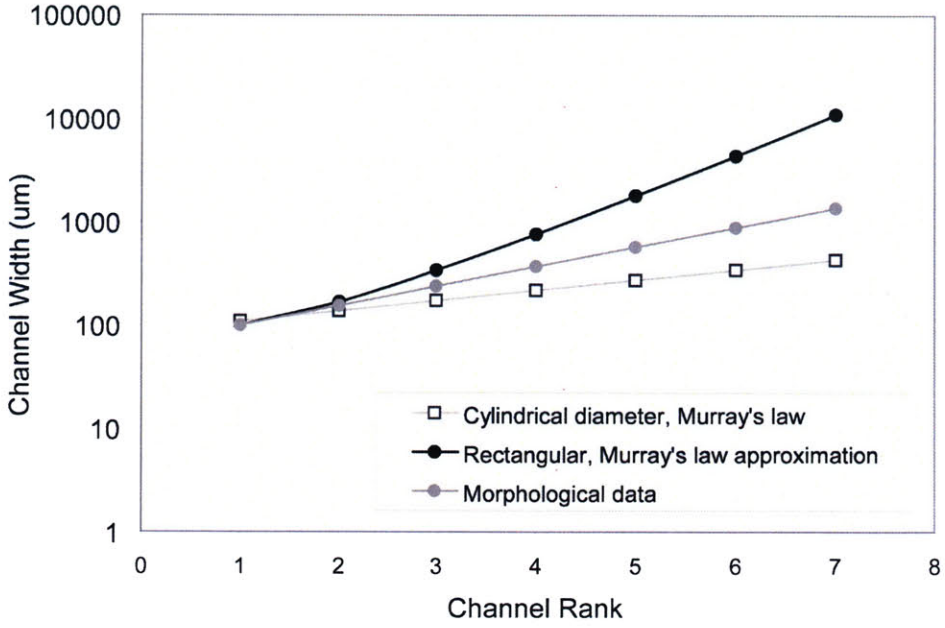

Figure 4.4: Channel dimension (width or diameter) versus channel rank for morphological data, capillary network based on Murray's law, and capillary network based on rectangular approximation to Murray's law.

At higher channel ranks, rectangular widths diverged at an exponential rate because of the large fluidic resistance of the rectangular channel shape. At the highest channel ranks, 6 and 7, the large channel width (~1cm) predicted by the Murray's law approximation had to be constrained to a maximum value of 2 mm due to fabrication constraints.

The net cross sectional area at each branching rank is shown in fig. 4.5A. Net area is represented as a ratio of the total cross sectional area at branch 'i' to the cross sectional area at the inlet (rank 7). The datasets shown in figs. 4.5A and 4.5B are identical to those shown in fig. 4.4. The significantly larger aspect ratios of the morphological data correspond to the dramatic exponential increase in the number of channels at lower channel ranks for physiological capillary networks. For instance, rank 1 in our fabricated model corresponds to 64 channels of 100μm width; from properly scaled morphological data, rank 1 corresponds to an identical diameter of 100 μm, with approximately 1500 channels. In the microfluidic device, a similar increase in the net area ratio at diminishing channel ranks is precluded by the 2-D nature of the microfluidic network.

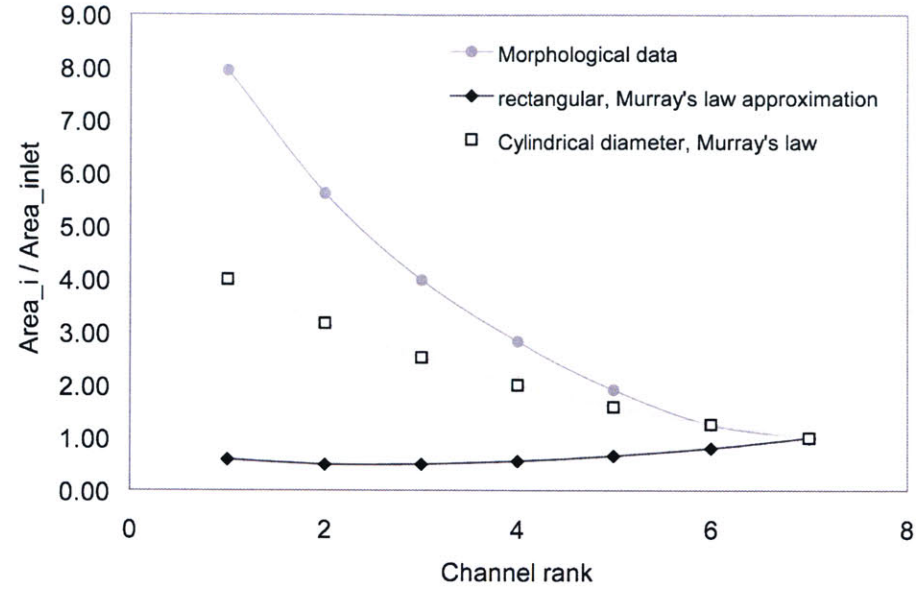

a)

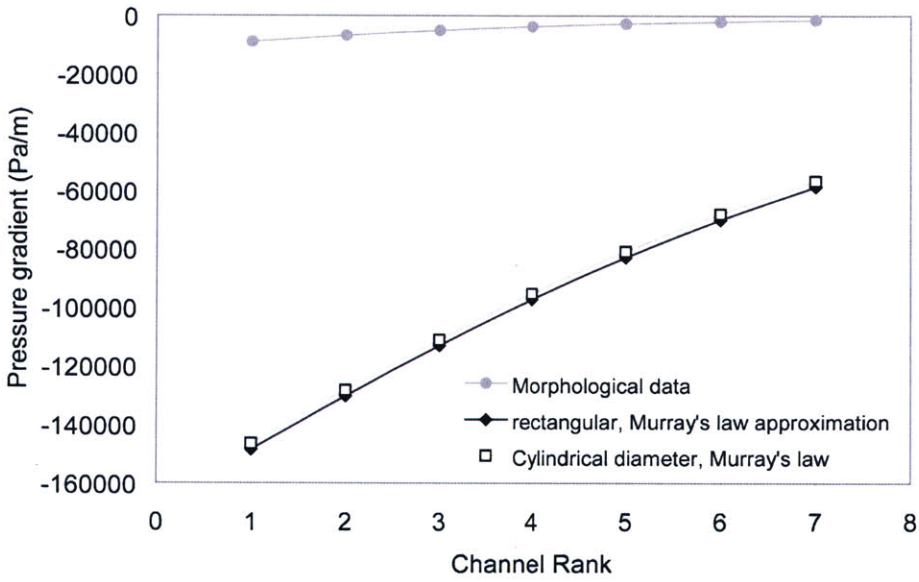

b)

Figure 4.5: Calculated channel characteristics as a function of branching rank.. a) Net area ratio for extrapolated morphological data and the fabricated microchannel network of fig. 4.3. b) The (absolute) axial pressure gradient increases smoothly and continuously with decreasing channel rank.

Figure 4.5B shows the calculated pressure gradient at each consecutive channel branch of the three capillary networks under consideration. The pressure drop in a

channel is proportional to the flow rate and the fluidic resistance. Since the rectangular channel widths were calculated by equating the rectangular resistance with the cylindrical resistance determined from Murray's law, it is clear that both sets of data should demonstrate an identical variation in pressure gradient with channel rank. Both the pressure gradients predicted from morphological data and Murray's law/rectangular approximation display an identical trend in pressure gradient, increasing gradually at progressively smaller channel sizes. The greater pressure gradients in the Murray's law/rectangular networks are due to the significantly lower net area expansion in these networks, as demonstrated in fig. 4.5A.

In Poiseuille flow, the maximum (wall) shear stress is proportional to the pressure gradient in the axial direction (x):

$$\tau_X = -\frac{R}{2} * \frac{\partial P}{\partial x} \tag{4.4}$$

where P is the pressure field, R is the radius, and 'x' is the axial direction of flow. The fluidic pressure gradient in fig. 4.5B decreases smoothly and continuously, indicating that, in theory, the rectangular capillary network avoids the adverse pressure gradients (shocks and rapid pressure drops) that cause excessive shear forces and cell damage.

Chapter 5

Optimization and Characterization of Mass Transfer

5.1 Dimensional analysis of convective mass transfer

The rate of oxygen uptake in the fluid channels of the microfluidic oxygenator is dependent upon several geometric and material properties of the microfluidic device. At high flow rates, rapidly moving fluid quickly carries diffused O_2 down the channel length. As a result, convective transport dominates diffusive transport and a longer overall channel length is required for O_2 to diffuse across the width of the channel and saturate the blood. Passive oxygenation was employed to generate a flux of O_2 into the fluidic channel and determine the minimum channel length necessary to achieve oxygen saturation. In the experiments that are described here, buffered water was used as the working fluid, as opposed to blood. Future work will examine the oxygenation characteristics of blood flow in microchannels. The following variables affect the rate of O_2 uptake in a convective environment: channel height, channel length, fluid flow rate, and PDMS membrane thickness and permeability. During passive oxygenation, the concentration of pure O_2 in the upper gas microchannels is much higher than the dissolved concentration of oxygen in the fluidic channels, resulting in a large concentration gradient across the PDMS membrane separating the two channel layers. Because of this large concentration gradient, O_2 diffuses readily across the thin PDMS membrane and the membrane resistance, which is a function of its permeability and thickness, can be effectively neglected. With this simplification, the mass transport in the microoxygenator is determined solely by the channel geometry and the fluid flow rate. Dimensional analysis of the mass transport problem can further simplify this analysis such that the channel length, height, and flow rate are reduced to a single dimensionless

variable that may be experimentally altered to characterize the oxygenator performance, as follows.[37] The dimensionless Navier-Stokes equation, which characterizes the velocity profile for flow between stationary boundaries, is written in dimensionless form as:

$$\mathrm{Re}(\tilde{v}\cdot\tilde{\nabla}\tilde{v}) = -\tilde{\nabla}\tilde{P} + \tilde{\nabla}^2\tilde{v} \tag{5.1}$$

$$\mathrm{Re} \equiv \frac{\rho V H}{\mu} \tag{5.2}$$

where Re is the Reynold's number, v is the velocity vector, P is the pressure, V is the mean fluid velocity, H is the channel height, ρ is the fluid density, μ is the viscosity, and the superscript ~ implies non-dimensionality. The dimensionless concentration profile is defined by the steady species conservation equation:

$$\mathrm{Pe}\tilde{v}\cdot\tilde{\nabla}\Theta = \tilde{\nabla}^2\Theta \tag{5.3}$$

$$\mathrm{Pe} \equiv \frac{VH}{D} = \mathrm{Re}\,\mathrm{Sc} \tag{5.4}$$

$$\mathrm{Sc} \equiv \frac{\mu}{\rho D} \tag{5.5}$$

where Pe is the Peclet number, Θ is the dimensionless species concentration, and Sc is the Schmidt number. Equation 5.1 implies that the velocity must have the following dependence:

$$\tilde{v} = \tilde{v}(\tilde{x}, \mathrm{Re}, \mathrm{geometric\_ratios}) \tag{5.6}$$

where x is the position, and geometric ratios refer to the dimensionless ratios of all the lengths necessary to define the system geometry – in this case, the channel length L divided by the channel height H. Equation 5.3 implies that the dimensionless concentration depends on the same parameters as the velocity, with the addition of the Peclet number:

$$\Theta = \Theta(\tilde{x}, \mathrm{Re}, \mathrm{Pe}, \mathrm{geometric\_ratios}) \tag{5.7}$$

Since eqn. 5.4 defines the Peclet number as a function of Re, eqn. 5.7 may be further simplified:

$$\Theta = \Theta(\tilde{z}, \mathrm{Pe}, \mathrm{geometric\_ratios}) \tag{5.8}$$

If the mass transfer coefficient that is used to determine the concentration in eqn. 5.8 is taken to be an averaged value along the length of the channel, then the dependence on the position z disappears and the Peclet number and geometric ratios may be represented in a single dimensionless parameter L*:

$$L^* = \frac{L}{H}\frac{1}{Pe} \tag{5.9}$$

The convective mass transfer coefficient for the microfluidic oxygenator is completely characterized by the single dimensionless parameter L* given by eqn. 5.9. The simplest experimental variable to manipulate in eqn. 5.9 was the velocity, which manifests in the Peclet number and was altered by varying the flow rate. Variations in the independent parameter L* for all of the following experimental data were all achieved by varying the flow rate.

5.2 Experimental protocol and introduction to oxygen sensing

The experimental protocol for evaluating the oxygen transfer was as follows. Fluidic and gas connections to the microfluidic device were made with 20G steel pipe segments connected to 0.2"/0.6" ID/OD Tygon tubing (Cole-Parmer). A syringe pump (Harvard Pump 11, Harvard Apparatus) was used to deliver a constant fluid flow rate to the device.

Reservoirs of DI water were bubbled with N_2 and O_2 gas for a minimum of 10 minutes, providing sufficient time for the oxygen concentration to stabilize and provide 0% and 100% oxygen references. The DO concentration in oxygen-saturated water was calculated to be approximately 42.5 ppm, equivalent to 42.5 mg L^{-1} in a dilute aqueous solution at STP. To test oxygenator performance, deoxygenated water was flowed through the system while the oxygen gas supply to the device's upper channels was cycled on and off, using an oxygen sensor to detect the gas concentration at the oxygenator outlet. The previously defined dimensionless length, L*, was the independent experimental variable that was varied to obtain different concentration data points. The fluid flow rate, which appears in the denominator of the L* term through the velocity value in the definition of the Reynolds number, Re, was used to vary L*. Fluid volume flow rate was varied from 50 μL min^{-1} – 5 mL min^{-1} during oxygenator testing, while properties of the channel geometry and membrane thickness were held constant. Two types of O_2 sensors, a Clarke electrode sensor and a custom-built optical O_2 sensor, were evaluated for the measurement of gas concentration. Both sensors are discussed in detail below.

5.3 Clarke electrode oxygen sensing

5.3.1 Operational principles of Clarke electrode oxygen sensing

Clarke electrodes are amperometric-type sensors which operate by chemically reducing dissolved oxygen in the fluid sample to generate a measurable current proportional to the concentration of oxygen. A potential is applied between two electrodes (typically Pt, Ag or AgCl) at a level suitable to reduce O_2 at the working electrode (~ 650 mV). Numerous chemical species oxidize at a potential similar to oxygen, making the electrode sensor undesirably sensitive to additional elements in the analyte. Additionally, the working area of the electrode surface may be fouled by other species in the fluid, a particularly relevant concern with biological fluids like blood where a proteinaceous film might adsorb and impair the electrode function.[38] To prevent electrode fouling and achieve

higher specificity for oxygen, an O_2 permeable polymer membrane such as PTFE (Teflon) is sealed in place between the electrodes, immersed in an electrolyte solution (KCl), and the analyte fluid. The concentration of O_2 in the fluid drives diffusion across the membrane, where O_2 in the electrolyte solution is reduced at the electrode surface.

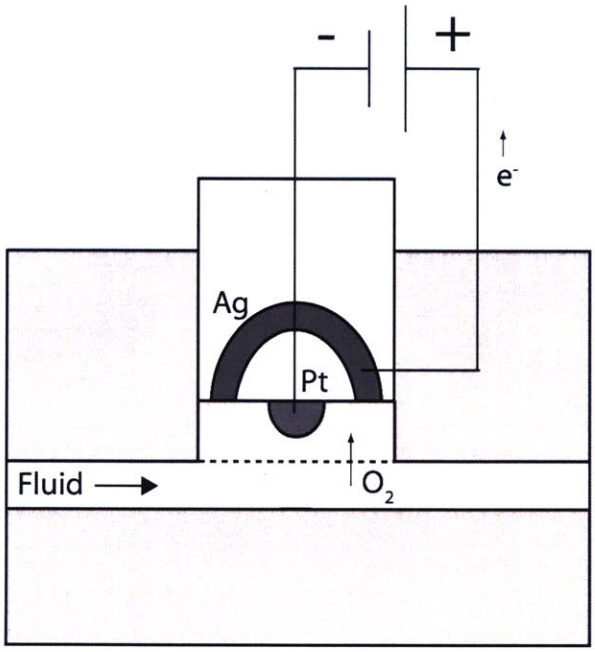

Figure 5.1: Schematic of Clarke electrode operation

Micro-reactor Clarke electrodes were purchased from Lazar Labs (DO-166FT) which featured a low volume (80 μL) chamber, magnetic stir bar for mixing of the analyte solution, and fluidic connections to allow fluid flow-through and real-time sensing. Tests of oxygenator performance using Clarke electrodes were performed by flowing deoxygenated water through test devices at various flow rates, recording the voltage reading from the electrode, then turning on the O_2 supply to the upper gas channels of the microfluidic device and recording the change in voltage reading. Upper and lower limits on the electrode voltage readings were obtained by flowing oxygenated and deoxygenated water (from bubbling, as previously described) through the device with the oxygen supply shut off. Assuming a linear relationship between voltage and oxygen

concentration, the voltage readings obtained experimentally were scaled between the 0% and 100% voltage readings to obtain a concentration value.

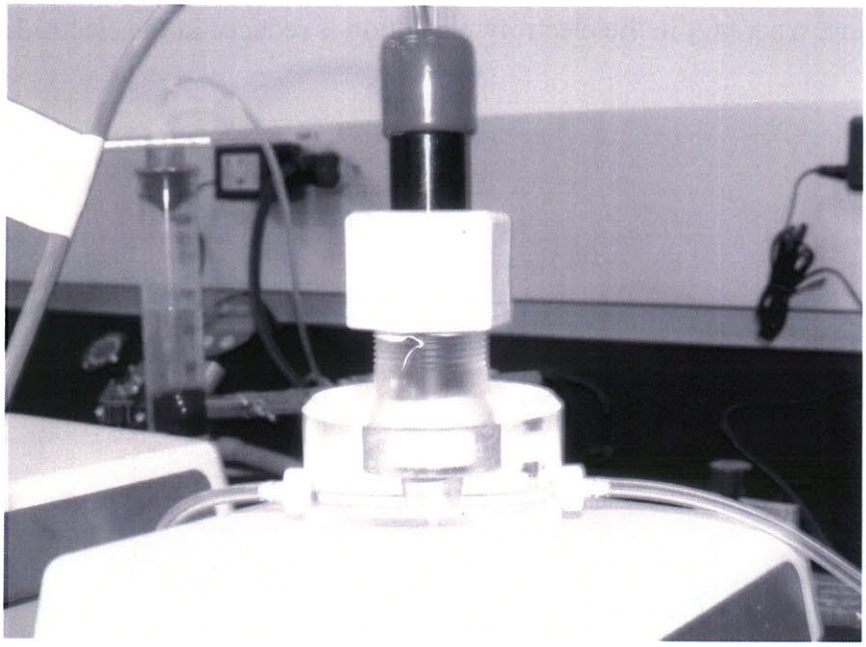

Figure 5.2: Clarke O_2 electrode connected in-line with fluid circuit

5.3.2 Inherent limitations of the Clarke electrode

Testing in the manner described above yielded a plot of percent oxygenation versus effective oxygenator channel length, L*, fig. 5.3. Although the trend of the data was approximately the desired linear relationship, the scatter in the data was non-ideal and indicated a large degree of uncertainty in the experimental results.

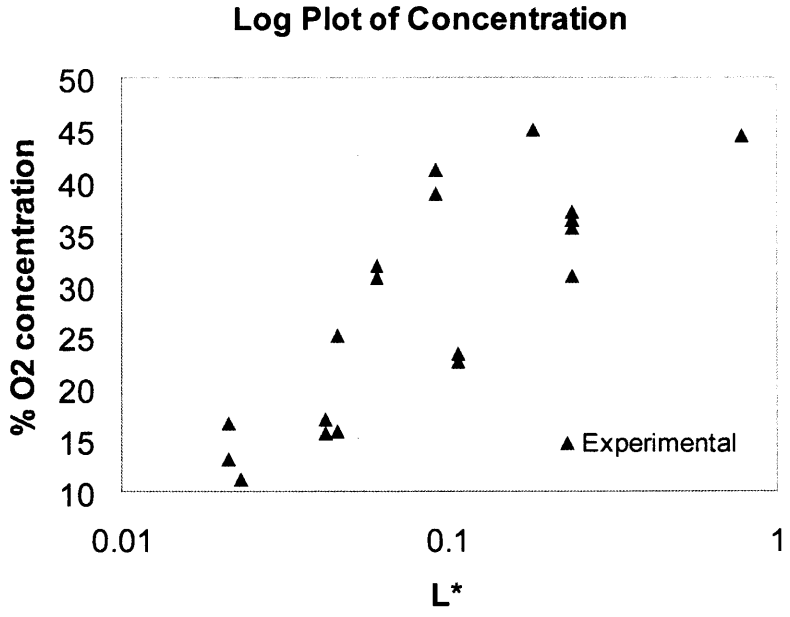

*Figure 5.3: Clarke O_2 electrode data for percent oxygenation vs. L**

Further research into amperometric oxygen sensing revealed multiple non-ideal characteristics of Clarke electrodes which account for the inconsistency of the data in fig. 5.3.[14] For micro-device applications involving biological fluids and micro-liter/min flow rates, amperometric sensors are generally undesirable because of difficulty in miniaturization, susceptibility to membrane fouling by organic matter, significant drift, analyte depletion, and signal variability at low flow rates.[39] The experimentation that has currently been conducted involves only buffered water as a working fluid, meaning that organic fouling of the electrode membrane was not a cause of concern. However, oxidation of the electrode surface area after prolonged usage and electrolyte depletion were both likely to have been responsible for inconsistency between data, which was taken over the course of several days. A more important concern relates to the fundamental method of operation of the amperometric electrode. The Clarke sensor operates by reducing oxygen, according to the following reaction:

$$\text{Ag anode:} \quad 4Ag^0 + 4Cl^- \longrightarrow 4AgCl + 4e^- \qquad (5.10A)$$

$$\text{Pt cathode:} \quad O_2 + 4H^+ + 4e^- \longrightarrow 2H_2O \qquad (5.10B)$$

The generation of an amperometric signal relies on the consumption of the O_2 analyte, which depletes the concentration of O_2 in the sample. For macroscopic applications with a large volume of sample or a high sample concentration, this is not a concern – mixing of the sample ensures a continual supply of O_2, and the quantity consumed is inconsequential compared to the concentration of DO in the entire sample. However, in a flowing medium at very low rates, the consumption of O_2 by the electrode is not balanced by the convection of fresh O_2 to the sample chamber, and the sensor signal is attenuated by the diminished availability of O_2. The result is a severe signal dependence on flow rate, as shown in fig. 5.4.

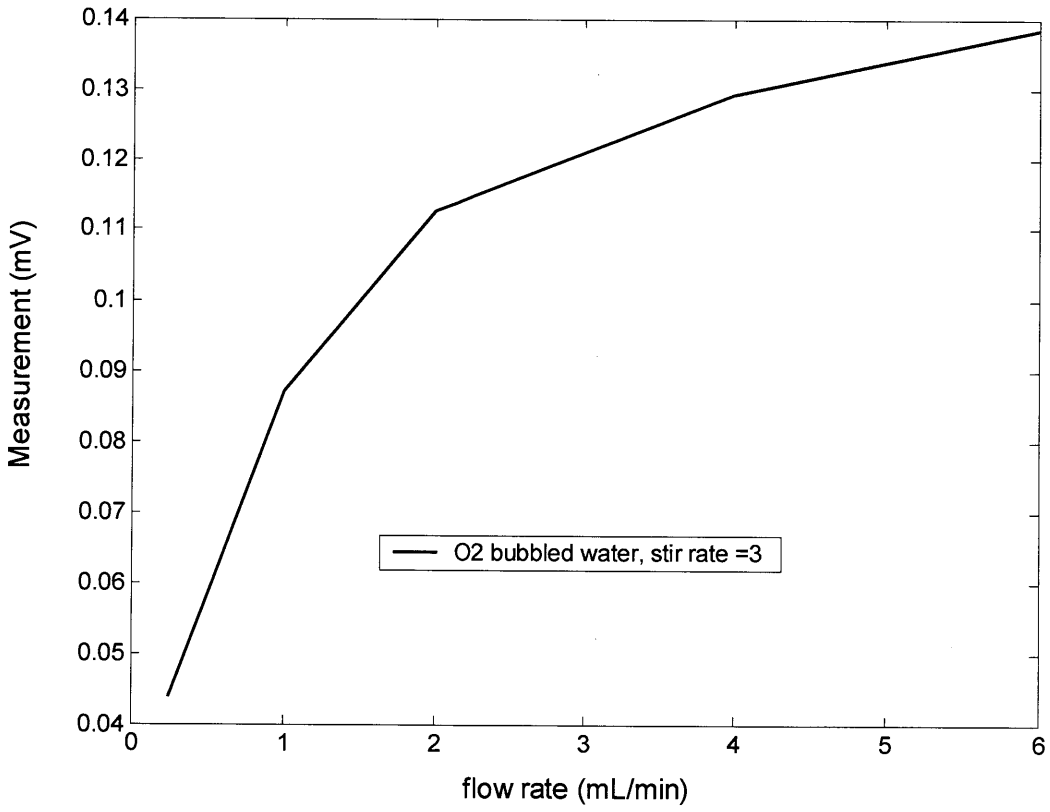

Figure 5.4: Variation of electrode signal with flow rate, due to O_2 consumption

Figure 5.4 corresponds to data recorded for a constant oxygen concentration, which should theoretically yield a constant mV signal value. Despite magnetic stirring, there is a severe signal attenuation below flow rates of approximately 6 mL/min. Above

6mL/min, the signal appears to asymptote to a stable value. A flow rate of 6 mL/min represents an upper limit of flow rates considered in the micro-oxygenator application, meaning that the analyte consumption by the Clarke electrode is a very non-desirable characteristic for this application.

5.4 Optical oxygen sensing

Due to the non-desirable characteristics of amperometric oxygen sensing in this particular application, it was necessary to develop a new and more appropriate sensing technique. The work of Harry Lee, a graduate student in Electrical Engineering at MIT, in the development of integrated oxygen sensors for a microfluidic mixing chamber, stimulated interest in the topic of optical oxygen sensing. Sensors based on optical excitation and detection of an embedded oxygen-quenched luminescent dye offer fast, linear response and immunity to drift from consumption of O_2. These ideal characteristics have generated intense interest in luminescent chemical sensors, which have been demonstrated and marketed in a variety of configurations for various biological, environmental, aerospace, and other applications.[15, 40-48]

5.4.1 Operational principles of luminescent optical oxygen sensing

The principle underlying optical oxygen detection is the excitation of a luminescent dye suspended in a micro-porous polymer matrix. Polymer encapsulated oxygen-quenched lumophore sensors have been demonstrated with numerous luminescent dyes and substrates. Early work in the area focused on polyaromatic hydrocarbon complexes,[49] more recent work on ruthenium diimines,[47, 50] and most recently on Pt and Pd porphyrin complexes.[15, 40, 42, 43] Quantification of dissolved oxygen content is determined by measurement of either the degree of luminescent intensity quenching or the luminescent lifetime. Of the previously mentioned dyes, the transition-metal (Pd, Pt) porphyrin complexes are most compatible with inexpensive solid-state optical components (LED and Si photodiode). Detection can be performed either directly with fixed optics above

and below the device[51] or remotely with a fiber optic probe[42, 43]. Both techniques allow non-invasive, real-time monitoring. In the present work, the former approach was employed to take advantage of the optical clarity of the polydimethylsiloxane (PDMS) microfluidic device and achieve a higher signal to noise ratio through better light coupling. Optical sensing pads were deposited at the inlet and outlet of the oxygen-transfer portion of the microfluidic device. By monitoring the inlet and outlet gas concentration at various flow rates, the convective mass transfer characteristics of the device are characterized as a function of effective oxygenator "length". While previous work has demonstrated optical sensing of gaseous oxyen[42, 44] and sensing of static fluids in biological microenvironments,[41, 45, 52] the application of an integrated optical sensor for detection of dissolved oxygen in a flowing medium with active mass transfer is a unique development.

In regards to this research, an integrated optical luminescent oxygen sensor was designed to meet objectives related to the development of a microfluidic photolytic oxygenation module. Specifically, the O_2 sensor was employed for experimental characterization of the mass transfer efficiency of microfluidic oxygenator designs. In future work on the photolytic oxygenation module, we imagine that the luminescent sensor could be fabricated with integrated solid-state excitation and detection optics in a fully encapsulated and operational device like that shown in fig. 3.2. An integrated micro-sensor in the final photolytic oxygenator design would allow for real-time detection of blood-gas levels, providing a detection element for a feedback-control loop. Such a feedback-control loop would be a valuable safety/redundancy feature, allowing modulation of photolytic oxygen generation via the applied electrical bias potential and UV light intensity to ensure the reliable delivery of the necessary concentration of oxygen to the bloodstream.

In addition to the photolytic oxygenator module, there exist other applications for which the integrated microfluidic O_2 sensor would be particularly relevant. A micro-device capable of oxygen sensing and delivery provides the potential for closed-loop control and regulation of biochemical species, a particularly important and unique development for the types of biological micro-device and tissue engineering applications previously reported in literature.[16, 53]

5.4.2 Fabrication of optical sensor

Of the various available chemical dyes suitable for oxygen detection, Pt octaethyl-porphyrin-ketone (PtOEPK, Frontier Scientific) was selected for its desirable optical properties and compatibility with readily available and inexpensive solid-state electronic components. The chemical structure of PtOEPK is shown in fig. 5.5.

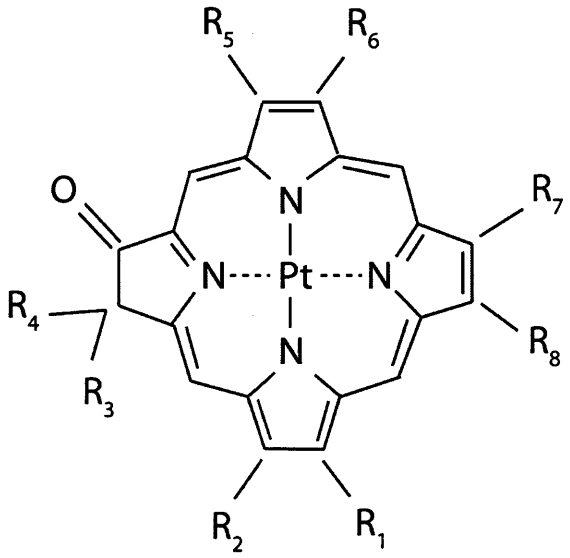

Figure 5.5: Platinum octaethylporphyrin ketone (PtOEPK)

PtOEPK exhibits an absorption peak in the visible spectrum at 590 nm, making it compatible with high-intensity yellow LED's.[42] The emission peak of PtOEPK is 760 nm, detectable by Si photodiodes. The longwave shift of the PtOEPK dye, relative to other luminescent materials, permits effective optical filtration with standard broadband filters. Additionally, PtOEPK shows greater long-term photostability than previously developed dyes.[40] Oxygen permeable films of PtOEPK-polystyrene (PtOEPK-ps) were prepared by dissolving 1 mg of the dye in 1 mL of a 5% solution of polystyrene in toluene. A variety of different sensor configurations were tested to achieve optimum sensor response time and mechanical integrity of the PtOEPK film. Figure 5.6 shows five different iterations on the sensor placement. The left hand image shows a cross

sectional view of the sensor and channel, with the arrow indicating direction of flow. The right hand side is a vertical view of the channel and sensor alignment.

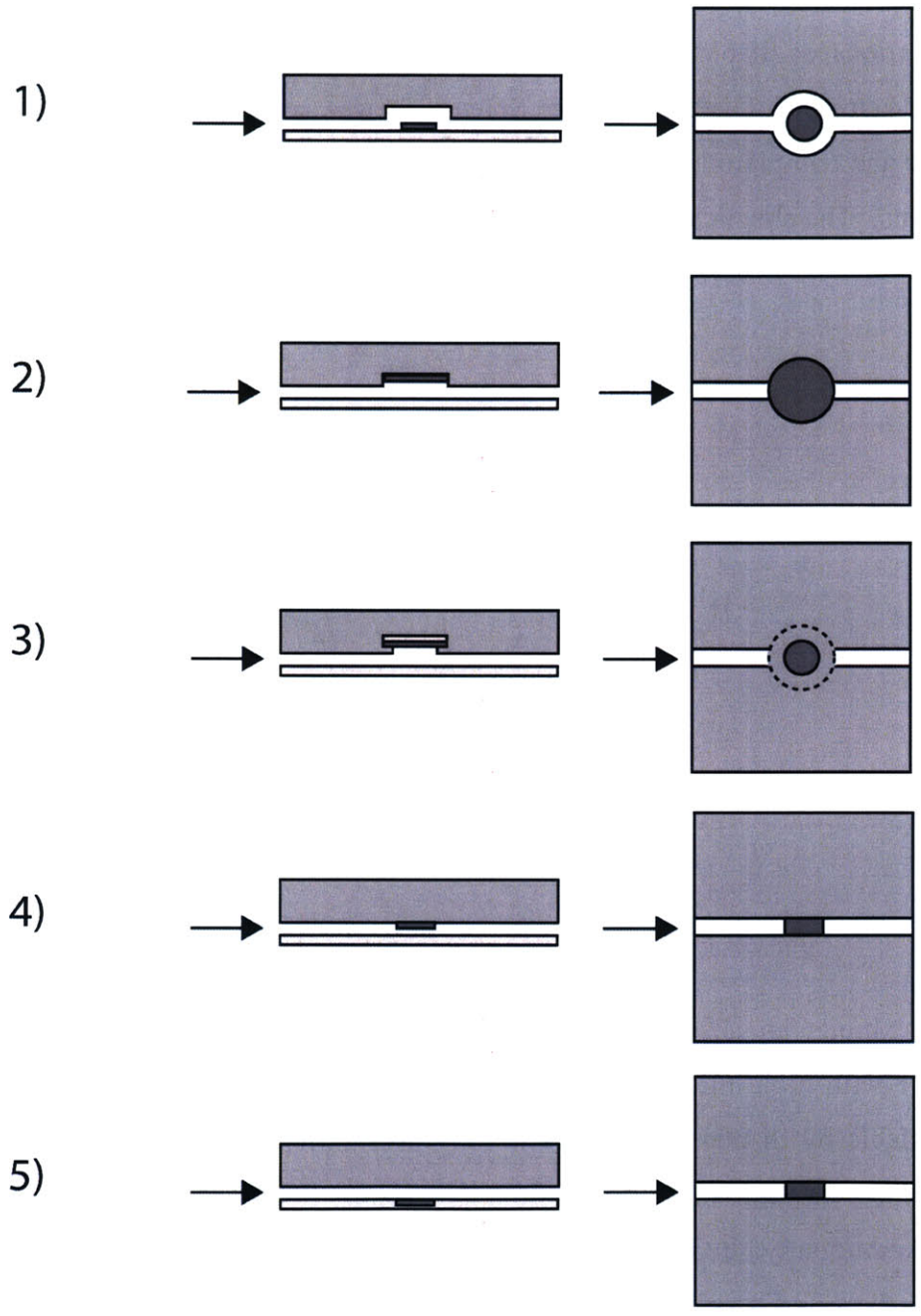

Figure 5.6: Cross sectional (left) and vertical views (right) showing configuration of PtOEPK-polystyrene sensor within microfluidic device. Arrow indicates direction of fluid flow between PDMS and glass substrate.

The first iteration of sensor design (1) was based upon PtOEPK-ps pads deposited upon a blank glass slide, centered beneath a circular flow chamber molded into the PDMS chip. This design exhibited serious limitations. The adhesion between the PtOEPK-ps pad and glass slide was very poor, making the sensor prone to release under fluid flow. Additionally, the circular PDMS reservoir was easily filled with air bubbles which were difficult to remove and interfered with the operation of the sensor. Design two (2) used the same PDMS flow chamber as design 1, but attempted to solve the problem of sensor adhesion by depositing the sensor material directly into the PDMS flow reservoir. Adhesion of the polystyrene to the PDMS surface was better than adhesion to the glass surface, but not sufficiently strong, and detachment remained a problem. Air bubble trapping remained problematic. Design three (3) addressed the bubble problem by using a smaller flow reservoir which was less prone to trapping air bubbles because of less fluid stagnation in the smaller volume. Mechanical adhesion was addressed by an elaborate method of first applying the PtOEPK-ps sensor to a miniature glass slide, then sealing the slide into the PDMS device with overlapping PDMS edges to hold the slide in place. This design proved excessively difficult to fabricate, and was prone to leaking. In the fourth design (4), the flow chamber was eliminated entirely and PtOEPK-ps was deposited directly into the top of the PDMS channel, essentially a simplification of design 2. This design was mechanically robust and trapped no air bubbles, but had a significant limitation. The high permeability of oxygen in PDMS means that O_2 is rapidly pulled from fluids entering the microfluidic chip and absorbed into the walls of the device. This occurs until sufficient time has passed that enough O_2 has been absorbed by the PDMS that the polymer has equilibrated with the gas concentration of the entering fluid. At low flow rates, this equilibration process can take a considerable amount of time. It was observed that when the PtOEPK-ps sensor is in direct contact with the PDMS channel walls, it too displays a very long equilibration time – in effect, the sensor detects the concentration of O_2 in the surrounding PDMS, in addition to the fluid, meaning that stabilization can occur very slowly. To bypass the slow rate of sensor equilibration, design 5 repeated the geometry of design 4, with the sensor deposited in contact with the glass slide rather than the PDMS. Isolating the sensor from contact with the PDMS achieved nearly a ten-fold decrease in equilibration time for the sensor, facilitating much

faster and more practical experimentation. To overcome the adhesion problems between glass and polystyrene that were encountered in design 1, the surface of the glass slide in the desired sensor location was etched with a dilute hydrochloric acid solution prior to depositing the sensor and plasma bonding the device. The acid etch removes several microns of glass, creating a microporous surface that promotes considerably better adhesion of the PtOEPK-ps layer. Additionally, etching of the surface effectively "submerges" the sensor in the glass slide, such that the sensor film does not occlude the cross sectional area of the microchannel and is subject to lower shear stress. An SEM of the glass microporous surface is shown in fig. 5.7. A tendril of the PtOEPK-ps film is visible in lower right hand corner of the image.

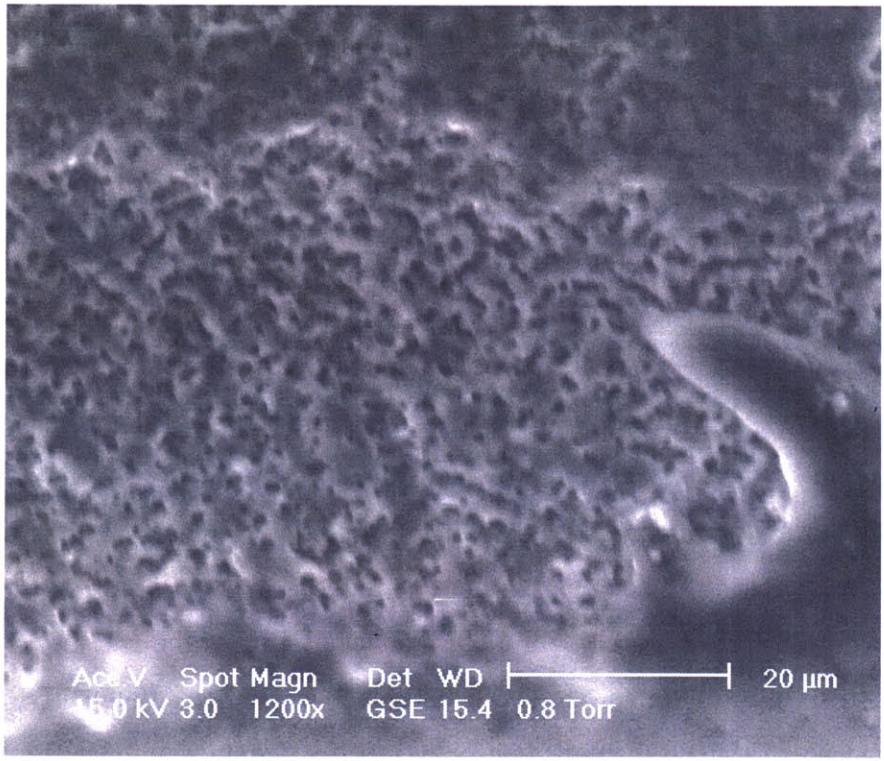

Figure 5.7: Microporous etched surface of glass slide used as substrate for PtOEPK-ps sensor film. An edge of the Pt-OEPK-ps material is visible in lower and lower-right sides of the image.

To fabricate devices according to design 5, a standard microscope slide was prepared as a substrate for the sensor using photolithography techniques. Positive photoresist (AZ 4620, Clariant) was spun to a thickness of 10 µm and developed to leave

two rectangular patches of glass exposed at the desired sensor locations on the glass slide. A commercially available dilute HCL glass etch (Armour Etch) was used to remove several microns of the glass surface, creating a micro-porous texture well suited to promoting mechanical adhesion between the glass substrate and the polystyrene matrix. A micropipette was used to apply 1-2 μL of the dye solution to the etched glass slide. After 10 minutes the solvent evaporated and acetone was used to strip the cured AZ mask from the glass slide, leaving a polystyrene/PtOEPK film of approximately 7 μm thickness. Acetone had a negligible effect on the integrity of the polystyrene-immersed dye. Figure 5.8 shows a spectrophotometer image of the absorbance peaks for two different PtOEPK sensors, one formed by pipetting of the PtOEPK-polystyrene solution onto a glass slide (blue), and the second formed by spin-coating a thin film of the same solution onto a glass slide at 3000 rpm (green). Both the pipetted ("Drops") sensor and spin-coated film sensor exhibit an absorption peak at 590nm, as well as additional absorbance in the lower wavelength UV band. Excitation light is optically filtered around 590nm to avoid excitation at lower wavelengths. Micro-pipetted sensor drops, the fabrication method that was ultimately selected for use in devices, are significantly thicker than the thin spun film, which accounts for the greater absorbance across the optical spectrum in fig. 5.8.

Oxygen-plasma bonding was employed to create a covalently bonded seal between the PDMS chip and glass slide (45 second exposure to plasma gas at the vacuum pressure of 100 mTorr). Completed microfluidic structures were stored in the dark to prevent photobleaching and degradation of the sensor's optical properties. A fully-assembled device is shown in fig. 5.9.

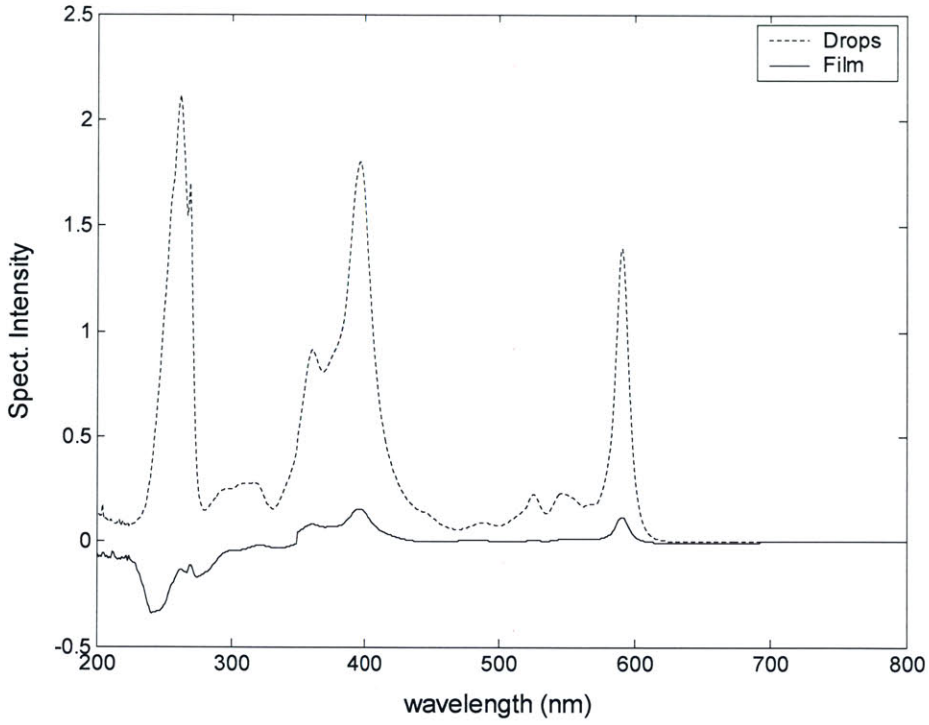

Figure 5.8: PtOEPK absorbance, demonstrating predominant peak at 590nm. The magnitude of absorbance is considerably larger for the thicker non-film sensor pad

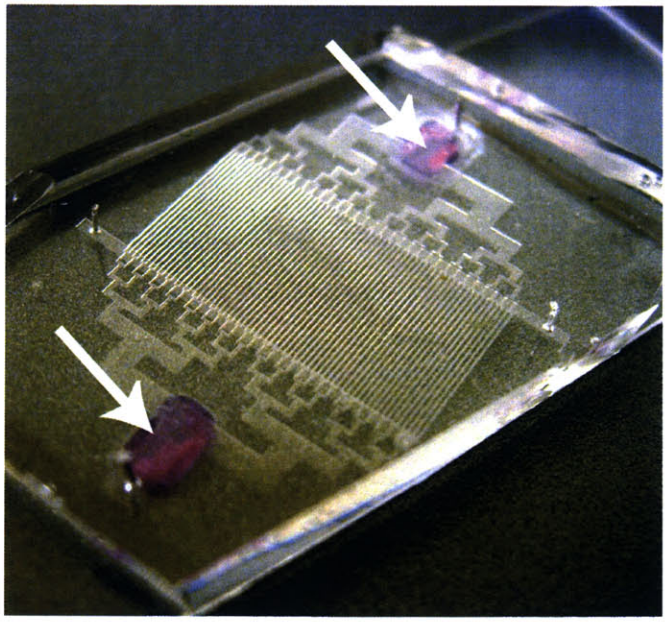

Figure 5.9: Multi-layer microfluidic device with fluidic channels and gas channels for passive oxygenation. Arrows indicate the location of integrated luminescent optical sensors at the device inlet and outlet. Approximate chip dimensions are 2.5 cm per side.

5.4.3 Optical and electrical apparatus

A LED-based optical excitation and detection system was fabricated to monitor oxygen content in the microfluidic chip upstream and downstream of the oxygenator channels. A 15° narrow-angle yellow/amber LED (590 nm, 2500 mcd, Ledtronic) was filtered by a BG39 Schott glass filter (CVI Laser) and positioned vertically directly above the sensor pad. A Si photodiode (S2386-44k, Hamamatsu) was positioned below the sensor, shielded, and filtered by an RG715 Schott glass long-pass filter. Analog electronics amplified and filtered the photodiode current signal, which was recorded in real-time along with the reference LED signal on a PC via a USB DAQ card (PMD-1608FS, Measurement Computing). The excitation LED was modulated at a frequency of 5 kHz, which allowed for phase-detection and low-frequency filtering in the signal conditioning circuitry to subtract any DC interference signal resulting from ambient lighting. Details of the analog circuitry developed for the sensor's signal processing is provided in Appendix B. The luminescent lifetime of the PtOEPK dye is on the order of 60 μs.[42] The decay time can be measured directly from the luminescent waveform by using a high speed spectrometer/data acquisition unit. Alternatively, the lifetime may be determined indirectly by measuring the phase shift between the 5 kHz excitation signal and the emission waveform at the same frequency. The dependence of the luminescent lifetime on the O_2 concentration manifests as a change in phase shift between the two signals. The relationship between phase shift (Θ) and lifetime (τ) in two common-frequency signals can be approximated by:

$$\tan(\Theta) = 2\pi \cdot \upsilon \cdot \tau \tag{5.11}$$

where υ is the modulation frequency. Phase-based lifetime detection precludes the need for high-speed (~10MHz) data acquisition hardware to directly measure the luminescent decay time. For the 5 kHz excitation and emission signals, phase shift was measured by digital lock-in detection in Labview. Additional post-processing was performed in Labview, which sampled the signal conditioning board at 20 kHz and performed various filtering of recorded data to produce averaged data points at a rate of 5 Hz. Lower averaged sampling rates (< 1 Hz) produced less noise, but limited the dynamic response

time of the system. The operation and organization of the Labview program is described in detail in Appendix C. The overall signal to noise ratio of the sensor is maximized by the compact, vertical arrangement of the sensing components, shown in fig. 5.10.

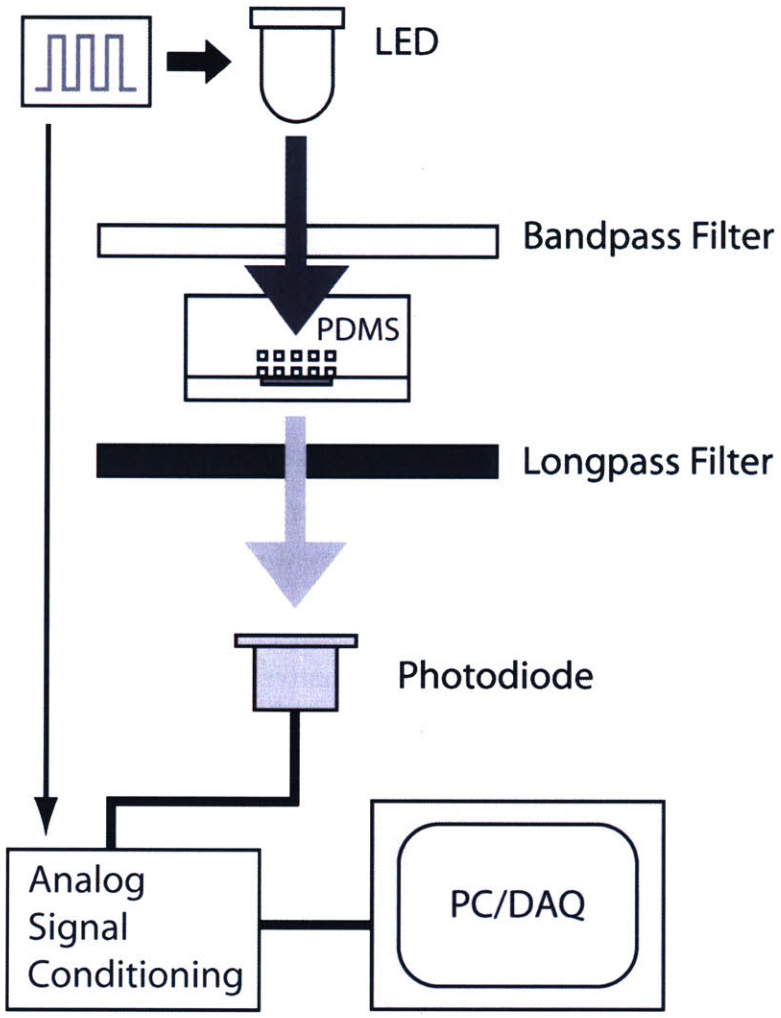

Figure 5.10: Optical and electrical components of the optical oxygen sensor detection system

Mechanical components and fixtures for the optical sensor were modeled in Solid Edge and machined at MIT's Pappalardo Lab. Images of the CAD solid model and the completed sensor assemply are shown in fig. 5.11.

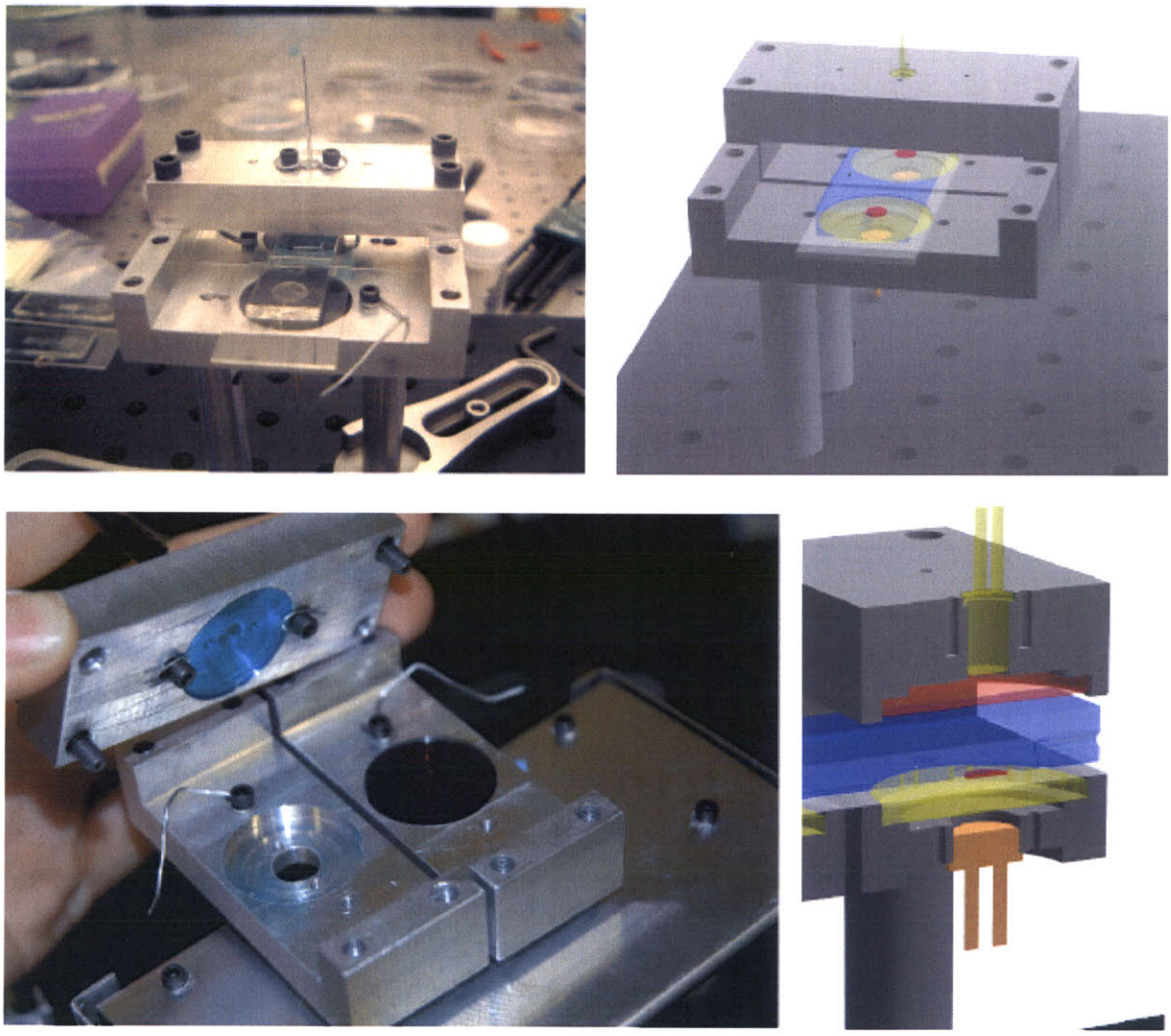

Figure 5.11: Optical sensor assembly: 1) Top left: sensor assembly with microfluidic chip in position between optical elements. Microfluidic chips are fabricated with sensing pads at the inlet and outlet, while the sensor assembly is shown with only one LED in position. For the majority of testing, only a single sensor was used at any given time. 2) Lower left: interior of sensor assembly showing bandpass and longpass glass filters. Metal box below sensor assembly is shielded analog signal processing circuitry. 3) Upper right: CAD model of sensor assembly developed prior to fabrication. 4) Lower right: cutaway view of sensor assembly interior visualizing the orientation of optical filters, microfluidic chip, PtOEPK-ps sensor pad, LED, and photodiode.

5.4.4 Methodology for oxygen detection: Phase-based lifetime sensing

The oxygen quenching process occurring in PtOEPK and other luminescent dyes is described by the Stern-Volmer equation for luminescent intensity (I) and lifetime (τ):

$$I_O/I = 1 + K^S_{SV}[O_2] = 1 + K^G_{SV} pO_2 \quad (5.12)$$

$$\tau_o/\tau = 1 + K^S_{SV}[O_2] = 1 + K^G_{SV} pO_2 \quad (5.13)$$

where K^S_{SV} and K^G_{SV} are the Stern-Volmer constants for solution and gas, respectively, I_O and τ_O are reference values in the absence of oxygen, $[O_2]$ is the oxygen concentration in solution, and pO_2 is the gaseous partial pressure of oxygen. Luminescent lifetime decay values were determined from the phase shift, as described by eqn. 5.11, and luminescent intensity was determined from the amplitude of the emitted 5 kHz waveform. Phase-based detection of luminescent lifetime was selected as the preferred detection scheme for all calibration and experimental measurements. A significant advantage of phase-based lifetime measurements is the inherent stability of the signal. The luminescent lifetime is an intrinsic property of the PtOEPK molecule and is therefore not susceptible to variation based on the intensity of incident light or heterogeneity in the thickness or distribution of the dye-polystyrene matrix. In contrast, the magnitude of the emitted luminescent intensity varies in proportion to the magnitude of incident light, meaning that small changes in alignment of the sensor pad can result in significant measurement errors. For this reason, the phase-based lifetime measurement is a considerably more reliable determinant of oxygen concentration than the luminescent intensity. An experiment, shown in fig. 5.12, was conducted to evaluate the relative stability of both the intensity and phase-based sensing methods. Deoxygenated water is flowed at a rate of 3 ml/min through the microfluidic chip. At t=100s, the passive oxygen supply is turned on and the oxygen concentration observed by the sensor should be, ostensibly, constant. The aluminum sensor mount is lightly shaken to perturb the alignment of the LED, sensor pad, and photodiode.

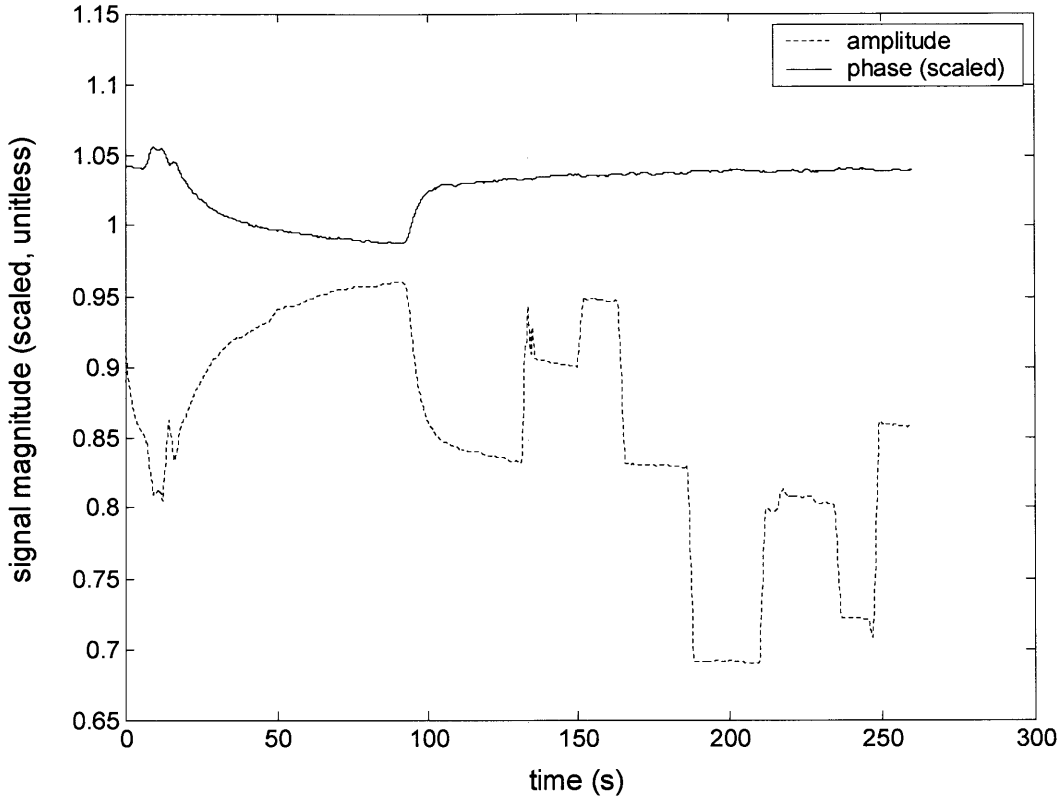

Figure 5.12: Signal stability comparison between intensity and phase-based optical oxygen sensing

Figure 5.12 clearly demonstrates the superior stability of the phase-based signal processing technique. The phase-based lifetime signal, which is scaled in the figure in order to be plotted on a common axis with the intensity signal, rapidly equilibrates following the onset of passive oxygenation at t=100s, and maintains a steady value despite agitation of the sensor. The intensity-based signal, alternatively, exhibits a pronounced DC offset with disruption of the optical alignment of the sensor. Because of its greater intrinsic stability, phase-based lifetime sensing was chosen as the preferred sensing technique for all experimental work.

5.4.5 A protocol for sensor operation and signal post-processing

A protocol of post-processing steps was formulated to extract oxygen concentration values from raw experimental data obtained using the microfluidic optical oxygen sensor. Raw sensor data is saved by Labview in the following form, where the y-axis indicates the phase shift and the x-axis indicates time.

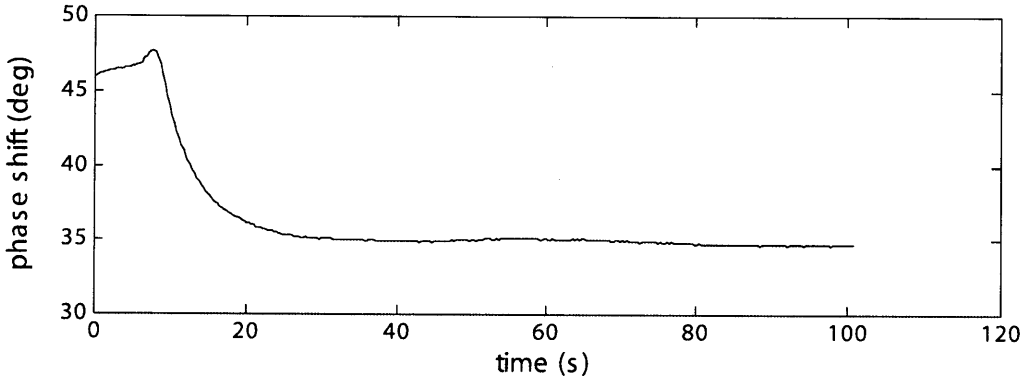

Figure 5.13: Raw data signal for detection of dissolved O_2 in fluid sample

Fluid mixtures containing a precise concentration of DO were obtained by making a volume-weighted mixture of purely deoxygenated and purely oxygenated water samples. For instance, a 40% DO sample would contain 4 parts oxygenated water to 6 parts deoxygenated water. While the flow rate was held constant, 5-point calibration tests were conducted by creating 0:4, 1:3, 2:2, 3:1, 4:0 mixtures of deoxygenated and oxygenated water, corresponding to 100%, 75%, 50%, 25%, and 0% DO, respectively. At a given flow rate, experimental data was obtained for each of these concentrations, as shown in fig. 5.14.

Equilibrium values for the phase shift at each O_2 concentration shown in fig. 5.14 are determined by inspection, shown in fig. 5.15.

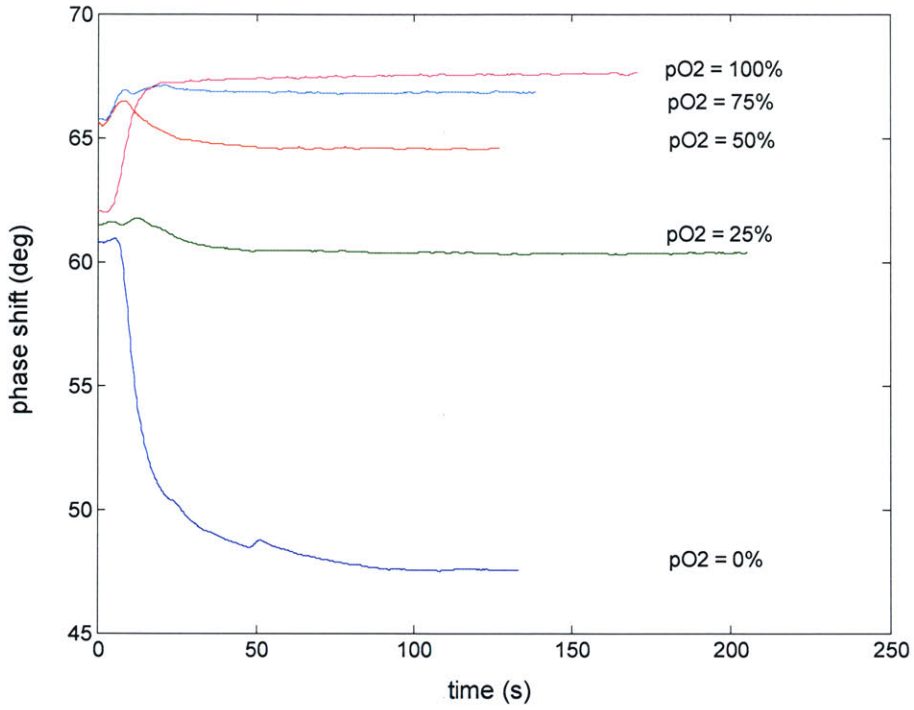

Figure 5.14: Raw calibration data for 5-point dissolved oxygen concentrations, flow rate Q=4 ml min^{-1}

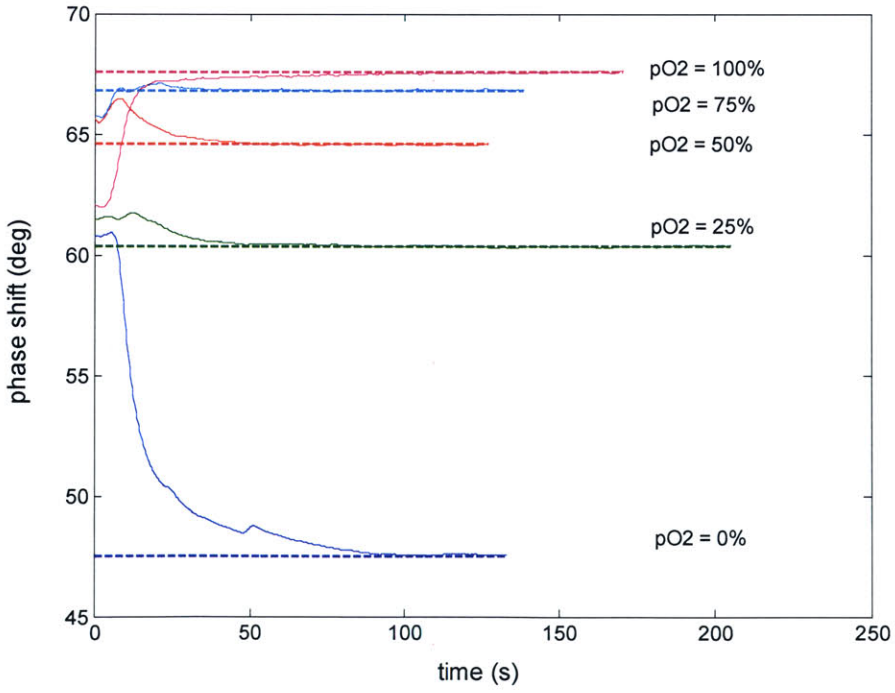

Figure 5.15: Equilibrium (asymptotic) value for phase shift in 5-point sensor calibration

The equilibrium values from fig. 5.15 are shown again for greater clarity in fig. 5.16a, as well as in fig. 5.16b, plotted against the fractional oxygen concentration.

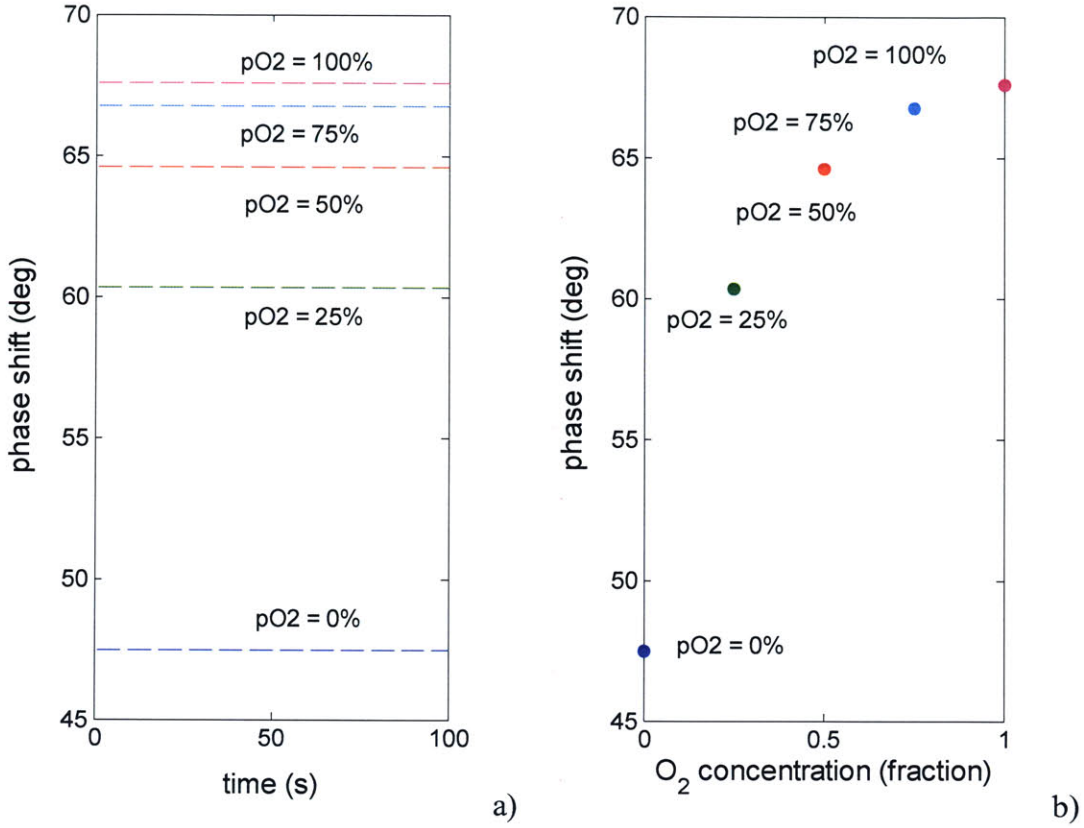

Figure 5.16: a): Equilibrium values for phase shift in 5-point sensor calibration b) Individual equilibrium data points plotted versus oxygen concentration fraction

The equilibrated experimental phase-shift values for concentrations between 0-100% O_2, shown in fig. 5.16b, represent the calibration curve for the optical oxygen sensor at a particular flow rate. However, experimentation revealed that the absolute value of the concentration measurement, in degrees, for a particular DO concentration, showed a dependence upon the flow rate. This is shown in fig. 5.17. The calibration datapoints for deoxygenated (diamond marker) and oxygenated (circular marker) samples are plotted versus flow rate through the device. Below a flow rate of 2.5 ml min^{-1}, the datapoints, deoxygenated in particular, begin to exhibit a dependence on the flow rate.

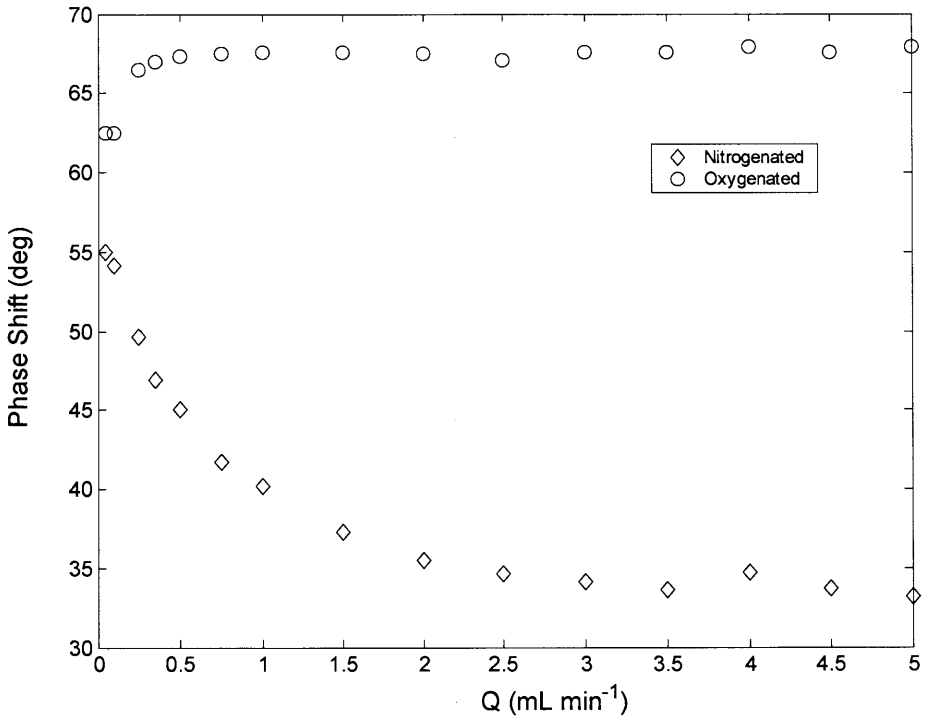

Figure 5.17: Calibration datapoints for deoxygenated water (diamond) and oxygenated water (circle) plotted versus flow rate Q. At flow rates below approximately Q=2.5 ml min^{-1}, the phase-shift begins to exhibit dependence upon the flow rate, particularly for the deoxygenated datapoints.

As fig. 5.17 indicates, lower flow rates correspond to a narrowing of the total dynamic operating range of the sensor as the oxygenated and deoxygenated reference curves approach each other. The operating range reduces from approximately 35°, at 5 ml min^{-1}, to 8°, at 0.05 ml min^{-1}. Originally, it was believed that the variation of the sensor signal at low flow rates was reminiscent of the flow-dependence problems experienced with the Clarke electrode sensor, fig. 5.4. However, there is no O_2 consumption associated with the optical sensor, meaning that it should, in theory, exhibit independence from the flow rate. The source of the problem was determined to be the O_2 capacitance of the PDMS, which has been previously described in regards to the slow response time of the sensor. At low flow rates, the concentrations of O_2 reaching the sensor are depleted by leeching into the PDMS (or, in the case of deoxygenated water, the fluid has increased its concentration by convecting O_2 away from the PDMS surface). The problem of

variability in the phase-shift signal was addressed by normalizing all sensor readings between calibration endpoints for deoxygenated and oxygenated water at a particular flow rate, according to eqn. 5.14:

$$\tau_{NORM} = \frac{\tau_{MEASURED} - \tau_{N2}}{\tau_{O2} - \tau_{N2}} \tag{5.14}$$

where τ_{N2} and τ_{O2} are the measured lifetime values, for a particular flow rate, of deoxygenated and oxygenated water samples. To evaluate the effectiveness of the microfluidic oxygenator, the repeatability of normalized sensor measurements was demonstrated across a broad dynamic range of flow rates. Figure 5.18 shows the calibration data for flow rates between 50 μL min^{-1} and 5 mL min^{-1}. For any particular flow rate, measured phase shift was normalized between the oxygenated (100%) and deoxygenated (0%) phase shift endpoints, like those shown in fig. 5.17.

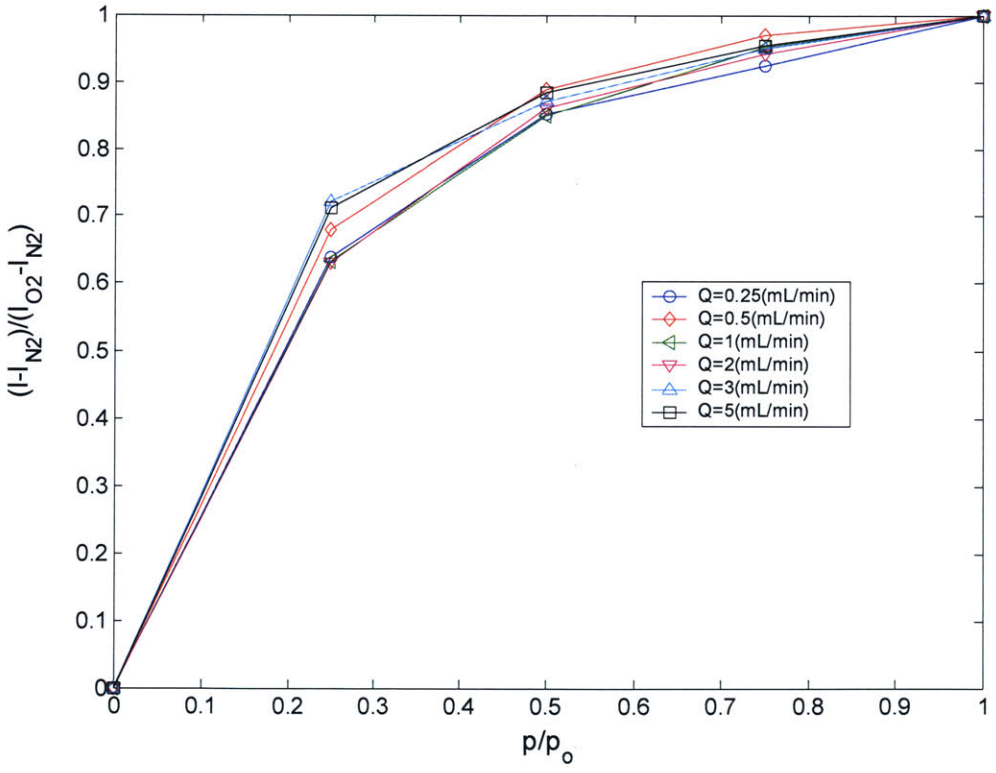

Figure 5.18: Oxygen sensor calibration curves normalized between upper and lower concentration bounds are shown to collapse consistently to a single curve, independent of flow rate.

Figure 5.18 shows the normalized 5-point calibration for 6 different flow rates. As opposed to the raw data points in fig. 5.17 which show variability across a broad range of flow rates, the normalized calibration curves in fig. 5.18 collapse consistently into a single curve. This permits simple two-point calibration of the sensor at any given flow rate. For the particular calibration curve shown in fig. 5.18, a 4th order polynomial fit is given by the following equation:

$$\tau_{NORM} = -3.618\rho^4 + 9.915\rho^3 - 10.012\rho^2 + 4.715\rho \tag{5.15.a}$$

$$\rho = {}^{p}\!/_{p_o} \tag{5.15.b}$$

It is important to note that while the phase-based sensing method employed to generate the calibration curve of eqn. 5.15 is a robust technique, this particular curve should be considered valid only for the devices with which it was generated. Future data should rely on repeated calibration curves for any different devices.

The method in which data points were gathered with the optical sensor can be summarized as follows:

1) Phase shift values recorded into Labview were converted to lifetime values, from eqn. 5.11.
2) At any flow rates under consideration, datapoints were taken with oxygenated and deoxygenated fluid to obtain the upper and lower bounds on the phase shift. After converting to lifetime values, these datapoints were used in normalizing experimental datapoints according to eqn. 5.14.
3) A 5-point calibration curve was generated using volumetric mixtures of oxygenated and deoxygenated fluid. While this calibration curve must be recorded at a single constant flow rate, it may be normalized by eqn. 5.14 and applied to normalized data recorded at any flow rate, as shown in fig. 5.18.
4) The desired experiments were performed at a variety of flow rates and data were first normalized then interpolated from eqn. 5.15 to obtain the O_2 concentration corresponding to the observed phase shift.

Resolution for the detection of dissolved oxygen varies in proportion to the flow rate. At 50 μL min^{-1}, the resolution is 780 ppb, or 0.92% of the full-scale oxygen concentration. At flow rates above 3 mL min^{-1}, the sensor approaches a maximum resolution of less than 120 ppb, 0.14% oxygen. The resolution and accuracy of the sensor for detection of both gaseous samples and fluidic samples compares favorably with results previously demonstrated.[44, 45] The range and resolution of the sensor make it ideally suited to detection of dissolved oxygen in biological fluids; blood, for example.

5.4.6 Sensor performance and calibration in gaseous samples

Sensor calibration was performed on both liquid samples and purely gaseous mixtures. While detection of dissolved oxygen concentrations in fluid samples is a more relevant capability in the context of this research, the measurement of O_2 concentration in gaseous samples provided a rapid and convenient validation of the sensor's operation. As opposed to the sensor pads for the integrated microfluidic device, the fabrication of which was described in the previous section, the sensor used for gaseous detection was fabricated simply by spin-coating a layer of PtOEPK-ps onto a glass slide, incorporating no PDMS microfluidic element. Spin-coating at a speed of 3000 rpm yielded a film of approximately 4 μm thickness. Tygon hoses supplying pure O_2 and N_2 were positioned above the sensor film, and the gas valves were alternately opened and closed to flood the sensor with the gaseous sample.

Figure 5.19 shows the dynamic response of the sensor to pure gas flow, and Figure 5.20 shows the corresponding 3-point Stern-Volmer curve. Oxygen partial pressure is normalized in Figure 5.20 between 0 and 1, corresponding to nitrogenated and oxygenated water, respectively. Figure 5.19 demonstrates high reversibility and nearly instantaneous dynamic response of the sensor under gas flow. The total time for 90% sensor equilibration is on the order of one second.

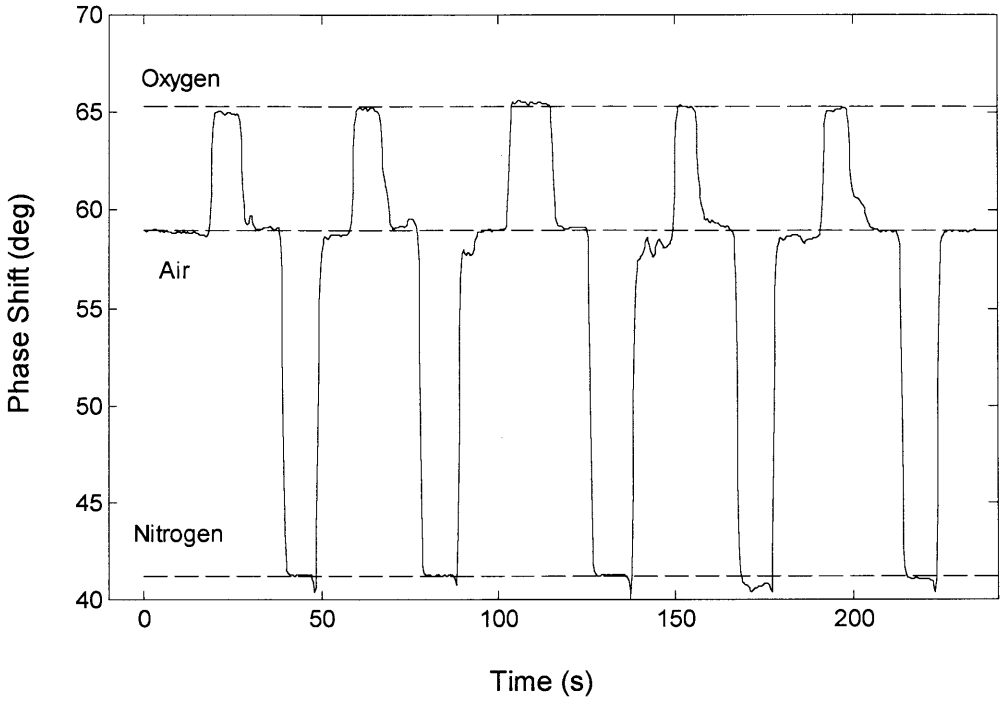

Figure 5.19: Thin-film PtOEPK-ps dynamic sensor response to pure gas flow. The sensor displays rapid dynamic response as well as a high degree of repeatability

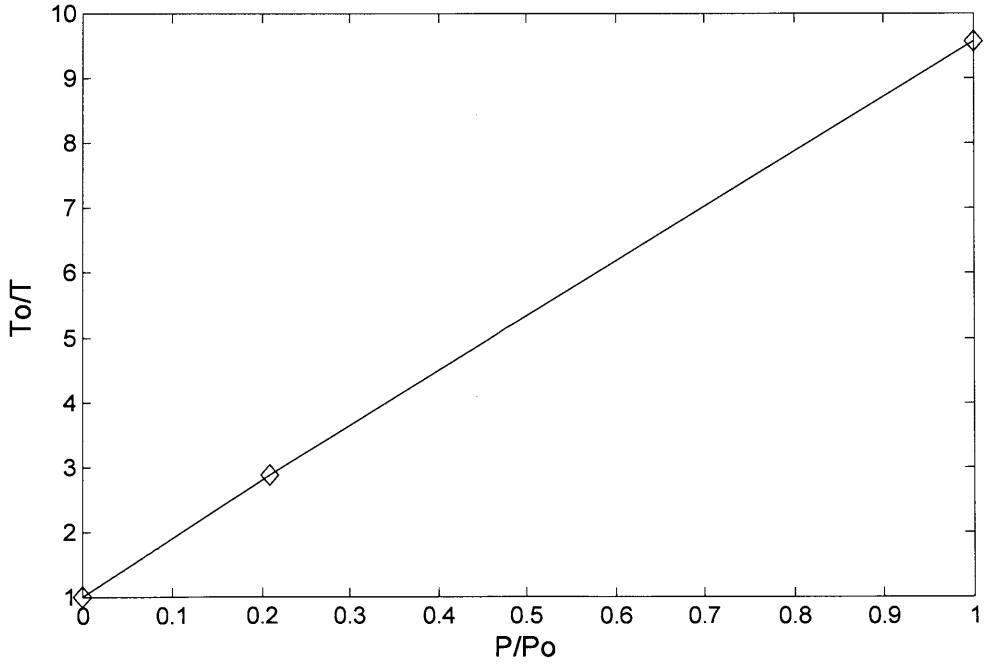

Figure 5.20: 3-point Stern-Volmer plot for thin-film PtOEPK-ps sensor under pure gas flow. The sensor demonstrates excellent linearity according to the Stern-Volmer relationship, eqn. 5.13.

Sensor linearity between normalized lifetime and oxygen concentration is excellent in detection of gaseous samples, as shown in fig. 5.20. Whereas non-linearity has been observed in many applications of polymer-suspended dye sensors,[44] the high diffusivity of oxygen in the hydrophobic polystyrene matrix improves the sensitivity of this sensor and contributes to its linearity across the entire operating range of oxygen concentration.

5.4.7 Sensor performance and calibration in fluidic samples

Detection of dissolved oxygen in aqueous samples was tested using calibrated concentrations of gas in buffered DI water. Dynamic sensor response is slower in an aqueous testing environment, varying from 30 seconds at flow rates above 4 mL min^{-1} to 3-5 minutes at flow rates below 500 μL min^{-1}. There are two primary causes for the slower dynamic response of the sensor in a flowing liquid medium. First, the interaction between dissolved oxygen (DO) and the luminescent dye is limited by the rate of DO diffusion through the fluid. Second, and most important for sensing across a broad dynamic range of flow rates, is the equilibration that must occur between the local oxygen content in the PDMS and the oxygen content in the fluid. PDMS is highly permeable to oxygen – thus its selection as a membrane material for the oxygenator. A convective process occurs between the PDMS walls of the microchannel and the oxygen-bearing fluid. Depending on the concentration of oxygen in the fluid entering the device, mass transfer from the walls occurs to either add or remove DO from the fluid. Equilibration occurs once the PDMS walls in the vicinity of the sensor have reached an oxygen concentration equal to the fluid. This process occurs more rapidly with faster moving fluids, resulting in the longer settling times at low flow rates. Through various sensor designs and methods of integrating the dye (fig. 5.6), we have accomplished nearly a ten-fold increase in speed of response over the evolution of the device. Figures 5.21 and 5.22 show the dynamic response of the sensor and Stern-Volmer plot, respectively, for detection of DO at a flow rate (Q) of 2 mL min^{-1}. Despite the slower dynamic response time for DO, sensor linearity remains excellent, as shown in figure 5.22.

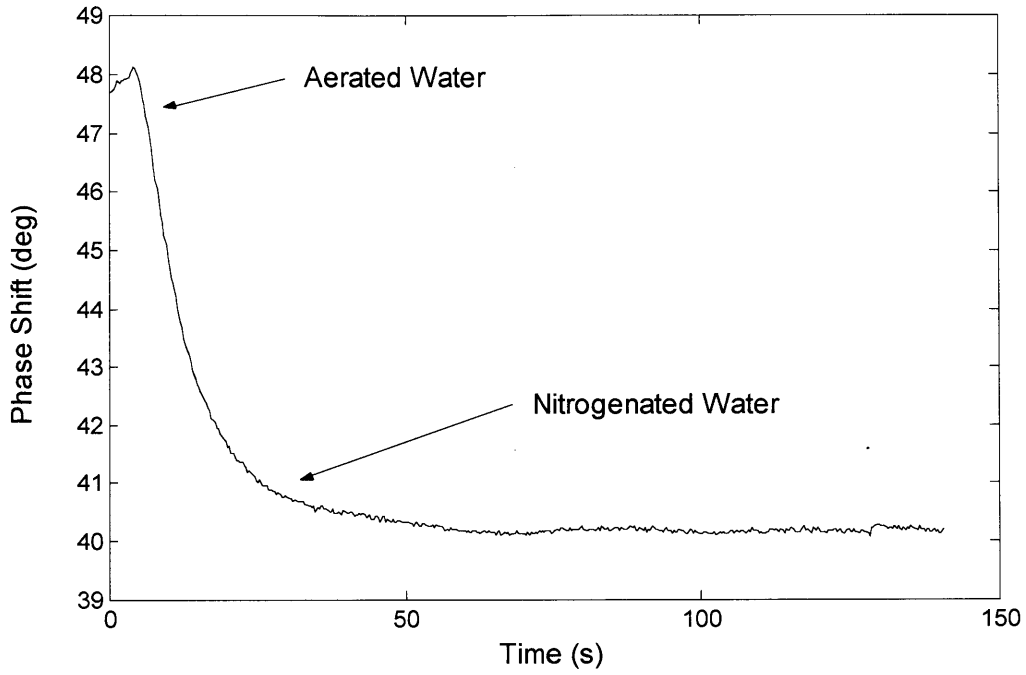

Figure 5.21: Dynamic sensor response for detection of dissolved oxygen in integrated microfluidic PtOEPK-ps oxygen sensor. $Q = 2$ ml min^{-1}

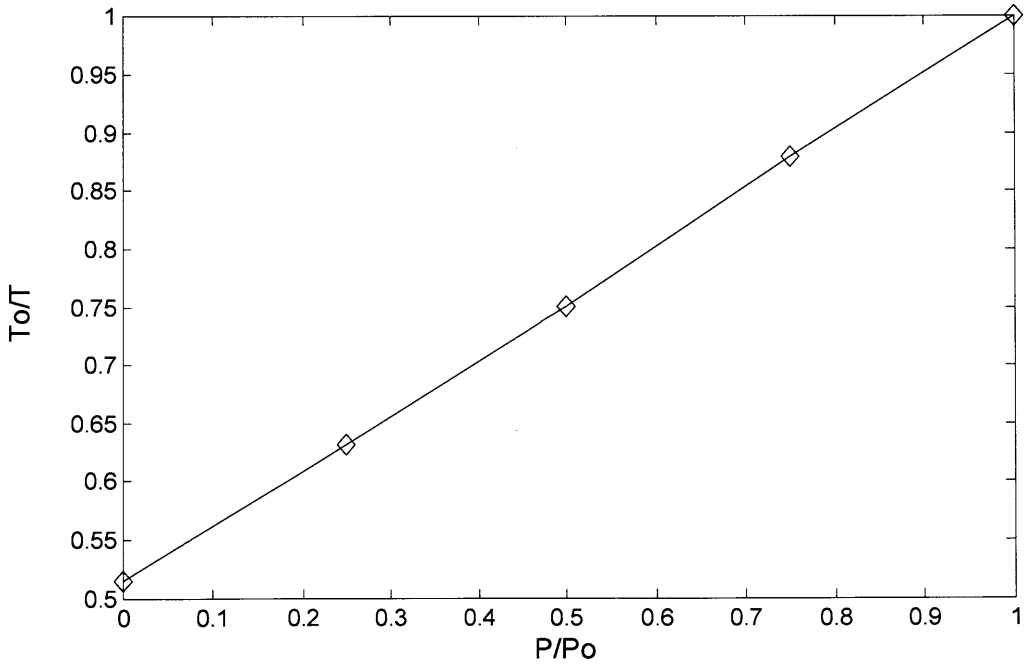

Figure 5.22: 5-point Stern-Volmer plot for integrated microfluidic PtOEPK-ps sensor in detection of dissolved oxygen. Despite the slower dynamic response of the sensor in a fluid environment, the sensor demonstrates excellent linearity according to the Stern-Volmer relationship, eqn. 5.13.

5.4.8 Photobleaching and stability

A final assessment of sensor function was made concerning its mechanical integrity and photostability. A common concern with lumophore-based chemical sensors is the degradation of the sensor's quantum efficiency following prolonged sampling and continual illumination. To evaluate the sensor's optical stability, a PtOEPK-polystyrene film was exposed to ambient air (20.1% O_2) and data was recorded over a period of 3 hours., pulsing the LED at 20 kHz, corresponding to nearly constant illumination. As shown in fig. 5.23, the intensity-based signal demonstrated a slight deterioration over the three hour course of the test.

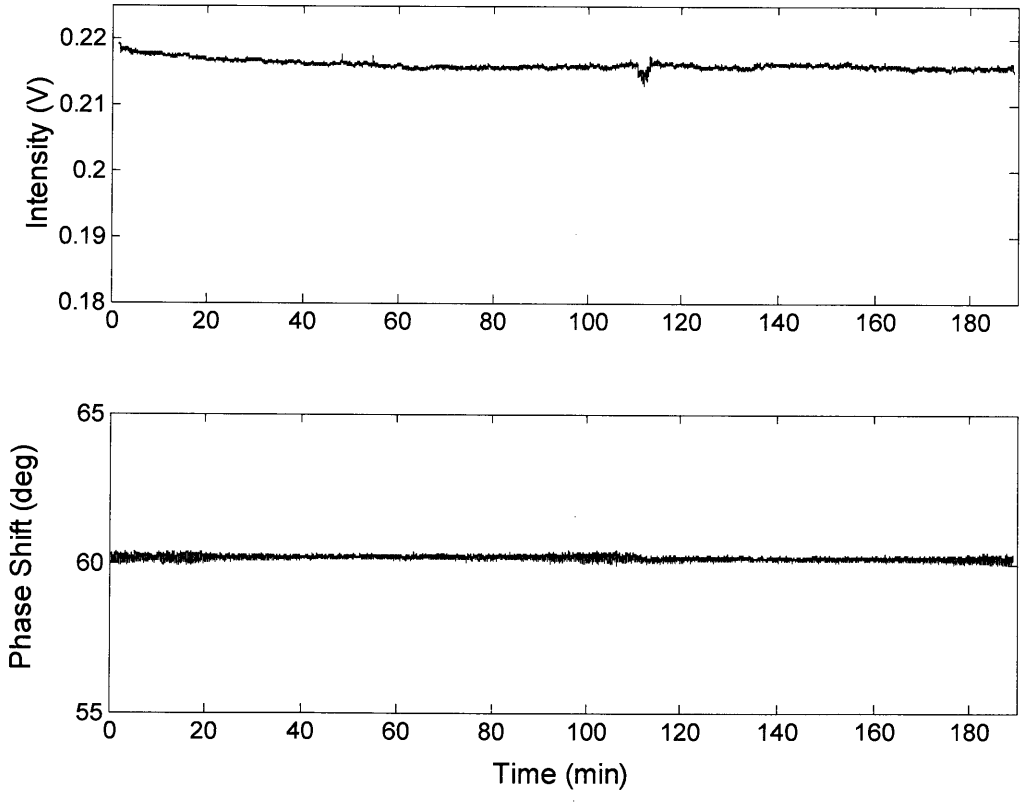

Figure 5.23: Three hr. photobleaching test showing deterioration (photobleaching) of the intensity based signal. The phase-based signal displays no deterioration through the course of the experiment

The change in observed voltage was 8 mV, corresponding to an error of 2.75% over the full-scale range of the sensor. As anticipated, the phase-based measurement of the luminescent lifetime was entirely unaffected by photobleaching effects, justifying the selection of phase-based lifetime as the preferred sensing technique. Based on the lower limit on response time in liquid, approximately 30 seconds, the sampling rate of the measurement apparatus could be reduced from 5 Hz to 0.2 Hz, sampling every 5 seconds, with a negligible loss in dynamic resolution. Reducing the sampling rate by a factor of 25 would deliver the same dose of illumination to the device as produced in our photobleaching test, over a period of approximately 72 hours rather than 3 hours. This places the operational lifetime of the sensor on the order of at least 3 days with a measurement error of essentially 0% in the lifetime-detection regime.

5.5 Modeling of mass transfer in the microfluidic oxygenator

The mass transfer properties of the microfluidic oxygenator were characterized analytically by developing a simple convective mass transfer model, in which the square channels of the actual device are modelled by infinite parallel plate channels. Experimental results obtained using the integrated PtOEPK sensor were compared to this model to determine the validity of the analytical work and demonstrate the model's appropriateness for simulations of future device designs. The parallel channel geometry of a single channel in the oxygenator is shown in fig. 5.24. Oxygen diffusion in the two-layer microchannel oxygenator occurs from the O_2 gas reservoir in the upper channel, through the PDMS membrane, and into the fluid channel. As shown in fig. 5.24, mass transfer begins at the point $x = 0$ and continues along the length of the channel to the end of the channel, where $x = L$.

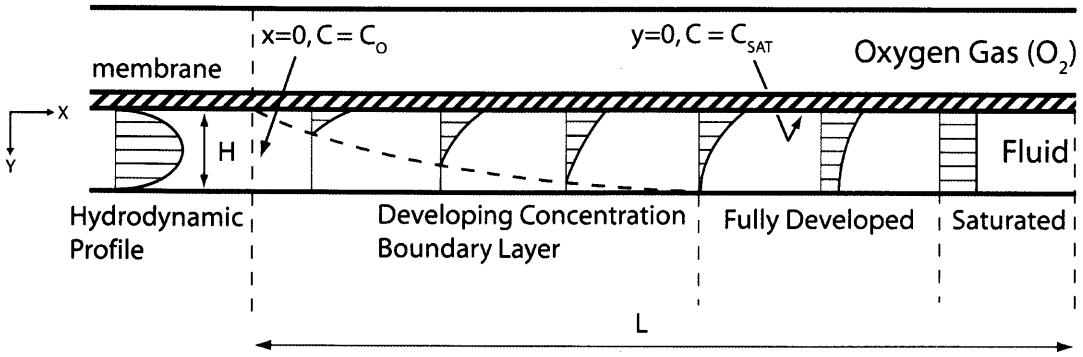

Figure 5.24: Geometry of the mass transfer scenario for the microfluidic oxygenator, detailing the parallel plate geometry, parabolic fluid velocity, O_2 reservoir, membrane, and the regimes of developing, fully developed, and saturated gas concentration profiles.

As noted, the actual fluid channels have a square cross section, for which the hydrodynamic entry length is on the order of 1.5 – 150 μm, depending on the flow rate, which is a variable in the experiment. Relative to the 1 cm overall length of the channel, the extremely short entry length justifies the assumption of a fully developed hydrodynamic profile in the model.

The ratio of the length of the developing region for the concentration boundary layer to the channel height is measured approximately by the Peclet number.

$$Pe = \frac{UH}{D_{o2}} \qquad \textit{(previously defined, 5.4)}$$

where U is the mean fluid velocity, D_{O2} is the diffusivity of oxygen in the fluid, and H is the channel height (see fig. 5.24). The Peclet number is a measure of the ratio of the convective to diffusive mass transport. The individual channel Peclet numbers are in the range of 50-5000, indicating that, except in the range of the lowest of the experimentally evaluated flow rates (Q=0.8μL/min, per channel), mass transfer occurs in the form of a developing concentration boundary layer. The developing concentration boundary layer, as well as the fully developed concentration profile, are shown in fig. 5.24. Recalling the nondimensional "effective channel length", L*, previously defined in eqn. 5.9, it can be

shown that the developing concentration boundary layer becomes fully developed at approximately $L^* \sim 1$. The definition of L^* is repeated here for clarity.

$$L^* = \frac{L}{H}\frac{1}{Pe} \qquad \textit{(previously defined, 5.9)}$$

This result will be important in the calculation of mass transfer coefficients in the different regimes of developing and developed flow.

Boundary and initial conditions for the diffusion problem are described as follows. The mass transfer coefficient between the O_2 reservoir and inner wall of the membrane is several orders of magnitude higher than the mass transfer coefficient for diffusion into the moving fluid. Because of the extremely high transfer coefficient across the membrane, the diffusive resistance of the membrane is effectively ignored, and the boundary condition at the inner membrane surface ($C_{y=0}$) is modeled as constant at the saturated concentration C_{SAT}, where C is the concentration of dissolved oxygen, measured in mg L^{-1}. The remaining, non-membrane contacting walls of the fluidic channel (the bottom channel wall in the model) are taken to be impermeable to oxygen. The normal concentration gradient at these walls is therefore zero. Fluid enters the oxygenation portion of the channel at the deoxygenated free-stream concentration of $C_{x=0} = C_O$.

The steady-state convective-diffusion equation for binary diffusion in dilute liquid solutions relates the concentration of the diffusing species (O_2) to the axial, x, and longitudinal, y, coordinates of the channel as follows:

$$u_x \frac{\partial C}{\partial x} - D_{o2}\frac{\partial^2 C}{\partial y^2} = 0 \qquad (5.16)$$

Here, u_x is the fluid velocity in the axial direction. Equation 5.16 states that the axial convection of a gaseous species is balanced by the transverse diffusion of the species.

The following equations are defined to facilitate a solution to eqn 5.16. At the inner surface of the membrane, the diffusive mass flux of oxygen is defined per unit time per unit area as follows:

$$j = D_{O2}\frac{\partial C}{\partial y} = h_D(C_{SAT} - C_M) \tag{5.17}$$

where h_D is the mean mass transfer coefficient. The value C_M is the "mixed mean", or bulk average, concentration, at any cross section. The mixed mean concentration C_M quantifies an 'average' oxygen concentration at an axial position in the channel and is defined by:

$$C_M(x) = \frac{\int C(x,y)\cdot u_x(y)dA}{\int u_x(y)dA} \tag{5.18}$$

Employing the definition of mixed-mean concentration C_M and wall flux j (eqn. 5.17), the diffusion equation (eqn. 5.16) can be integrated across the channel cross-section, assuming a constant mean mass transfer coefficient, yielding the following relation:[37]

$$\frac{(C_{SAT} - C_M(L))}{(C_{SAT} - C_O)} = \exp\left[\frac{-L}{H\cdot U}\cdot h_D\right] \tag{5.19}$$

Equation 5.19 describes the relation between the normalized mean oxygen concentration and the mean mass transfer coefficient, channel length L, and mean fluid velocity U.

Evaluation of eqn. 5.19 requires an appropriate mean mass transfer coefficient, h_D. The mass transfer coefficient is determined from the Sherwood number, Sh, a dimensionless parameter which measures the ratio of the mass transfer flux to the diffusive driving force.[37, 54, 55]

$$Sh = \frac{jH}{(C_{SAT} - C_M)D_{O2}} = \frac{h_D H}{D_{O2}} \tag{5.20}$$

Here, (C_{SAT} – C_M) characterizes the diffusive driving force; that is, the difference between the saturated concentration at the membrane wall of the channel and the mixed-mean concentration in the fluid. The Sherwood number can be computed for both the regions of developing and fully developed oxygen concentration in a variety of channel cross sections. For simplicity, the square channel geometry has been modeled as a hydrodynamically fully developed flow between infinite parallel plates, with an impermeable boundary condition on one wall and a constant concentration on the opposing wall.

The experimental flow rates under consideration vary across several orders of magnitude, meaning that the diffusive concentration profile may be either developing or fully-developed, depending on the value of L* (eqn. 5.9). In the developing boundary layer region, exact computations of the Sherwood number rely on a similarity solution of eqn. 5.16 that utilizes a linearization of the parabolic velocity profile near the membrane wall known as the *Leveque* approximation.[56] Such an approximation is only valid for boundary layers which are extremely thin relative to the channel width. Therefore, the analytical solution for the developing boundary layer concentration profile is exact only for values of L* considerably less than 1, for which the boundary layer thickness is thin. For values of L* on the order of 1 or greater, the concentration profile is fully developed and the Sherwood number is constant.[57] Based on these two solutions, a piecewise function for the Sherwood number can be defined that is valid over approximate ranges of L* given below:

$$Sh = 1.233 L^{*-1/3} \qquad L^* \ll 1 \qquad (5.21\text{ a})^{56}$$

$$Sh = 4.861 \qquad L^* \geq 1 \qquad (5.21\text{ b})^{57}$$

Equation 5.21 is plotted in fig. 5.25, where the solutions in both ranges of L* are extrapolated into the transition regime where an exact solution is not available.

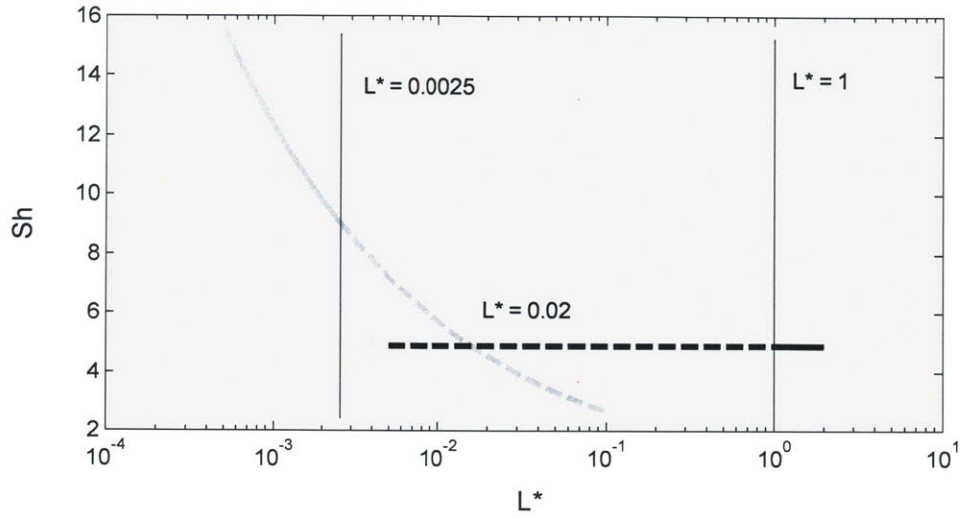

Figure 5.25: Sherwood number (Sh) plotted versus effective length (L). For the transition regime between 0.0025 < L* < 1, the concentration boundary layer Leveque solution (grey) and the fully developed solution (black) have been extrapolated beyond their formal range of applicability. The Leveque solution intersects the fully developed solution at L* ≈ 0.02. In the present analysis, Sh is approximated as a piecewise function defined by the Leveque solution below L* = 0.02 and the fully developed solution for L* > 0.02. This approximation was verified to produce minimal error.*

From fig. 5.25, the thin-boundary-layer Leveque solution intercepts the fully developed solution at approximately L* = 0.02. As a simple approximation the extrapolated solutions are taken to hold up to their intersection, that is,

$$Sh = 1.233 L^{*-1/3} \qquad L^* < 0.02 \qquad \text{(5.22 a)}$$

$$Sh = 4.861 \qquad L^* \geq 0.02 \qquad \text{(5.22 b)}$$

Applying the definition of the Sherwood number given in eqn. 5.22 to the solution of eqn. 5.19 and comparing to the results of analogous experimental heat transfer data given in Shah and London, it was verified that the approximate form of Sh in eqn. 5.22 yields a maximum error of less than 5% in determining the mean concentration.

Figure 5.26 shows the parallel plate model result given by eqns. 5.19 and 5.22, together with the experimental data obtained for the percentage oxygen concentration delivered by the oxygenator at a particular effective length, L^*. The data is plotted on a

semi-logarithmic scale with percent oxygenation defined relative to the calibration endpoints, where 0% represents nitrogen-bubbled water and 100% represents oxygen-bubbled water (0 – 42.5 mg L^{-1}). Note that, since fig. 5.26 displays *percent* oxygen concentration relative to the inlet concentration, the quantities derived from eqns. 5.19 and 5.22 for a single channel are equally valid for the entire 64 channel oxygenator network.

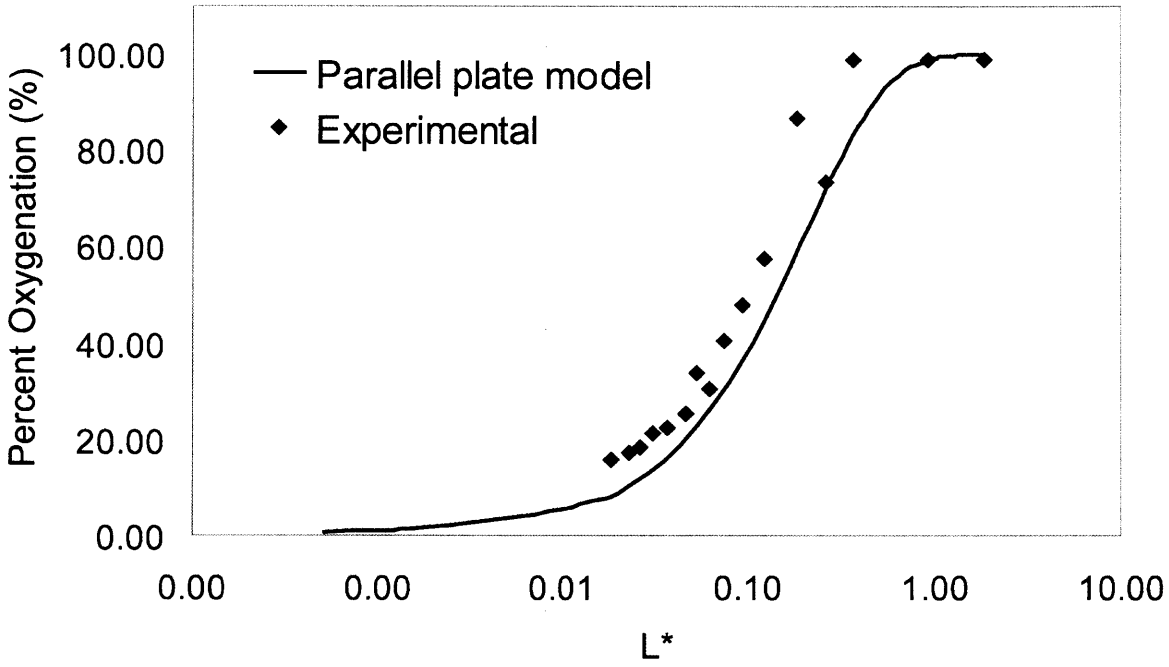

Figure 5.26: Experimental and analytical results for the mixed-mean O_2 concentration plotted versus L.*

Figure 5.26 confirms that the experimental data is extremely well matched by the simple convective mass transfer model of eqns. 5.19 and 5.22. It is acknowledged that the parallel plate model utilized for the mass transfer analysis is an approximation to the actual square geometry. We expect that the true mass transfer coefficient for a square channel will be slightly higher than the value presented in eqn. 5.22, due to corner effects in the aspect ratio one channel. However, the agreement between experiment and theory, demonstrated in fig. 5.26, seems sufficient to justify the approximations used in the simplified analytical model. In future iterations of microchannel and micro-oxygenator design, the good agreement between experiment and theory obtained here justifies the use

of the simple convective-diffusion model to predict device characteristics and optimize device geometry. For a given device in a particular application, the parameter L* may be altered in real-time via the flow rate to deliver a precise and repeatable concentration of oxygen between 0-100% saturation in water, on-demand.

Chapter 6

Hemocompatibility

6.1 Preliminary results on microchannel hemocompatibility

Preliminary experiments to test the hemocompatibility of the microfluidic network fabricated for the photolytic oxygenator were conducted by Trevor Snyder, graduate researcher at the McGowan Institute for Regenerative Medicine at the University of Pittsburgh. Hemocompatibility was assessed by measuring plasma free hemoglobin release and thrombus formation with blood flow. Hemolysis studies were conducted with bovine blood anticoagulated 1:9 with acid citrate dextrose. The construct was connected with two 23 gauge needles to a circuit consisting of a 30 cm extension tubing set and a roller pump (Fisher) with a 3 inch section of ¼" diameter silicon tubing. The circuit was primed with saline, and then a blood reservoir was connected to the inlet of the roller pump. A sample of blood was then collected to measure baseline hematocrit and plasma free hemoglobin. The blood reservoir was then removed from the circuit and the blood circulated for 5 hours, whereupon a final sample was collected. A parallel circuit was set-up without the microfluidic construct. Plasma free hemoglobin increased 37.0 mg/dL after 5 hours of flow at 0.4 mL/min.

For thrombus testing, bovine blood anticoagulated with 2 U/mL heparin was used, with mepacrin added to label platelets and leukocytes. A microfluidic construct was mounted onto a microscope slide and placed on an inverted epiflourescent microscope (Zeiss). Blood was drawn through the capillary network at 0.1, 0.4, and 0.64 mL/min for 20 minutes. Images of the branching networks and channel lumens were collected immediately after initiating blood flow and then every 2 minutes. All channel lumens remained patent, although thrombus was observed in about 25% of the channel

inlets/outlets, and at bifurcations (fig. 6.1). Based on experimental results, this pattern can be attributed to flow conditions that occur at 90° bifurcations, which include flow separation and recirculation regions. The occurrence of blood coagulation was not a surprising result given the non-optimal device branching angle, as previously discussed. Current and future investigations of device geometry will use computational fluid dynamics (CFD) software to optimize the fluid dynamics in the bifurcation region.

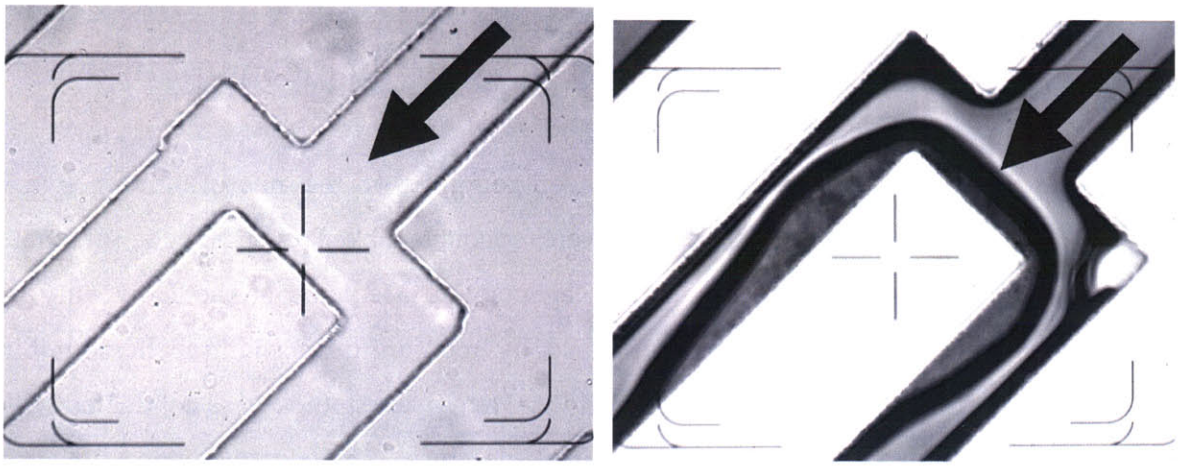

Figure 6.1: Image of microchannel bifurcation before and after exposure to flowing blood. The image on the left (A) shows a channel bifurcation prior to blood contact. The image on the right (B) shows the same channel bifurcation after 20 minutes of blood flow (the flow rate was 20 μL/min in the inlet channel). The dark areas in the channel are thrombi and areas of reduced flow. The arrows indicate the direction of flow. The pattern of thrombus occurred in areas of flow separation and recirculation.

The blood flow experiments originally conducted at the University of Pittsburgh were repeated with corporate collaborator Levitronix LLC, in Waltham MA. Anticoagulated blood was prepared in a similar manner to the experimental conditions in the Pittsburgh experiments. Hemolysis tests were performed at flow rates between 0.05 – 5 mL/min through the device to determine the influence of flow rate on shear-induced hemolysis. Unlike the Pittsburg test, in which blood was re-circulated continuously through the device using a roller pump, tests were performed at Levitronix by flowing blood in single pass through the device from a syringe pump to a collection reservoir. Surprisingly, almost no RBC hemolysis was observed at any of the experimental flow rates. We

conclude that the hemolysis effect is much less significant than expected, and manifests only after prolonged recirculation.

Clotting, however, proved to be a significant obstacle in blood perfusion tests performed at Levitronix. Initial images (fig. 6.2) revealed no blood coagulation in the microchannels. However, clotting was rapidly initiated and occluded the device within 45 min. of beginning blood perfusion (fig. 6.3).

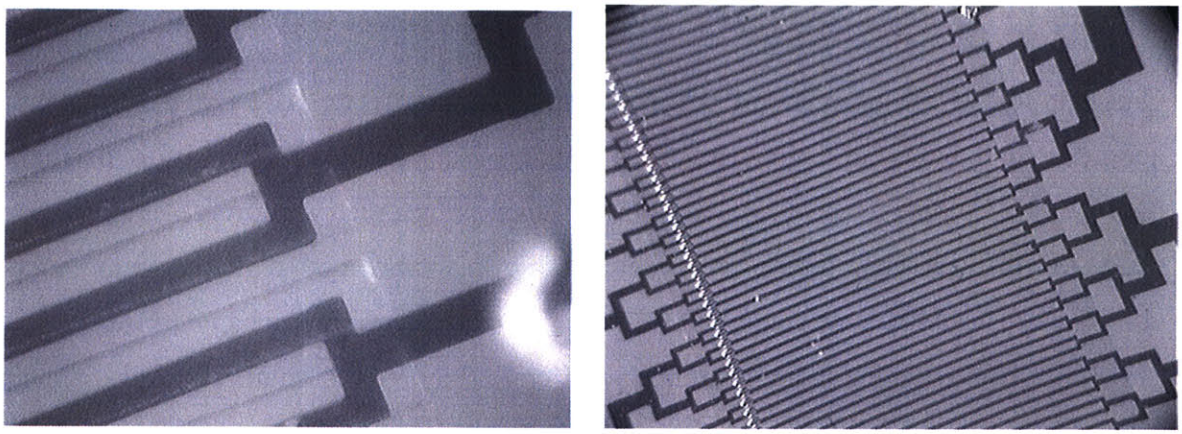

Figure 6.2: Microchannel images following 5 min. blood perfusion, demonstrating no coagulation in conditions of adverse fluid dynamics.

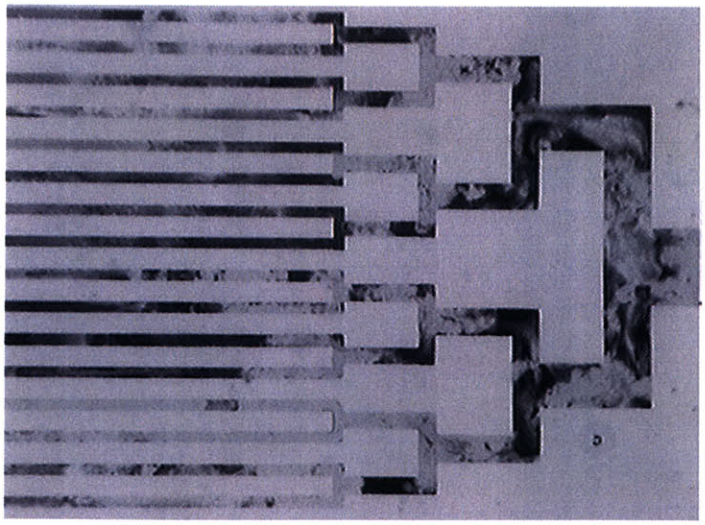

Figure 6.3: Microchannel image following 45 min. of blood perfusion. Occlusion of the majority of the channel lumen generated prohibitively high back pressure, forcing termination of the test.

The absence of fluid circulation patterns in fig. 6.3, unlike fig. 6.1, suggests that clotting in the Levitronix test may have been more influenced by adverse material interactions, ie. between the blood and glass substrate, than by the non-optimal branching geometry and fluid dynamics. Both the geometry and biomaterial surface interaction play a key role in the efficacy of blood perfusion in PDMS microdevices.[58]

6.2 Future device designs for optimal blood flow

One solution to the problem of adverse fluid circulation is to redesign the branching geometry to have a smoother, more optimal profile. An alternative is to design a microfluidic device which eliminates the bifurcation geometry entirely. Figure 6.4a shows a "diffuser chamber" – type device that was fabricated with the intention of eliminating shear stress or coagulation issues associated with microchannel bifurcations. The width of the device is approximately 2.5 cm. Hundreds of small 100 μm diameter pegs are interspersed throughout the chamber to prevent sagging of the device in the center of the chamber.

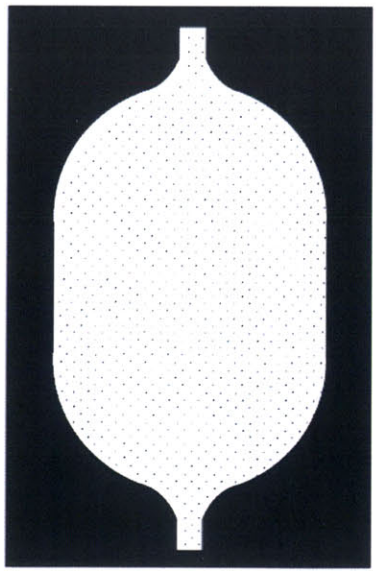

a)

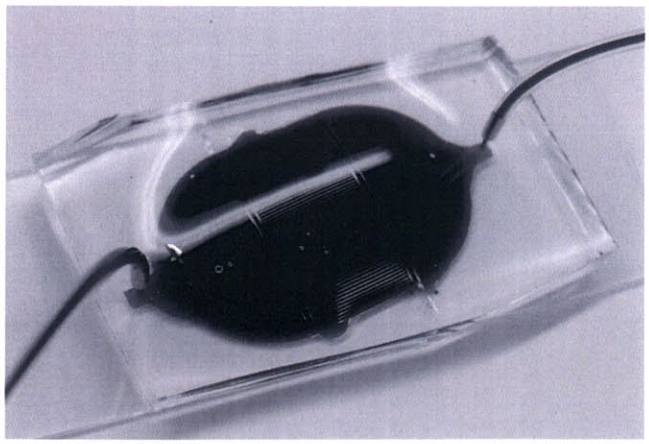

b)

Figure 6.4: a) Microfluidic chamber design. b) Chamber-type device under blood flow, demonstrating considerable high-pressure bulging.

Experimental results with this device illustrated that, while sagging of the chamber is not a significant concern, swelling of the chamber and build-up of fluid pressure, akin to the charging of an electrical capacitor, is a significant problem. The bulging is shown in fig. 6.4b. Chamber bulging generates such a significant pressure rise that one device actually burst explosively off the glass slide during testing.

Figure 6.5 represents the most recent iteration of fluid network design, intended to be a compromise between the extremely small channel widths and sharp bifurcations of the device shown in figs. 6.1-6.3, and the excessively large chamber design in fig. 6.4. The "mesh" of larger width channels in fig. 6.5 is intended to eliminate the risk of excessive shear stress and channel occlusion, while the square pegs interspersed throughout the interwoven channels are intended to provide sufficient covalent adhesion to the glass/TiO_2 substrate to prevent bursting of the microfluidic device. The wide entry and exit areas of the device provide ample room for the incorporation of optical oxygen sensing elements.

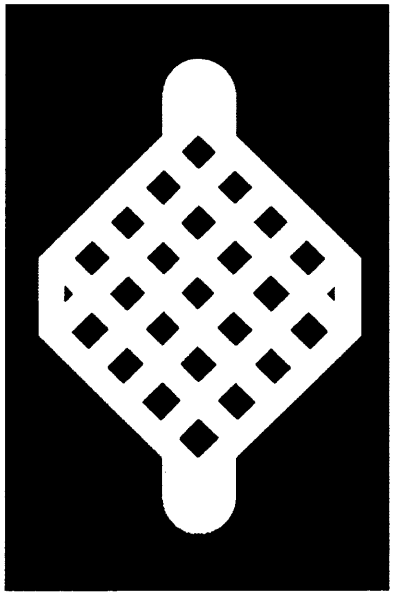

Figure 6.5: "Mesh" style interwoven fluidic network design

Future designs of microfluidic networks are likely to proceed in the direction of fig. 6.5, maintaining low channel height for efficient oxygen diffusion, while improving the

circulation dynamics and device performance by incorporating broader, interconnected flow channels.

Chapter 7

Summary and Conclusions

The work described in this thesis advances the goal of designing an integrated photolytic artificial oxygenation platform. We have effectively pursued the development of a photolytic microfluidic oxygenator via a decoupled, parallel design process. At the same time as corporate research collaborators independently pursued increased quantum efficiency and improved mechanical stability in the development of the TiO_2 photolytic film, we characterized and attempted to optimize the fluidic and mass transfer properties of the microfluidic element that is intended to be bonded with the photolytic surface. By pursuing this development in parallel, the complexity of the photolytic element was removed from the experimental process of refining the microfluidic device. Ultimately, we envision that photolytic and microfluidic elements could mate as seamlessly as if the TiO_2 photolytic device were simply one of the glass cover slips currently used as a substrate for the microfluidic channels.

This thesis details the development of a unique integrated microfluidic platform for the precise delivery and detection of oxygen into a fluid medium. Multilayer 2D soft lithography was utilized to create a PDMS micro-capillary network with a minimum dimension approximately ten times the size of a human red blood cell. The patterning of bifurcations in the microfluidic capillary system was designed in emulation of biological precedents based on morphological data from an adult human pulmonary capillary tree. It was shown that Murray's law, a simple mathematical model identifying an optimum branching condition, is in good agreement with morphological data for capillary networkds, and an approximation to Murray's law was developed for the rectangular geometry of the microfluidic device. While it was not possible to conduct extensive testing of blood flow in PDMS microchannels, it was demonstrated that RBC hemolysis

is potentially a less significant problem than originally anticipated. Blood coagulation may likely prove to be a greater challenge for future microchannel designs.

An essential feature of the two layer microfluidic device described above is the parallel channel oxygen exchange portion, an element that allows the passage of a diffusive flux of oxygen gas from one set of channels, across a thin PDMS membrane, into neighboring channels containing a fluid such as water or blood. This oxygen diffusion technique, which we have referred to as "passive oxygenation" was developed to characterize the device's mass transfer characteristics in lieu of an oxygen-generating photolytic film. A simple model was derived to estimate the quantity of O_2 that would be diffused through the oxygenator into a fluid medium, given a particular channel geometry and fluid flow rate. This model was intended to be used to allow rapid estimation of the performance characteristics of future generations of multilayer channel designs.

To evaluate the oxygen transfer efficiency of the microfluidic oxygenator, and thereby validate the accuracy of the aforementioned mass transfer model, an integrated optical oxygen sensor was designed and fabricated to detect dissolved oxygen levels in the microfluidic device. The optical sensor is unique for its integration directly into the microchannels of the device, its ability to achieve non-invasive, real-time oxygen monitoring, and its robustness and accuracy across several orders of magnitudes of fluid flow rate. The sensing characteristics of the sensor were evaluated in gaseous and aqueous samples, verifying the linearity, optical stability, resolution, and accuracy of the sensor. In particular, the oxygen sensor achieved a maximum resolution of 120 ppb, repeatability across two orders of magnitude of micro-flow rates, and excellent long-term stability in the phase-sensing regime. The oxygenating performance of the entire integrated chip was measured as a function of fluid flow rate, channel height, and channel length, on the basis of the dimensional analysis employed in the model via the dimensionless parameter L*. The percent oxygenation achieved by the microfluidic oxygenator was shown to be accurately predicted by the simple convective mass transfer model previously developed. The optical oxygen sensing device demonstrated favorable sensing performance compared to recently published optical sensors of a similar nature,[41, 44, 45] with a simpler fabrication protocol and a more flexible platform for detection of gaseous or dissolved oxygen. Based on the good agreement between experimental data

on oxygenator performance and analytical predictions of the convection-diffusion mass transfer model, we conclude that the model is indeed an effective tool for the rapid estimation of appropriate channel dimensions and flow conditions in the design of oxygenation elements for future microfluidic devices.

Future areas of investigation into the design of a microfluidic oxygenator must certainly involve the iterative redesign and improvement of the capillary network geometry. Preliminary hemocompatibility tests clearly demonstrated that the 90 degree bifurcation geometry is undesirable for blood flow. It will remain for future research to determine whether a more optimal bifurcation shape is preferable, or whether better results may be obtained by eliminating channel bifurcations entirely in favor of a nozzle-type "chamber" device or some other previously untried geometry. The low incidence of hemolysis in tests conducted thus far suggests that shear stress may be a less critical determinant of hemocompatibility than previously imagined. Minimization of adverse fluid conditions and optimization of the biomaterial interaction between blood cells, proteins, and the microfluidic device should be a primary focus. More suitable biomaterials, hydrophilic surface treatments such as poly-ethylene-glycol (PEG), and endothelial cell culturing on channel walls have all been investigated in the study of biological fluid flow in microfluidics[53, 59] and merit consideration.

An important validation of the effectiveness of the optical oxygen sensor will be the demonstration of proper sensor function for the detection of oxygen levels in whole blood. To date, only preliminary tests have been made on the performance of the sensor with blood samples, as opposed to the water samples which were used for the majority of experimental work. There are a number of important distinctions between oxygen detection in water and oxygen detection in blood that make the latter a considerably more challenging problem. Blood, unlike water, is not optically transparent, which means that the intensity of light passing through the fluid to the PtOPEK-ps film will be greatly attenuated. Additionally, the presence of cells and macromolecules in the bloodstream may scatter and refract the incident light. The concentration of oxygen in blood, due to the presence of oxygen-binding hemoglobin, is more complex to determine than for water, where the concentration of oxygen molecules dissolved in the fluid is simply

proportional to the partial pressure of the gas and the solubility of O_2. It is likely that sensing may be further complicated by the issue of blood clotting and coagulation over the polystyrene sensor film, diminishing and potentially eliminating the sensor signal. Other problems related to sensing in the bloodstream may arise, and it will be important to evaluate the sensor, and if necessary improve its operation, to address these complexities.

A final direction in which to consider future research pertains to the third specific research motivation identified in the Introduction. The microfluidic oxygenation platform developed and presented in this thesis accomplishes rapid and efficient diffusive exchange of oxygen at small length scales, in unison with precise sensing of oxygen concentration. In this function, the microfluidic device effectively mimics the action of the pulmonary alveoli system, making it ideally suited to the artificial photolytic lung application for which it was designed. In a broader context, however, additional applications of the integrated microfluidic oxygen delivery and detection system should be pursued in the burgeoning fields of Lab-On-A-Chip and Micro Total Analysis (μ-TAS) systems, where foreseeable applications include tissue engineering and cell culturing in a microfluidic environment, real-time blood gas detection in a clinical environment, or extracorporeal oxygenation in a surgical setting. [16, 53] In addition to the initial aim of developing an artificial respiratory element, the versatility of the microfluidic oxygen delivery and detection technology presented in this thesis promises to yield a myriad of applications in the expanding fields of MEMS and biological microdevices.

Appendix A

Microfluidic fabrication

A.1 Fabrication of Su-8 soft lithography mold

The cross-sectional channel dimensions in the oxygen-exchange portion of the microfluidic device are 100 μm x 100 μm. The mold for the soft-lithographic stamping process was fabricated at MIT's Experimental Materials Laboratory (EML) from SU-8 negative photoresist (SU-8 50, Microchem) on a 3" Si wafer (Silicon Quest). Microchem's SU-8 50 resist was determined to have superior adhesive properties than it's successor, Microchem SU-8 2050, resulting in considerably longer mold lifetime.

Silicon wafers were prepared with a three step solvent cleaning process of acetone followed by methanol, isopropanol, then DI water. Cleaned wafers were baked at 130°C for 30 min. to eliminate residual organic solvents. The SU-8 resist was spun onto clean wafers in a two-step ramp, first at 500 rpm for 10 sec., followed by 1000 rpm for 30 sec. to yield a 100 μm coating. A two step hotplate pre-exposure bake was performed, consisting of 5 min. at 65°C followed by 15 min. at 95°C. Following the 15 min. 95°C bake, wafers were transferred back to the 65°C hotplate, which was then turned off and allow to cool to room temperature. This cool down ramp is essential to minimize the build-up of thermal stresses in the thick resist layer.

Photolithography was performed using a high resolution transparency mask, printed at 3550 dpi (Mikacolor, CA). A high-frequency optical filter was used to prevent over-absorption of low frequency (< 350 nm) light by the SU-8. Exposure was performed, on average, for 2.5 min. Exposure times were determined by calibration of the broadband lithography machine's optical output using a radiometer probe. The desired exposure dose was approximately 500 mJ cm^{-2}.

A two-step postexposure hotplate bake was performed for 2 min. at 65°C, and 10 min. at 95°C. Wafers were cooled by transferring to the 65°C hotplate and shutting off the power as previously described. Once cooled, wafers were developed in a propylene glycol monomethylether acetate (PGMEA) solvent for approximately 5 min., washed in isopropanol and water, and dried. No post-development bake was performed.

Following development of the SU-8 photoresist, a 2 hour evaporation process was performed using a high molecular weight trichloro-perfluorooctyl silane (Aldrich) at room temperature.

A.2 PDMS soft lithography fabrication

PDMS was chosen for the microfluidic structure based on its low cost, non-toxicity, and ease of fabrication with soft-lithography rapid prototyping techniques. PDMS is particularly appropriate for the oxygenator application because of its high permeability to oxygen gas. The diffusivity of oxygen in PDMS is approximately $6x10^{-9}$ m^2 s^{-1}.[60] General Electric RTV615A/B two-part PDMS was used for this work. To construct the 2-layer microfluidic device, a 15:1 monomer/hardener mixture was mixed and degassed, then applied via spin-coating (1000 rpm, 30 sec.) to a thickness of 120 μm onto an SU-8 mold. Simultaneously, a 5:1 PDMS mixture was prepared and poured to a thickness of 6 mm onto a second SU-8 mold. Prior to baking, both the PDMS spin-coated and poured molds were degassed under vacuum in a bell jar to remove air bubbles. The molds were then baked in an oven for 20 minutes at 80°C. Following the initial bake, both molds were removed from the oven for alignment. The thick (6 mm) PDMS layer was cut and peeled from the SU-8 mold and punched with fluidic vias using a blunt-tipped 20G surgical steel Luer stub (BD). The thick PDMS layer was visually aligned and mated to the spin-coated lower layer (still affixed to the wafer) under an Olympus SZX9 stereo-zoom dissecting microscope. The two affixed PDMS layers were firmly bonded by a second, 2-4 hour bake at 80°C. After this final bake the chip was cut from the wafer, peeled off, and the lower-layer was punched with fluidic inlets. Examination of device cross-sections under a microscope confirmed the accuracy of channel dimensions and

vertical alignment between gas and fluid channels. Thickness of the inter-layer membrane can be precisely controlled by variation of the spin coating speed during fabrication of the lower PDMS layer. For effective oxygen transfer and consistency of fabrication, 20 μm is an optimal membrane thickness.

Fully baked 2-layer PDMS devices are bonded via an O_2 plasma oxidation process to form a irreversible bond with a glass substrate. Additionally, oxygen plasma bonding renders the inner surface of the microchannels hydrophilic.

(This page intentionally left blank)

Appendix B

Electronic circuit design for optical oxygen sensor

Two analog circuit boards were designed to operate the optical oxygen sensor. The first of these boards was a "modulator" (fig. B.1) which generated a variable frequency square wave voltage signal to power the LED. The second board was the signal conversion and amplification board (fig. B.2), consisting primarily of various amplifiers (transimpedance and non-inverting).

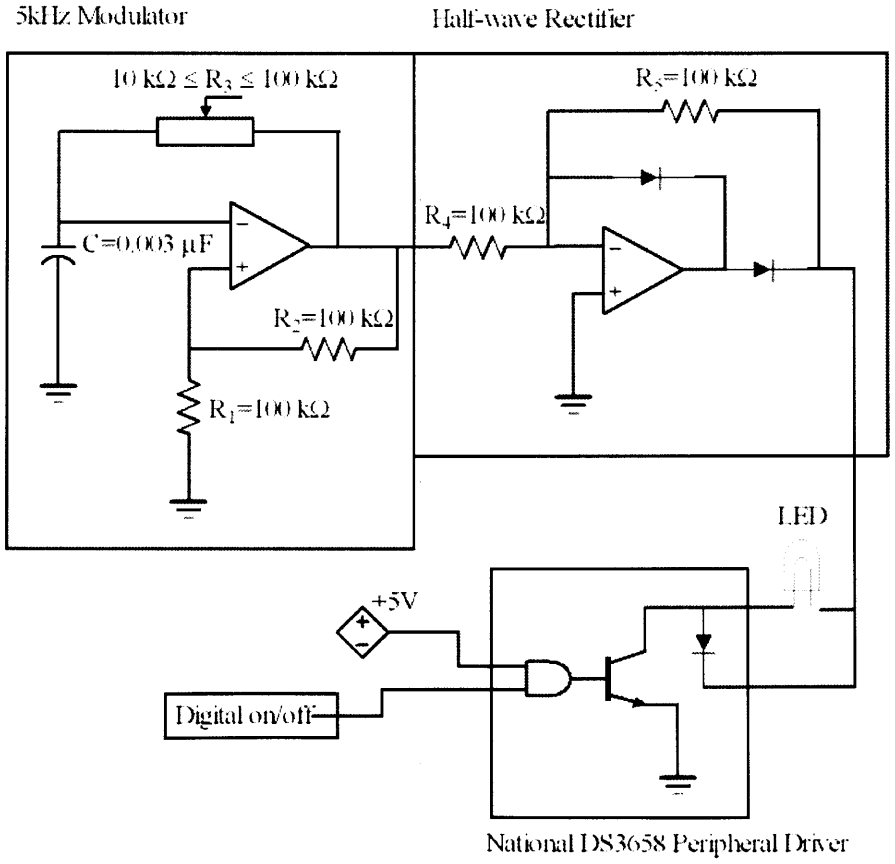

Figure B.1: "Excitation circuit": diagram for high frequency LED modulator

Circuit elements are listed in the following section as appropriate – all operational amplifiers (op amps) were Fairchild Semiconductor LF347 type, a high speed, high input impedance, wide bandwidth JFET quad op-amp. The LF347 operates at +/- 15 V. FET op amps have a low input current which makes them a nearly universal choice for photodetector monitoring.[61] Figure B.1 illustrates what was essentially the "excitation" circuit for the optical oxygen sensor, responsible for driving the excitation LED. The '5kHz Modulator', fig. B.1, is an analog circuit that generates a square wave at a frequency specified as follows[62, 63]:

$$v = T^{-1}, \quad T = 2R_3 C \ln\left[\frac{1+\lambda}{1-\lambda}\right], \quad \lambda = \frac{R_1}{R_1 + R_2} \tag{B.1}$$

The resistor 'R_3' is a potentiometer, which allows for variation of the modulation frequency between 15 kHz and 1.5 kHz. The 'Half-wave rectifier' is a unity gain circuit which crops the negative component of the square wave signal at zero[64]. The effect of the rectifier upon the square wave signal is shown in fig. B.2. The amplitude of the square wave driving the LED is approximately 4-5V. The maximum reverse voltage rating on the LED (590 nm, 2500 mcd, Ledtronic) is 5V, indicating that the negative component of the square wave signal could potentially exceed the LED threshold and damage the bulb. Several bulbs were indeed destroyed this way, resulting in the need for the rectifying circuit to eliminate the reverse voltage upon the LED.

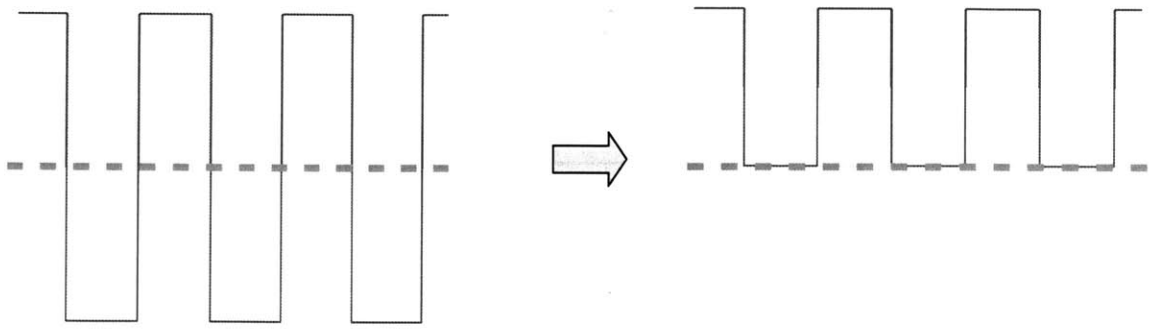

Figure B.2: Square wave and rectified wave

The final element of the "Modulator" circuit is a National Semiconductor DS3658 Peripheral Driver chip, which allows for a digital input control of the LED via an integrated transistor. Using the digital input, the modulator circuit may be externally activated from Labview/DAQ, at which point the LED will pulse at the frequency set by the modulator. Upon de-activation of the analog input, the DS3658 enters a high impedance state and the LED is shut off.

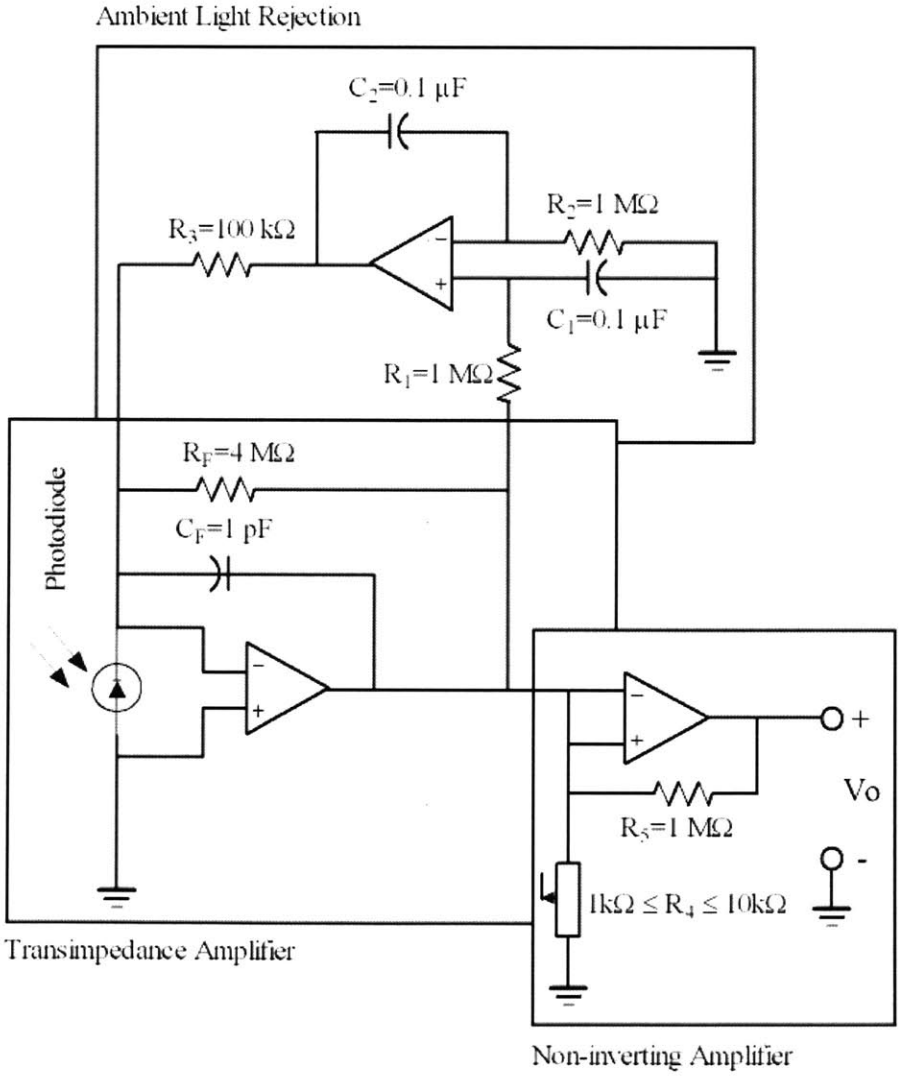

Figure B.3: "Detection circuit": Transimpedance amplifier and associated circuits

Figure B.3 illustrates the "detection" circuit for the optical sensor, which consists of a transimpedance amplifier, low-pass rejection circuit, and non-inverting amplifier. The transimpedance amplifier, which may also be described as a "current to voltage converter", converts the output of the Si photodiode (S2386-44k, Hamamatsu), which is in the form of a current, to a voltage, by forcing the current through the feedback resistor R_F. Thus, the output of the amplifier may be given by:

$$V_O = I_P * R_F \tag{B.2}$$

where I_P is the photodiode current. The majority of the design on the transimpedance amplifier for this application was based upon an article at www.elecdesign.com (electronic design) by Bob Pease (National Semiconductor),[65] which compliments the work of Jerald Graeme, *Photodiode Amplifiers – Op Amp Solutions*.[66] A transimpedance amplifier allows amplification of extremely small current signals to detectable voltages, providing that R_F is sufficiently large. While it is possible to implement a transimpedance amplifier simply by placing a resistor in series with the photodiode and not including the op amp, the op amp-based transimpedance amplifier allows for much higher signal to noise ratios and provides a considerably lower time constant. A potential downside of the op amp implementation of the transimpedance amplifier is overshoot and oscillation associated with the input capacitance of the op amp. To stabilize the system, a capacitor C_F is added in parallel with the feedback resistor R_F. A large capacitance value for C_F will result in a stable circuit with low noise gain, but a very slow time constant. A much faster time constant can be attained while maintaining the stability and low noise gain of the circuit by choosing C_F according to the following criterion[65]:

1)

$$\text{If} \quad \left(\frac{R_F}{R_{IN}}+1\right) \geq 2\sqrt{GBW * R_F * C_S} \tag{B.3a}$$

$$\text{then} \quad C_F = \frac{C_S}{2\left(\frac{R_F}{R_{IN}}+1\right)} \tag{B.3b}$$

2)

$$\text{If} \quad \left(\frac{R_F}{R_{IN}}+1\right) < 2\sqrt{GBW * R_F * C_S} \tag{B.4a}$$

$$\text{then } C_F = \sqrt{\frac{C_S}{GBW * R_F}} \tag{B.4b}$$

where R_F is the previously defined feedback resistance, C_S is the source capacitance of the photodiode, R_{IN} is the input resistance of the op amp, C_F is the desired value of the feedback capacitor, and GBW is the gain-bandwidth product. The gain, G, is the open loop op amp gain, and the bandwidth is the desired operational bandwidth of the amplifier. Since the photodiode is intended to be receiving signals at approximately 5kHz, the bandwidth is chosen to be slightly more than twice the operational frequency to prevent excess high frequency noise, but avoid attenuation of the signal. The values for the transimpedance amplifier components are given below.

R_{IN} = 1E12 Ω

R_F = 4E6 Ω

G = 1E5

BW = 12 kHz

C_S = 1600 pF

Based on these values, the second scenario given above (B.4) applies, which yields that the feedback capacitance should be approximately:

$C_F = 1$ pF

The second stage of fig. B.3 is the ambient light rejection circuit, which is a DC restoration circuit to electronically reject low-frequency light signals from ambient sources.[67] This permits repeatable operation of the sensor in environments of variable ambient light with a minimum of optical shielding. The low frequency cutoff pole of the circuit was chosen to be 16 Hz, given by the following equation:

$$f_{-3dB} = \frac{1\,M\Omega}{R_3(2*\pi*R_2*C_2)} \tag{B.5}$$

The decision to use high frequency modulated excitation light for the optical sensor was motivated both by the desire to implement phase-based sensing, and by the choice to incorporate the ambient light rejection circuit, which eliminates any DC or low-frequency contribution from the LED/photodiode.

The final stage of the detection circuit, fig. B.3, is the non-inverting amplifier, which amplifies the milli-volt range signal of the transimpedance amplifier to ~1V. The non-inverting amplifier gain is given by:

$$\frac{V_o}{V_i} = \left(1 + \frac{R_5}{R_4}\right) \tag{B.6}$$

Both the pre-amplifier and post-amplifier are extracted from the circuit board to be read into the DAQ card.

Shielding

A minimum of electrical shielding was required to achieve a sufficiently high signal to noise ratio. All wiring running from the circuit board to external components (ie LED, photodiode, DAQ board) is insulated, ground, shielded cable. It is particularly important to minimize the length of wire from the photodiode to the detector circuit board, as stray current signals in this portion can be magnified to an extreme degree because of the transimpedance amplifier's high sensitivity. Both the excitation and detection circuit boards are shielded in grounded aluminum enclosures. A degree of common mode (60 Hz) noise was observed in the detector signal, but it was not significant enough to be deleterious to the signal quality.

(This page intentionally left blank)

Appendix C

Optical sensor data aquisition and Labview module

Data acquisition and processing for the optical sensor was performed in Labview. This section details the development of the Labview VI used to operate the sensor. The methodology of the data acquisition and processing scheme is summarized in the following steps:

1) Both the reference (excitation) signal driving the LED and the detected signal from the photodiode are read from the USB DAQ board. The LED modulation frequency is tunable, but was experimentally determined to be optimal near 5 kHz. In order to recover all the Fourier components of the reference and detected waveforms to effectively determine the intensity and phase shift of the detected signal, it was necessary to sample at or above the Nyquist frequency.[68] The Nyquist frequency is defined as follows:

$$f_{Ny} = \frac{1}{2}\upsilon \qquad \text{C.1}$$

where υ is the sampling frequency. The Nyquist frequency, or Nyquist limit, dictates that the highest frequency that can be detected by sampling a continuous signal is half the sampling rate. In this case, the Nyquist limit dictates that, to detect a 5kHz signal, the DAQ board must sample at 10 kHz or above. Signals above 5 kHz are low-pass filtered in the analog electronic loop, previously described, to avoid the phenomenon of aliasing. Aliasing describes the presence of unwanted signal frequencies overlapping due to a sampling frequency that is below the Nyquist limit. Each channel of the DAQ

board is sampled at 20 kHz, twice the necessary frequency, to improve the quality of the reconstructed digital signal.

2) To minimize the total light exposure to the sensor and diminish the effect of photobleaching, as well as to allow for computational time required for signal processing, the Labview module operates by alternately sampling the DAQ at 20 kHz / channel for a period of time t_S and then pausing for a period of time, t_P. During the period t_S, the LED is pulsed at 5 kHz. During the period t_P, the LED is off. A single period t_S followed by a single period t_P corresponds to one full sampling cycle. For the bulk of experimentation, t_S and t_P were each set to 0.1 sec, yielding a full sampling cycle of 0.2 sec. Accordingly, in a single sampling cycle, Labview collects approximately 2000 datapoints. The actual number of datapoints is limited by the packetsize of the Measurement Computing DAQ board. The packetsize, which is 31, is the number of datapoints the board reads simultaneously. Therefore, the number of points must be an integer multiple of 31. Two thousand divided by 31 is 64.5, meaning that 64*31 = 1984 is the number of raw datapoints collected every sampling cycle. These points are averaged, as described in the following section, to yield a single value every sampling cycle. At a rate of 0.2 sec. per cycle, the board produces averaged data points at a rate of 5 Hz.

3) Signal processing in the Labview module provides additional filtering and determination of the average phase shift and intensity, once per sampling cycle.

Intensity: The 5 kHz waveform from the photodiode typically has some DC offset from 0 V, which is eliminated using a low-pass filter VI to determine the DC component of the waveform, and subtracting this from the raw signal (This is roughly equivalent to a high-pass filter). The amplitude is not measured directly, but rather the RMS magnitude of the waveform is determined using a Labview VI. The RMS amplitude varies in proportion to the total amplitude of the signal, and represents a cleaner, averaged value.

Phase Shift: The phase shift is determined by digital lock-in detection in the Labview module. Prior to lock-in detection, both the reference and detected signal are bandpass filtered in identical first-order digital butterworth bandpass filters. The concept of lock in detection is as follows:[69, 70] Two sinusoidal signals with a common frequency ω and an unknown phase shift δ may be represented as follows:

$$ref = A_R \sin(\omega t) = A_R \sin(r) \qquad \text{C.2}$$

$$signal = A_S \sin(\omega t + \delta) = A_S \sin(s) \qquad \text{C.3}$$

The sum and difference formulas for trigonometric identities yield the following two relations:

$$A_R \sin(r) A_S \sin(s) = \frac{1}{2} A_R A_S (\cos(s - r) - \cos(s + r)) \qquad \text{C.4}$$

$$A_R \cos(r) A_S \sin(s) = \frac{1}{2} A_R A_S (\sin(s - r) + \sin(s + r)) \qquad \text{C.5}$$

The reference signal may be converted to a co sinusoidal waveform by phase-shifting it 90° through a Hilbert Transform[71], implemented in Labview. The values 's – r' and 's + r' in the right hand side of the trigonometric identities, above, are shown below.

$$s - r = \omega t + \delta - \omega t = \delta \qquad (DC) \qquad \text{C.6}$$

$$s + r = \omega t + \delta + \omega t = 2\omega t + \delta \qquad (AC) \qquad \text{C.7}$$

The later of these two equations, C.7, retains a sinusoidal time dependence, while the former (C.6) is a constant. Hilbert filtering the reference signal to obtain a cosine and multiplying the waveforms as shown above in eqn. C.4 and C.5 yields two higher frequency sinusoidal functions with a DC offset.

Both functions are lowpass filtered to eliminate the AC component and retain the constant signal, $0.5A_RA_S\cos(\delta)$ and $0.5A_RA_S\sin(\delta)$, respectively. The ratio of these two constant signals eliminates the amplitude terms, yielding:

$$\frac{\frac{1}{2}A_R A_S \sin(\delta)}{\frac{1}{2}A_R A_S \cos(\delta)} = \tan(\delta) \qquad \text{C.8}$$

The arctan of the value in eqn. C.8 recovers the phase shift δ between the original reference and detected signals in C.2 and C.3. A schematic of the (simplified) Labview module used to implement the digital lock-in detection is shown in fig. C.1.

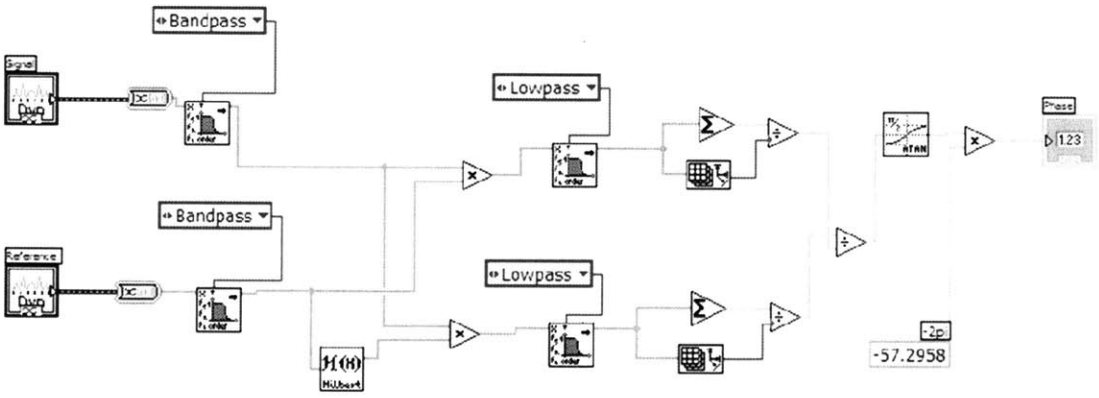

Figure C.1: Simplified Labview module for digital lock-in detection

4) The averaged values of intensity I and phase shift δ are added to a buffer of data points which is updated every full sampling cycle (0.2 sec). At the conclusion of a test, these buffers, along with filtered (10 point moving-average) buffers of the intensity and phase data, are saved to a user-defined Labview (.lvm) file. The time stamps of each averaged data point are saved in a buffer as well.

Figure C.2 shows the Labview VI front end. In the upper right hand corner, horizontally across the screen, are plots showing the filtered and unfiltered phase shift and intensity. The raw data, high-pass filtered raw data, and power spectrum of the raw (20 kHz) data are plotted along the bottom of the VI.

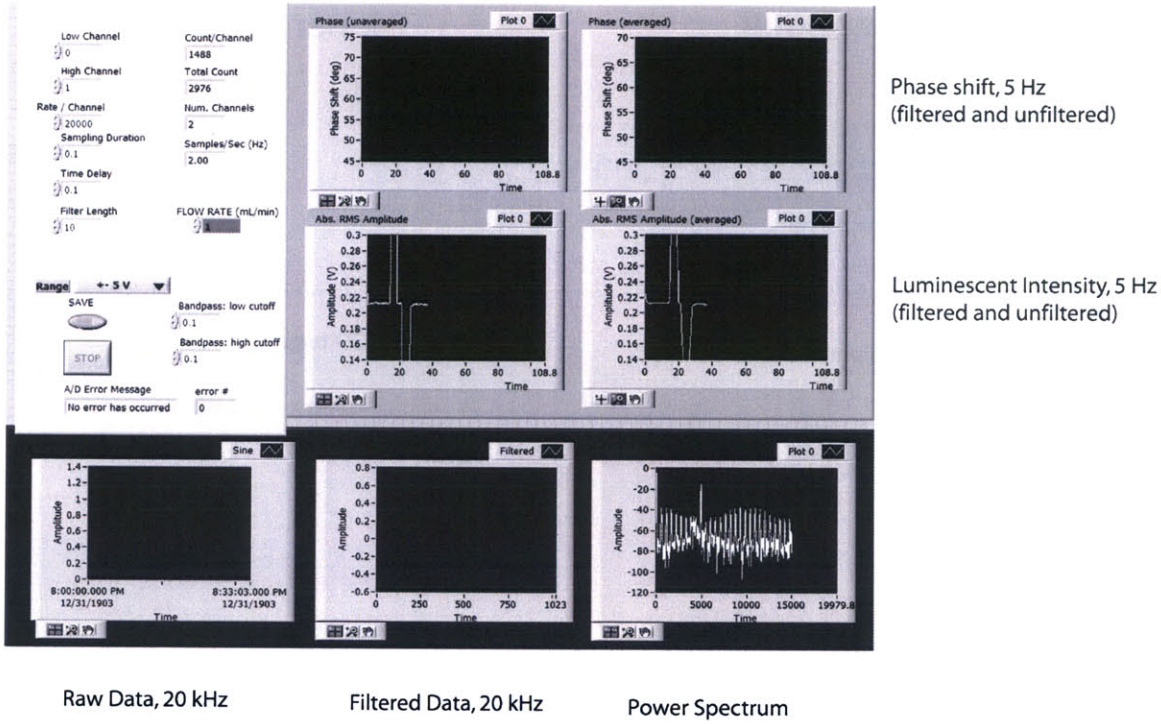

Figure C.2: Labview VI front end for optical oxygen sensor

Unlike the phase shift and luminescent intensity plots which display the averaged data continuously in real-time, the 20 kHz raw data and power spectrum plots are refreshed with every 0.2 sec. sampling cycle. A flowchart for the VI operation is shown in fig. C.3. An outer shell of 3 increments runs a single time during the recording of one dataset. In the first increment (1), the analog and digital ports of the DAQ board are initialized. In the second increment (2), the data acquisition and processing occurs within a nested "inner loop". Within this inner loop, in step (2a), the modulated LED is turned on. In the second loop increment (2b), the DAQ board is sampled for the duration t_S at the specified sampling frequency. In the third loop increment (2c), data acquired in step (2b) is processed to determine average phase and intensity values. In the final loop step (2d) the

LED is turned off and the average phase and intensity values are added to a buffer of data points. User input to cease data acquisition ejects the program from the inner loop. The final step of the VI's outer shell (3) is to save the buffered data points from (2d) to a file, from which they can be post-processed in matlab.

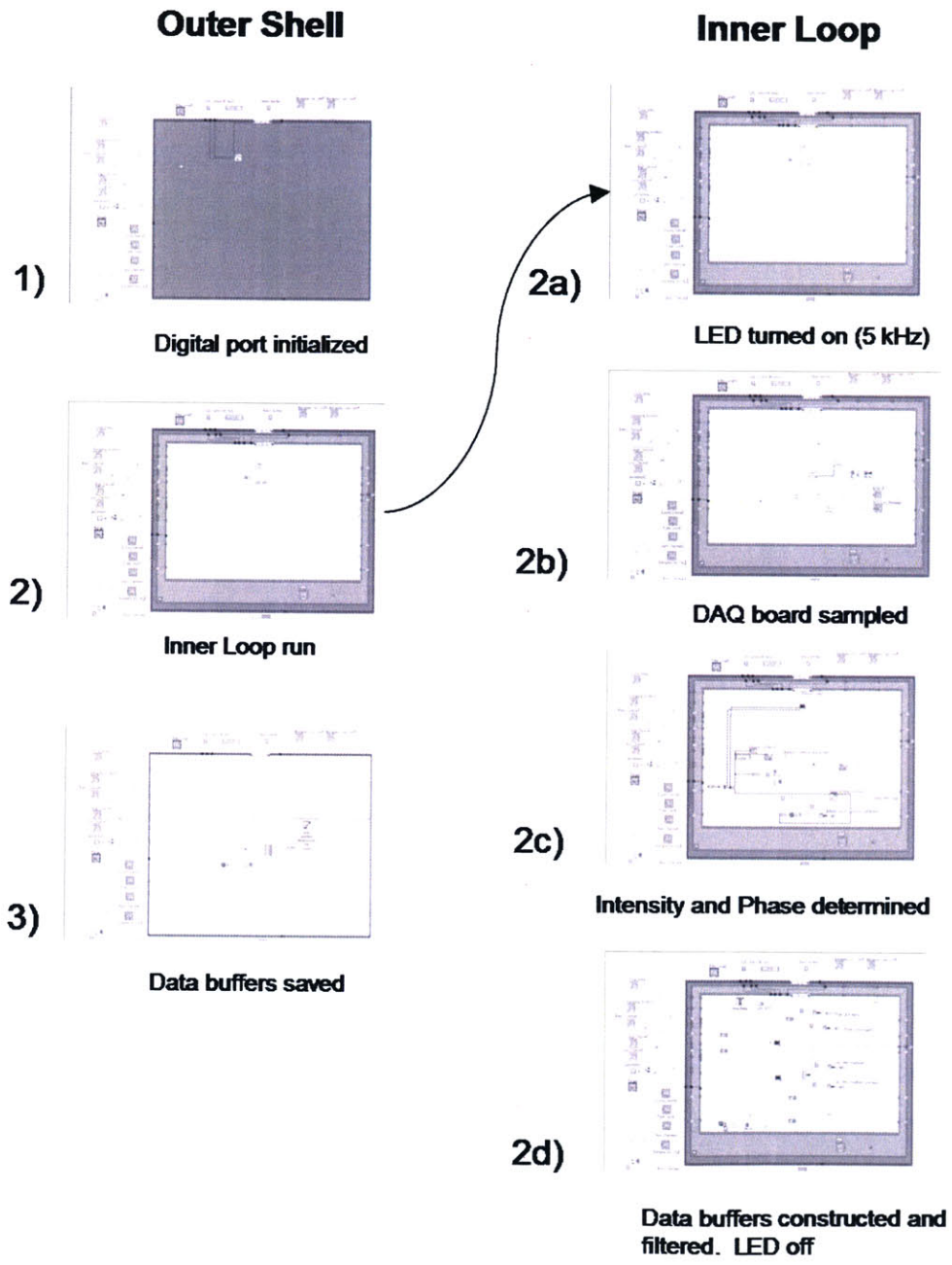

Figure C.3: Operational flowchart for optical sensor Labview VI

References

1. K.H. Orbon, T.R. Schermer, J.W. Van der Gulden, et al., Employment status and quality of life in patients with chronic obstructive pulmonary disease, *International Archives of Occupational and Environmental Health*, 1900,

2. G. Gudmundsson, T. Gislason, C. Janson, et al., Depression, anxiety and health status after hospitalisation for COPD: A multicentre study in the Nordic countries, *Respiratory Medicine*, In Press, Corrected Proof,

3. W. Harringer, K. Wiebe, M. Struber, et al., Lung Transplantation - 10 year experience, *J Cardiothorac Surg*, 1999, 16, 546-554.

4. J.D. Hosenpud, L.I. Bennet, B.M. Keck, et al., The registry of the International Society for Heart and Lung Transplantation: 15th official report, *J Heart Lung Assoc*, 1998, 17, 656-668.

5. J. DeMeester, J.M. Smits, G.G. Persijn, et al., Listing for lung transplantation: life expectancy and transplant effect, stratified by type and stage of lung disease, the Eurotransplant experience, *J Heart Lung Transplant*, 2001, 20, 518-524.

6. L.D. Sharples, G.J. Taylor, J. Karnon, et al., A model for analyzing the cost of the main clinical events after lung transplantation, *J Heart Lung Transplant*, 2001, 20,

7. R.P. Byrd and T.M. Roy, *Mechanical Ventilation*, http://www.emedicine.com/med/topic3370.htm, 2004.

8. J. Orme, J.S. Romney, R.O. Hopkins, et al., Pulmonary function and health-related quality of life in survivors of acute respiratory distress syndrome, *American Journal of Respiratory and Critical Care Medicine*, 2003, 167, 690-694.

9. N.G. Smedira, N. Moazami, C.M. Golding, et al., Clinical experience with 202 adults reeiving extracorporeal membrane oxygenation of heart failure. Survival at five years, *J. Thorac. Cardiovasc. Surg.*, 2001, 122,

10. K. Eya, F. Tatsumi, Y. Taenaka, et al., Development of a membrane oxygenator for long-term respiratory support and its experimental evaluation in prolonged ECMO, *J. ASAIO*, 1996, 42,

11. G. Zobel, M. Kuttnig-Haim, B. Urlesberger, et al., Extracorporeal lung support in pediatric patients, *Acta. Anesth. Scand. Suppl.*, 1996, 109, 122-125.

12. G.B. Fiore, G. Pennati, F. Inzoli, et al., Effects of blood flow pulse frequency on mass transfer efficiency of a commercial hollow fibre oxygenator, *International Journal of Artificial Organs*, 1998, 21, 535-541.

13. A. D'Armini, E.J. Tom, C.S. Roberts, et al., When does the lung die? Time course of high energy phosphate depletion and relationship to lung viability after death., *J. Surg. Res.*, 1995, 59,

14. M. Brischwein, E.R. Motrescu, E. Cabala, et al., Functional cellular assays with multiparametric silicon sensor chips, *Lab Chip*, 2003, 3, 234-240.

15. T.C. O'Riordan, D. Buckley, V. Ogurtsov, et al., A Cell Viability Assay Based on Monitoring Respiration by Optical Oxygen Sensing, *Anal. Biochem.*, 2000, 278, 221-227.

16. H. Andersson and A.V.d. Berg, Microfabrication and Microfluidics for Tissue Engineering: State of the Art and Future Opportunities, *Lab Chip*, 2004, 98-103.

17. Y.N. Xia and G.M. Whitesides, Soft lithography, *Annu. Rev. Mat. Sci.*, 1998, 28, 153-184.

18. G.M. Whitesides, E. Ostuni, S. Takayama, et al., SOFT LITHOGRAPHY IN BIOLOGY AND BIOCHEMISTRY, *Annu. Rev. Biomed. Eng.*, 2001, 3, 335-373.

19. T. Thorsen, S.J. Maerkl and S.R. Quake, Microfluidic Large-Scale Integration, *Science*, 2002, 298, 580-584.

20. J.B. Brzoska, I. Benazouz and F. Rondelez, Silanization of Solid Substrates - a Step toward Reproducibility, *Langmuir*, 1994, 10, 4367-4373.

21. L.E. Rodd, T.P. Scott, D.V. Boger, et al., *XIVth Int. Congr. on Rheology,* 2004

22. Y.C. Fung, *Biomechanics: circulation*, 2nd edn., Springer, New York, 1997.

23. C.K. Mathews and K.E.v. Holde, *Biochemistry*, edn., Benjamin Cummings, Redwood City, 1990.

24. C.H. Brown, L.B. Leverett, C.W. Lewis, et al., Morphological, Biochemical, and Functional Changes in Human Platelets Subjected to Shear-Stress, *Journal of Laboratory and Clinical Medicine*, 1975, 86, 462-471.

25. C.H. Brown, R.F. Lemuth, J.D. Hellums, et al., Response of Human Platelets to Shear-Stress, *Transactions American Society for Artificial Internal Organs*, 1975, 21, 35-39.

26. Y.C. Fung, *Biomechanics: Mechanics Properties of Living Tissues*, 2nd edn., Springer, New York, 1993.

27. D. Trebotich, W. Chang and D. Liepmann, *Technical Proceedings of the 2001 International Conference on Modeling and Simulation of Microsystems,* 2001

28. J.P. Shelby, J. White, K. Ganesan, et al., A microfluidic model for single-cell capillary obstruction by Plasmodium falciparum infected erythrocytes, *Proceedings of the National Academy of Sciences of the United States of America*, 2003, 100, 14618-14622.

29. V.V. Gafiychuk and I.A. Lubashevsky, On the principles of the vascular network branching, *Journal of Theoretical Biology*, 2001, 212, 1-9.

30. T.F. Sherman, On Connecting Large Vessels to Small - the Meaning of Murray Law, *Journal of General Physiology*, 1981, 78, 431-453.

31. G.S. Kassab and Y.C.B. Fung, The Pattern of Coronary Arteriolar Bifurcations and the Uniform Shear Hypothesis, *Annals of Biomedical Engineering*, 1995, 23, 13-20.

32. W. Huang, R.T. Yen, M. McLaurine, et al., Morphometry of the human pulmonary vasculature, *Journal of Applied Physiology*, 1996, 81, 2123-2133.

33. K.L. Karau, G.S. Krenz and C.A. Dawson, Branching exponent heterogeneity and wall shear stress distribution in vascular trees, *American Journal of Physiology-Heart and Circulatory Physiology*, 2001, 280, H1256-H1263.

34. Anonymous, GE Handbook Fluidic Resistance, General Electric Technical Document.

35. J.B. Zhang and Z.B. Kuang, Study on blood constitutive parameters in different blood constitutive equations, *Journal of Biomechanics*, 2000, 33, 355-360.

36. F.J. Walburn and D.J. Schneck, Constitutive Equation for Whole Human-Blood, *Biorheology*, 1976, 13, 201-210.

37. W.M. Deen, *Analysis of Transport Phenomena*, edn., Oxford University Press, New York, 1998.

38. D. Falck, Amperometric Oxygen Electrodes, *Current Separations*, 1997, 16,

39. H. Chuang and M.A. Arnold, Radioluminescent sources for optical chemical sensors, *Pure Appl. Chem.*, 1999, 71, 803-810.

40. D.B. Papkovsky, New oxygen sensors and their application to biosensing, *Sens. Actuators, B*, 1995, 29, 213-218.

41. Y.F. Cao, Y.E.L. Koo and R. Kopelman, Poly(decyl methacrylate)-based fluorescent PEBBLE swarm nanosensors for measuring dissolved oxygen in biosamples, *Analyst*, 2004, 129, 745-750.

42. D.B. Papkovsky, G.V. Ponomarev and W.T.a.P. Oleary, Phosphorescent Complexes of Porphyrin Ketones: Optical Properties and Application to Oxygen Sensing, *Anal. Chem.*, 1995, 67, 4112-4117.

43. D.B. Papkovsky, A.N. Ovchinnikov, V.I. Ogurtsov, et al., Biosensors on the basis of luminescent oxygen sensor: the use of microporous light-scattering support materials, *Sens. Actuators, B*, 1998, 51, 137-145.

44. C.S. Burke, O. McGaughey, J.M. Sabattie, et al., Development of an integrated optic oxygen sensor using a novel, generic platform, *Analyst*, 2005, 130, 41-45.

45. D.A. Chang-Yen and B.K. Gale, An Integrated Optical Oxygen Sensor Fabricated Using Rapid-Prototyping Techniques, *Lab Chip*, 2003, 3, 297-301.

46. E.R.C.a.J.N. Demas, B.A. DeGraff and J.R. Bacon, Photophysics and Photochemistry of Oxygen Sensors Based on Luminescent Transition-Metal Complexes, *Anal. Chem.*, 1991, 63, 337-342.

47. D.P. O'Neal, M.A. Meledeo, J.R. Davis, et al., Oxygen sensor based on the fluorescence quenching of a ruthenium complex immobilized in a biocompatible Poly(Ethylene glycol) hydrogel, *Sensors Journal, IEEE*, 2004, 4, 728-734.

48. W. Trettnak, C. Kolle, F. Reininger, et al., Miniaturized luminescence lifetime-based oxygen sensor instrumentation utilizing a phase modulation technique, *Sens. Actuators, B*, 1996, 36, 506-512.

49. I. Bergman, Rapid-response atmospheric oxygen monitor based on fluorescence quenching, *Nature*, 1968, 218, 396.

50. I. Klimant and O.S. Wolfbeis, Oxygen-Sensitive Luminescent Materials Based on Silicone-Soluble Ruthenium Diimine Complexes, *Anal. Chem.*, 1995, 67, 3160-3166.

51. W. Trettnak, C. Kolle, F. Reininger, et al., Optical oxygen sensor instrumentation based on the detection of luminescence lifetime, *Adv. Space Res.*, 1998, 22, 1465-1474.

52. A. Zanzotto, N. Szita, P. Boccazzi, et al., Membrane-aerated microbioreactor for high-throughput bioprocessing, *Biotechnol. Bioeng.*, 2004, 87, 243-254.

53. J.T. Borenstein, H. Terai, K.R. King, et al., Microfabrication Technology for Vascularized Tissue Engineering, *Biomed. Microdev.*, 2002, 4, 167-175.

54. W.M. Rohsenow and H. Choi, *Heat, Mass, and Momentum Transfer*, edn., Prentice-Hall, Englewood Cliffs, NJ, 1961.

55. W.M. Kays and M.E. Crawford, *Convective Heat and Mass Transfer*, 3rd edn., McGraw-Hill, New York, 1993.

56. R. Probstein, *Physicochemical Hydrodynamics*, 2nd edn., Wiley-Interscience, Hoboken, NJ, paperback, 2003.

57. R. Shah and A. London, *Laminar Flow Forced Convection in Ducts: a Source Book for Compact Heat Exchanger Analytical Data*, edn., Academic Press, New York, 1978.

58. M.C. Belanger and Y. Marois, Hemocompatibility, biocompatibility, inflammatory and in vivo studies of primary reference materials low-density polyethylene and polydimethylsiloxane: A review, *Journal of Biomedical Materials Research*, 2001, 58, 467-477.

59. A. Lloyd, Improving the biocompatibility of silicone, *Materials Today*, 2003, November, 19.

60. J. Brandrup and E.H. Immergut, *Polymer Handbook*, 2 edn., 1974.

61. Anonymous, Photodiode Monitoring with Op Amps, Burr-Brown Application Bulletin AB-075. Burr-Brown, Tucson, AZ, 1994.

62. R. Nave, *Square Wave Generator*, http://hyperphysics.phy-astr.gsu.edu/hbase/electronic/square.html, 2001.

63. R.E. Simpson, *Introductory Electronics for Scientists and Engineers*, 2nd edn., Allyn and Bacon, 1987.

64. K. Bigelow, *A Precision Half-Wave Rectifier*, http://www.play-hookey.com/analog/half-wave_rectifier.html, 1996.

65. B. Pease, *What's all this transimpedance amplifier stuff, anyhow?*, http://www.elecdesign.com/Articles/Print.cfm?ArticleID=4346, 2001.

66. J. Graeme, *Photodiode Amplifiers - Op Amp Solutions*, edn., McGraw-Hill, New York, 1995.

67. M. Stitt and W. Meinel, OPT201 Photodiode-amplifier rejects ambient light, Burr-Brown Application Bulletin AB-061. Burr-Brown Corporation, Tucson, AZ, 1993.

68. Wolfram, *Mathworld - Nyquist Frequency*, http://mathworld.wolfram.com/NyquistFrequency.html, 1999.

69. P. Kromer, *PC-Based Digital Lock-In Detection of Small Signals in the Presence of Noise*, http://mrflip.com/papers/LIA/AAPTPaper/AAPTPaper.pdf, 1999.

70. S. Cova, A. Longoni and I. Freitas, Versatile Digital Lock-in Detection Technique - Application to Spectrofluorometry and Other Fields, *Review of Scientific Instruments*, 1979, 50, 296-301.

71. Wolfram, *Mathworld - Hilbert Transform*, http://mathworld.wolfram.com/HilbertTransform.html, 1999.